Raman Spectroscopy Analysis of CVD Hard Coatings Deposited in the $TiC_{1-x}N_x$, $TiB_xC_yN_z$ and Ti-B-N System

Dissertation
der Mathematisch-Naturwissenschaftlichen Fakultät
der Eberhard Karls Universität Tübingen
zur Erlangung des Grades eines
Doktors der Naturwissenschaften
(Dr. rer. nat.)

vorgelegt von
Ines Dreiling
aus Böblingen

Tübingen
2011

Tag der mündlichen Qualifikation: 18.07.2011

Dekan: Prof. Dr. Wolfgang Rosenstiel

1. Berichterstatter: Prof. Dr. Thomas Chassé

2. Berichterstatter: Prof. Dr. Dines Christen

This doctoral thesis was carried out at the Institut für Physikalische und Theoretische Chemie, at the Mathematisch-Naturwissenschaftliche Fakultät of the Eberhard-Karls-Universität Tübingen, Germany, under the guidance of Prof. Dr. Thomas Chassé in cooperation with the Walter AG Tübingen.

Foremost, I am indebted to Prof. Dr. Thomas Chassé and Dr. Dirk Stiens, my supervisors from the University of Tübingen and the Walter AG, respectively, for their support and excellent guidance during this work. I would like to thank them for providing me the lab facilities and a perfect working environment, as well as for their confidence. I could not have learnt more about physical chemistry, materials science, scientific research and communication during the course of this work.

I thank all current and former members of the AG Chassé for valuable discussions and for a friendly working atmosphere. I would like to specially thank Dr. I. Biswas, C. Raisch, M. Glaser and S. Savu.

Furthermore, I would like to thank Prof. Dr. H.-J. Meyer and Dr. J. Glaser for welcoming me in their laboratory and helping me with the chemical synthesis. Especially, I would like to thank Dr. J. Glaser for his comments and discussions which proved to be very valuable for several parts of this thesis. Moreover, I would like to thank PD Dr. T. Wenzel for the WDX measurements and for the many useful discussions.

I thank the Walter AG Tübingen for the generous financial support of my thesis and the successful cooperation, especially Dr. H. Holzschuh. I would further like to thank M. Schaible for her assistance in several experiments.

Finally, I am thankful to my family and to Adrian for their support and for the inspiration they gave me.

Parts of this work have already been published or accepted for publication:

I. Dreiling, A. Haug, H. Holzschuh, T. Chassé, 'Raman spectroscopy as a tool to study cubic Ti–C–N CVD coatings', *Surf. Coat. Technol. 204 (2009) 1008-1012*.

I. Dreiling, D. Stiens, T. Chassé, 'Raman spectroscopy investigations of $TiB_xC_yN_z$ coatings deposited by low pressure chemical vapor deposition', *Surf. Coat. Technol. 20 (2010) 1339-1344.*

I. Dreiling, C. Raisch, J. Glaser, D. Stiens, T. Chassé, 'Characterization and oxidation behavior of MTCVD Ti-B-N coatings', *Surf. Coat. Technol.*, accepted for publication (07.2011)

Conference contributions:

04/2009: ICMCTF 2009, San Diego, CA/USA. Oral Presentation: 'Properties and Tribological Behavior of CVD TiBN-Coated Cutting Tools' in cooperation with the WALTER AG, Tuebingen.

04/2009: ICMCTF 2009, San Diego, CA/USA. Poster Presentation: 'Raman Spectroscopy as a Tool to Study Cubic Ti-C-N CVD Coatings' in cooperation with the WALTER AG, Tuebingen.

04/2010: ICMCTF 2010, San Diego, CA/USA. Oral Presentation: 'Raman Spectroscopy Investigations of CVD Hard Coatings in the Ti-B-C-N system' in cooperation with the WALTER AG, Tuebingen.

Table of contents

1. Introduction

Cemented carbide tools used today for metal cutting are markedly improved by the application of a thin, hard and uniform layer on their surface, the so-called coating. Around 1970 the manufacture of such coatings by chemical vapor deposition (CVD) was introduced. These CVD coatings permit to increase the wear resistance and lifetime of cemented carbide tools by a factor of 10. (1)

Today typical industrial coatings deposited by CVD are for example of $TiC_{1-x}N_x$, $TiB_xC_yN_z$ and Ti-B-N.

$TiC_{1-x}N_x$ coatings deposited by CVD have advantageous properties like excellent adherence, high hardness and high toughness. The complete miscibility within the TiN-TiC system enables the variation of the properties from high toughness and good chemical stability of TiN to high hardness and abrasion resistance of TiC. (2; 3; 4)

In addition to ternary $TiC_{1-x}N_x$, quaternary $TiB_xC_yN_z$ coatings have more recently received a lot of attention since it has been shown that the addition of boron to $TiC_{1-x}N_x$ improves the wear resistance by increasing the film hardness (5; 6; 7). Furthermore, $TiB_xC_yN_z$ coatings were found to display excellent tribological properties (8; 9). Deposition and characterization of $TiB_xC_yN_z$ coatings are part of an overall program to develop non-sticking, oxidation and wear-resistant coatings for forming tools. (9)

Deposition parameters like temperature and gas composition have a great influence on the microstructure, composition and mechanical properties of CVD $TiC_{1-x}N_x$ and $TiB_xC_yN_z$ coatings. In high-temperature CVD (HTCVD) the C:N ratio in the coating can easily be changed by varying the precursor flow rates of N_2 and CH_4 during the CVD process. This results in a variety of coatings with different compositions and properties. However, the elevated temperatures in HTCVD support boron diffusion and decarburization of the cemented carbide inserts. (5; 6; 10)

As a result, a brittle η-phase and CoWB is formed at the substrate-coating interface, which can cause chipping when subjected to the cyclic mechanical and thermal stresses characteristic for milling (10; 11). The lower temperatures (700-900°C) in combination with more reactive precursors (CH_3CN) used in moderate-temperature CVD (MTCVD) reduce diffusion and decarburization, and thus avoid the formation of brittle phases in the surface region (12). Therefore, MTCVD coated inserts are known to have increased toughness (10; 13; 14). However, in contrast to HTCVD, it is not possible to vary the composition of MTCVD coatings in such a wide range. The C:N ratio is here almost independent from the precursor flow rates (5; 6; 13).

Ti-B-N coatings also possess excellent properties for cutting applications. They combine extreme hardness with high toughness; furthermore they exhibit good corrosion and wear resistance, and show high thermal stability (15; 16; 17; 18). The different phases within the ternary Ti-B-N system provide the possibility of depositing wear-resistant coatings that offer a wide range of properties. (19; 20; 21) Thus, a significant amount of work has already been published on this coating system deposited by physical vapor deposition (PVD) (17; 19; 22; 23) and plasma-assisted chemical vapor deposition (PACVD) (17; 18; 24; 25; 26). Investigations of CVD Ti-B-N coatings revealed only the formation of TiN and TiB_2 where the coating composition could be varied from pure TiN to pure TiB_2 (15; 16).

Not only the composition but also the oxidation resistance has a great influence on the wear performance of hard coatings because of the increased temperatures occurring in the contact zone during machining operation. The degradation (chemical reaction, cratering) of titanium-based coatings is known to be due to the formation of titanium oxides at the surfaces which can cause delamination (27; 28). For titanium carbonitride coatings the extent of oxidation was found to be highly dependent on the carbon and nitrogen concentration (2; 29; 30).

The oxidation behavior of Ti-B-C-N coatings has already been studied to some extent. It has been suggested that they are inherently prone to oxidize, since most of the oxidation products are gaseous and evaporate, therefore rather destroying than protecting the coating. (7; 31)

In Ti-B-N coatings, on the other hand, low boron concentrations are known to considerably increase the thermal stability compared to TiN (23; 32; 33; 34). But despite being important, the oxidation behavior of CVD Ti-B-N coatings with different boron concentrations has not yet been investigated in detail.

In the field of materials science, tribological model tests are typically performed in the laboratory scale to evaluate the performance of hard coatings in real working conditions. The tribological behavior of Ti-B-N coatings has been investigated before and outstandingly low friction values were found (20; 18). As an explanation a self-lubrication mechanism resulting from tribochemical reactions in the contact zone was proposed by the formation of Magnéli-phases or boric acid H_3BO_3 (20).

In the last decades, Raman spectroscopy has become a very powerful tool to study molecules and materials due to the development of new technologies like high stability laser excitation, sensitive charge coupled device detectors (CCDs), and the coupling with optical microscopes. These advantages combined with the fact that this analysis method is non-invasive and non-destructive resulted in the situation that many more research groups today elaborate the potential of Raman spectroscopy. (35)

In the late 1980s Raman spectroscopy has further been introduced as a promising technique for the analysis of wear debris and wear tracks formed during tribological testing, since it provides a possibility to observe and quantify surface chemistry changes with a high spatial resolution (36). Nowadays, also real-time identification of transfer film composition is possible by the usage of in-situ Raman tribometers (37; 38).

Raman spectroscopy takes advantage of the inelastic scattering of monochromatic laser light by molecules or crystal lattices. The resulting information can be used to determine details on the structure and composition as well as on the crystallinity and orientation of the sample. Furthermore different prevailing stress conditions can be identified.

In the field of surface engineering the majority of Raman spectroscopy investigations are performed on films like diamond-like carbon (DLC), tetrahedral amorphous carbon (ta-C) and chemical vapor deposited (CVD) diamond films because of its high sensitivity for different carbon phases (39; 40; 41).

Furthermore, Raman spectroscopy has already successfully been used to study first generation transition-metal hard coatings, like TiN and TiC. In such cubic crystal systems, first-order Raman scattering is actually forbidden, but the relatively high percentage of lattice defects in such coatings allows the detection of defect-induced Raman spectra. The intensity, frequency and width of the Raman features are thereby strongly dependent on the chemical composition, defects, short-range order, crystalline structure, and internal stresses in the material. (35; 42; 43; 44; 45; 46; 47)

However, up to now only little work has been done on advanced multicomponent hard coatings like TiCN, TiAlN, TiZrN or Ti_3SiC_2 (35; 48).

The objective of this work is to demonstrate the analytical power of Raman micro-spectroscopy on different ternary and quaternary titanium-based CVD coatings, like $TiC_{1-x}N_x$, $TiB_xC_yN_z$ and Ti-B-N. The analyses were performed with regard to changes in the basic coating properties, like the composition and microstructure. Since Raman spectroscopy is up to now no commonly used analysis method for such coatings, the results are correlated to those obtained by well established other techniques like X-ray diffraction (XRD), wavelength-dispersive X-ray spectroscopy (WDS), scanning electron microscopy (SEM) and X-ray photoelectron spectroscopy (XPS).

In order to gain better understanding of the high temperature oxidation, Raman spectroscopy was further used to study the oxidation processes of TiC, TiN, $TiC_{1-x}N_x$, $TiB_xC_yN_z$ and Ti-B-N coatings by the spectroscopic detection of the formed oxidation products after annealing under ambient conditions at different temperatures.

To study tribochemical reactions of Ti-B-N coatings, Raman analysis was performed on the wears tracks of tribological tested samples to examine the types of the formed oxides in the contact zone. The identified compounds were correlated with the observed friction coefficients. Additionally, turning tests with Ti-B-N coated inserts were performed at various turning speeds. The compounds identified by Raman spectroscopy on the rake face were compared to those found on the wear tracks after tribological testing to estimate an approximate value for the contact temperature in machining operations.

2. Theoretical background

2.1 Chemical vapor deposition (CVD)

Today approximately 90% of cutting tools are coated in order to increase the lifetime of hard metals for cutting and milling operations. The demands on coated inserts surfaces are that they have to resist interactions with the work piece (e.g. steel) and the environment (e.g. oxidation). Furthermore, an excellent adherence to the sintered compact is needed, and the coating in itself must possess high hardness, fracture toughness and strength. Coatings of transition-metal compounds (e.g. the corresponding nitrides, carbides and borides) are mainly produced by chemical vapor deposition (CVD) and physical vapor deposition (PVD). (49)

In thermal CVD, a defined mixture of the carrier gas (H_2) and the reaction gases (= precursors, usually a volatile metal compound such as a chloride with a nitrogen and/or a carbon or boron based gas like CH_4, CH_3CN or BCl_3) is passed over a substrate (typically cemented carbide inserts) at temperatures of 850-1000°C. A typical CVD system (Fig. 1) therefore consists of (50):

1) gas sources and feed lines
2) mass flow controllers
3) the reaction chamber
4) heating system for the substrate on which the film is deposited
5) temperature sensors

The reaction products form a solid, strongly adherent layer on the substrate with a thickness of approximately 5-20 µm.

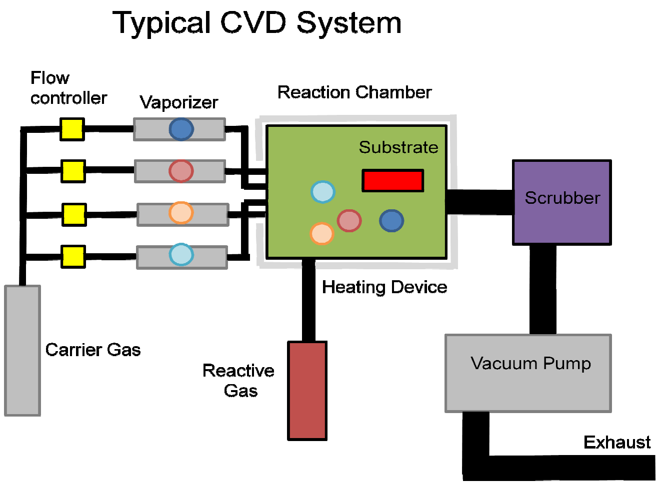

Fig. 1: Typical set-up of a thermal CVD system **(51)**.

In addition to thermal CVD, plasma- or laser-assisted CVD has been developed where the temperatures can be lowered to about 400°C (49). This reduces for example undesired side reactions, like the decarburization of the cemented carbide inserts as well as the formation of thermal cracks due to the different thermal expansion coefficients of the substrate and the coating.

The most important CVD processes are (52):

- Atmospheric pressure CVD (APCVD) – conditions: T = 400-1300°C, p = 1 bar. Advantage: High deposition rates are achieved due to use of atmospheric pressure.

- Low-pressure CVD (LPCVD) - conditions: T = 500-1000°C, p = 0.01-10 mbar. Advantage: The reduced pressure retards unwanted gas-phase reactions and improves the film uniformity.

- Plasma-Enhanced/Assisted CVD (PECVD/PACVD) - conditions: T = 200-500°C, p = 1 mbar. Advantage: Deposition at lower temperatures is possible since plasma is used to enhance chemical reaction rates of the precursors.

The coatings investigated in this work were all deposited by LPCVD. LPCVD itself can further be separated into high-temperature (HTCVD) and moderate-temperature (MTCVD) processes. In HTCVD, the deposition temperature is about 1000°C and the precursors are usually a metal chloride, nitrogen and methane. In MTCVD, the usage of a more reactive precursor (CH_3CN) instead of N_2 and CH_4 enables the deposition at lower temperatures (700-900°C). A detailed description of the used parameters is given in Chapter 3.1.

The fundamental steps in a CVD process (Fig. 2) can be summarized as follows (50):

1) A defined mixture of reactant gases and diluent inert gases are introduced into the reaction chamber at a specified flow rate
2) Diffusion of the gas species to the substrate surface
3) Adsorption of the reactants on the substrate surface (physisorption)
4) Chemical reaction (chemisorptions) of the reactants with the substrate to form the film
5) Desorption of the gaseous by-products of the reactions and evacuation from the reaction chamber

During the CVD process, the reactant gases can undergo heterogeneous and homogeneous reactions. Heterogeneous reactions occur on the heated surfaces, not only of the tool but in the entire system of the reaction chamber. In this case, good-quality films are observed (high-purity, high-performance solid materials). Homogeneous reactions, on the other hand, occur in the reactor's atmosphere in the gas phase and aggregates of the depositing material are formed. These aggregates adhere poorly to the surface and low-density films with a high defect rate are obtained. Therefore, heterogeneous reactions are much more desirable than homogeneous reactions during CVD. (50)

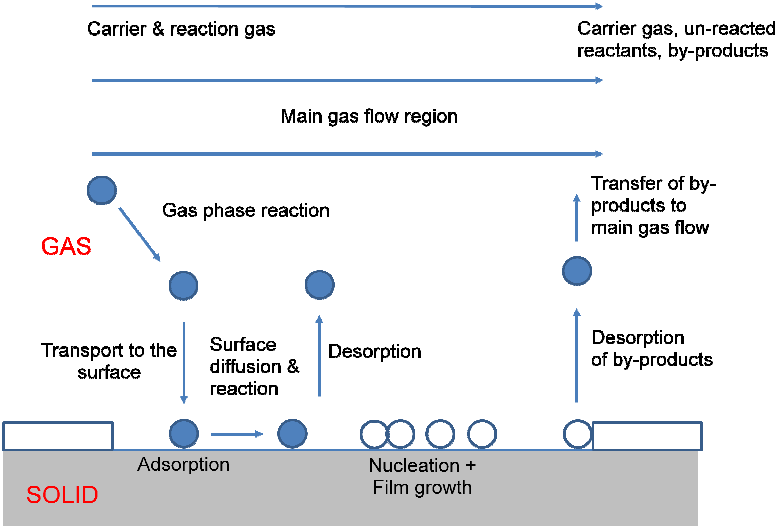

Fig. 2: Fundamental steps in a CVD process (53).

Similar to CVD, PVD processes can be separated into different variants, which include for example (52):

- Cathodic Arc Deposition (Arc-PVD)
- Electron beam physical vapor deposition (EBPVD)
- Pulsed laser deposition (PLD)
- Sputter deposition

However, since the here studied coatings were all deposited by CVD, details on the different PVD techniques are beyond the scope of this text. For further information the reader may refer to (54).

2.2 Titanium-based hard coatings

Hard coatings, which are actually in use and widely studied, are binary, ternary and quaternary compounds containing titanium. Particularly, the titanium nitrides, carbides, borides, carbonitrides and boronitrides exhibit a combination of outstanding properties, like exceptional hardness, high melting points, metallic luster and simple metallic structures, resulting in a variety of technical applications (49).

Generally, these coatings form interstitial alloys or compounds, where the small carbon, nitrogen or boron atoms are located in the interstitial voids of the densely-packed host lattice. They either exhibit face-centered cubic (f.c.c.) or hexagonal close packed (h.c.p.) metal lattices with randomly distributed non-metal atoms on the interstitial sites. The metal atoms form thereby close packed arrangements of metal layers with ABCABC… (cubic) or ABAB… (hexagonal) stacking sequence, and the non-metal atoms occupy the octahedral interstitial sites (55). The crystallo-chemical rule (56; 57) states, that a pure cubic type phase can posses a maximum non-metal/metal ratio of 1, whereas for the hexagonal type phase the maximum ratio is ½. (55)

Ternary systems often consist of mixtures of different binary compounds (58). This applies for example for the Ti-B-N system, where TiB_2 and TiN coexist as a crystal mixture, due to the insolubility of boron in TiN as well as of nitrogen in TiB_2 (19; 21; 59). Contrarily, binary TiC and TiN are known to form a solid solution over a wide homogeneity range (60; 61) resulting in ternary Ti-C-N compounds where the properties are highly dependent on the nitrogen and carbon concentration (5; 6; 49).

A table summarizing the most important properties of the binary systems TiC, TiN and TiB_2 can be found in the appendix (Table 15, p.134). Values are taken from (62) and references therein.

As is apparent from the two examples described above, for the deposition and analysis of different ternary coatings, it is essential to understand the phase diagrams, not only of the ternary systems of interest, but also of the binary surrounding systems. Therefore, the phase diagrams of the here studied TiN, TiC, Ti-C-N, TiB_2 and Ti-B-N coatings will be discussed in the following.

2.2.1 The Ti-N and Ti-C systems

TiN and TiC exhibit a NaCl-type structure, in which the cubic close packed titanium atoms form octahedral voids which are filled by carbon or nitrogen atoms. The bonding character is a mixture of metallic, covalent and ionic. The metallic character is thereby displayed by the high electrical conductivity (see appendix Table 15, p. 48). The covalent contribution, given by the molecule orbital (MO) scheme, shows a change in bonding strength from strong Ti-C interaction in TiC to more pronounced Ti-Ti interaction in TiN. The ionic contribution, due to charge transfer from the metal to the nonmetal atom, is about half an electron and contributes to electrostatic interactions. (49)

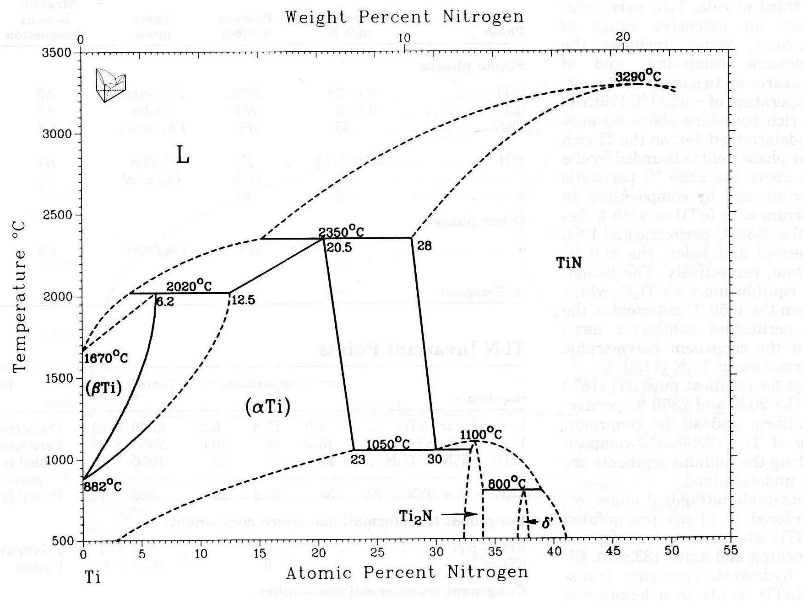

Fig. 3: Equilibrium phase diagram of the Ti-N system (63).

The equilibrium phase diagram of the Ti-N system (63) is shown in Fig. 3. It can be seen, that nitrogen exhibits a high solubility in αTi. The phase diagram exists mainly of αTi, βTi, tetragonal Ti_2N and cubic TiN, which provides a wide homogeneity range between 28 and 55 at.% N. Ti_2N on the other hand has a narrow homogeneity range (~ 33 at %) and is surrounded by αTi and TiN on the nitrogen rich side.

TiC crystallizes in the f.c.c. type structure mono-carbide. The equilibrium phase diagram of Ti-C (64) shown in Fig. 4 depicts the homogeneity range of TiC between 35-48.8 at.% C. Carbon concentrations above 48.8 at.% result in a binary-phase structure of TiC and graphite. Another existent titanium carbide is Ti_2C, where vacancies are ordered on the carbon sublattice. Ti_2C is stable between 32-36 at.% C (58; 64).

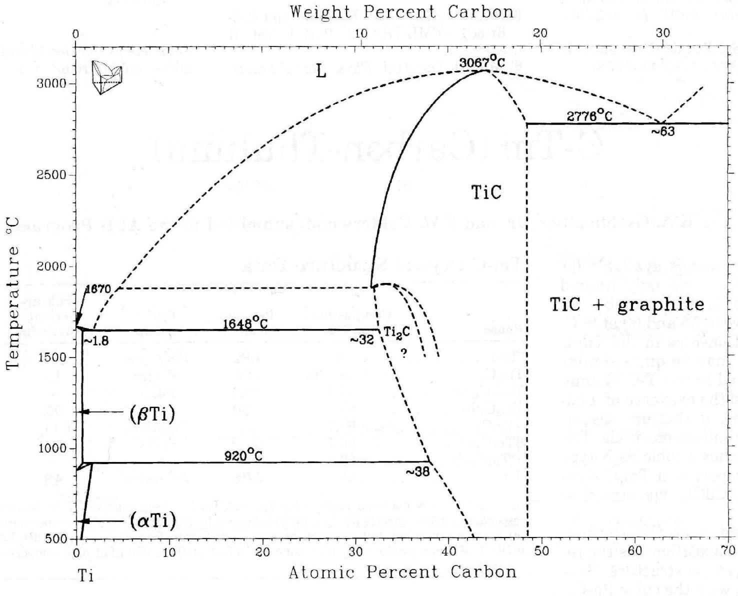

Fig. 4: Equilibrium phase diagram of the Ti-C system (64).

2.2.2 The Ti-C-N system

Due to the high similarities between TiN and TiC (same crystal structures with similar atomic radii of carbon and nitrogen), carbon/nitrogen can be replaced completely by nitrogen/carbon, without changing the structure of the binary phase (49; 58; 60). Within the ternary carbonitrides, Ti-C-N is one of the most important systems. The phase diagram (Fig. 5) shows a complete quasi-binary solid solution of the binary f.c.c. carbides and nitrides. All octahedral interstitial lattice sites are randomly occupied by carbon and nitrogen and consequently also the voids are randomly distributed. A large variation of composition is possible because of the wide range of homogeneity. (58; 61)

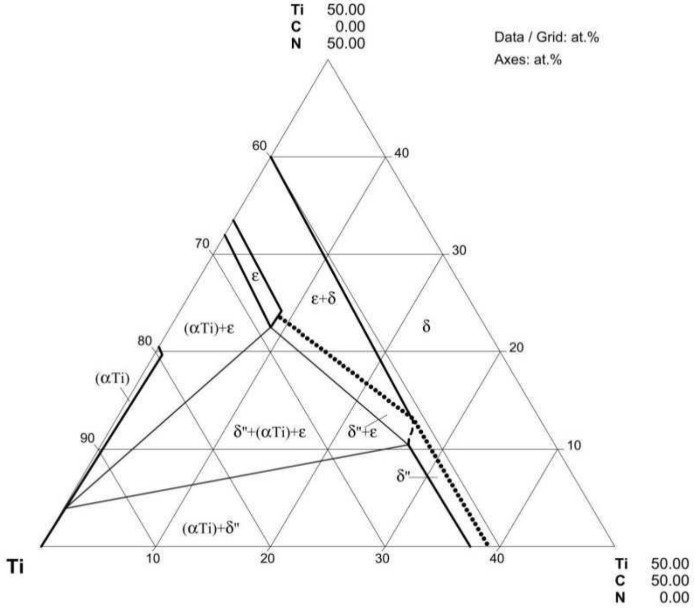

Fig. 5: Phase diagram of Ti-C-N at 500°C with δ” = Ti_2C_{1+x}, (Ti_8C_5); ε = Ti_2N; δ =$Ti(C_xN_{1-x})$. **(61)**

Coatings deposited in the Ti-C-N system are very important for technical applications since they possess high hardness, high corrosion resistance and high thermodynamic stability. The properties can thereby be tailored by the variation of the carbon and nitrogen concentration (61). For example, transition-metal carbides exhibit a gray color, whereas the nitrides show an intense golden appearance. For the carbonitrides, the color can be changed as a function of the C:N ratio (49). The appearance of the coating can thus be used to distinguish between C- and N- rich carbonitrides. Similar dependency applies for the microhardness, which increases constantly with increasing carbon concentration (5; 6). Furthermore, it is known that the curve of lattice parameter of a continuous series of solid solutions between the isostructural binary phases TiC and TiN vs. composition is almost linear (60; 61).

2.2.3 The Ti-B system

Transition-metal borides generally exhibit high hardness, possess exceptional physical properties (like high melting points, high electrical conductivity) and the chemical resistance against oxidation increases with the boron concentration. Many diborides show therefore superhardness (i.e. hardness values > 40 GPa), are chemically inert and high-temperature stable with high melting points (> 3000°C). Furthermore, the electrical conductivity often exceeds that of the corresponding pure elements. (58)

TiB_2 crystallizes in the AlB_2 type structure, which can be described as a sequence of alternating metal and boron layers of hexagonal symmetry. The metal layers are closed-packed, stacked in an A-A-A sequence, resulting in a basal-centered unit cell. The boron-atoms are six-fold coordinated and situated in the center of a trigonal prism formed by the metal atoms. Combined, the titanium and boron atoms form a planar primitive hexagonal, two-dimensional, graphite-like structure with an ABA-BAB … stacking sequence, resulting in a P6/mmm space group. (55)

The Ti-B system is completely different to the Ti-N or Ti-C system. This becomes evident by looking at the equilibrium phase diagram (64) shown in Fig. 6. Here, neither boron is soluble in αTi or βTi, nor titanium in rhombohedral boron. The only two stable phases are TiB (FeB-type structure) and TiB_2 (AlB_2-type structure) whereas the existence of Ti_3B_4 is still discussed (58; 64). The homogeneity ranges of TiB (49-50 at.% B) and TiB_2 (65.5-66.7 at.% B) are very narrow. Independent of the temperature they exist as stoichiometric compounds.

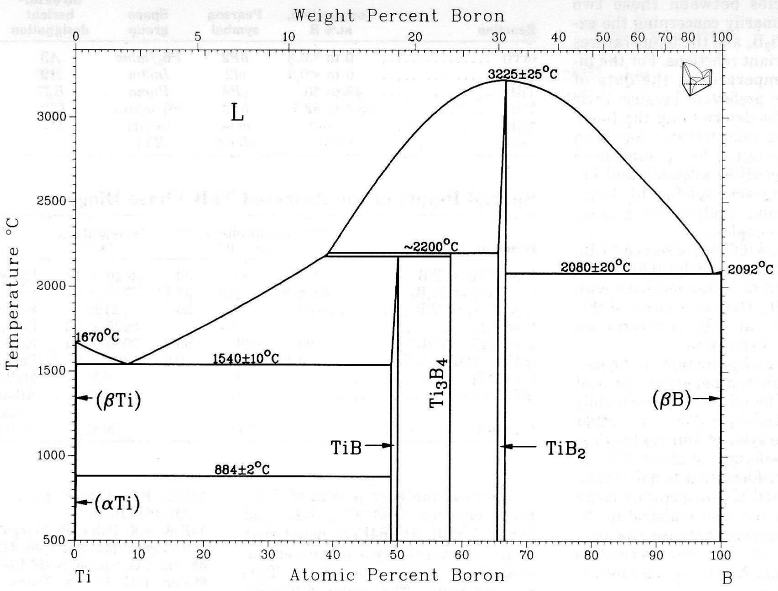

Fig. 6: Equilibrium phase diagram of the Ti-B system **(64)**.

2.2.4 The Ti-B-N system

The Ti-B-N phase diagram (59) is shown in Fig. 7. It clearly demonstrates that no ternary compounds can exist in the Ti-B-N system. Furthermore, the diagram reveals a very limited solubility of boron in TiN and no significant solubility of nitrogen in TiB and TiB_2 (19; 21; 59). Although different multiphase sections are present, it is obviouse that the phase diagram is dominated by the three phase section of TiB_2+TiN+BN.

Owing to the fact that only binary phases exist in the Ti-B-N system, the question arises whether it is reasonable to synthesize Ti-B-N coatings. Actually, it is known that multiphase systems can offer considerable advantages over single-phase systems. They often display higher hardness and toughness values than the hardest single phase system, but therefore coatings with compositions located at particular sections in the phase diagram need to be synthesized. (19)

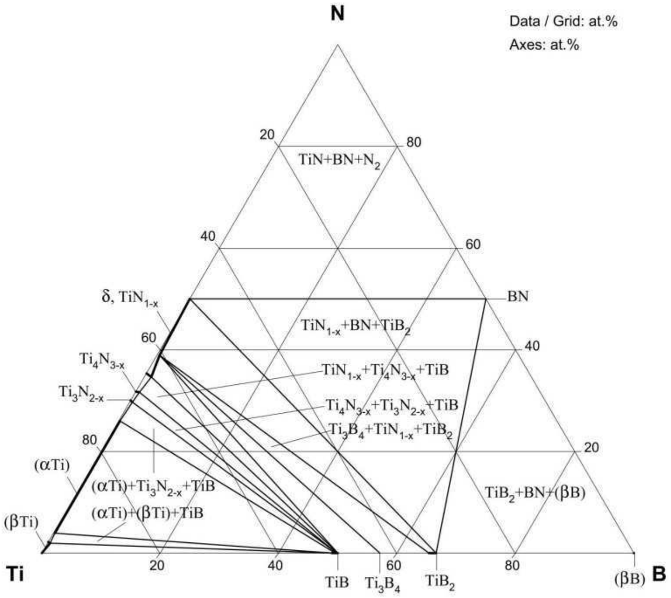

Fig. 7: Phase diagram of Ti-B-N at 1090°C **(59)**.

2.3 Analytical methods

2.3.1 Raman spectroscopy

In this work, Raman spectroscopy was extensively used to study the composition and oxidation behavior of different CVD coatings. Although, it is not (yet) a commonly used analysis method in this field of materials science, the results presented herein may clearly contribute to establish Raman spectroscopy as a complementary technique compared to e.g. XRD and WDS for studying coatings of the Ti-C-N and Ti-B-N systems. Therefore, the theoretical background of this method will be shortly explained in this chapter.

Raman spectroscopy is a vibrational spectroscopy based on the inelastic scattering of a monochromatic exciting source. A sample is irradiated by an intense laser beam in the UV-region (ν_0) and the scattered light consists of:

1. Rayleigh (elastic) scattering, which intensity is proportional to $1/\lambda^4$, with the same frequency as the incident light ν_0.

2. Raman (inelastic) scattering, which is very weak ($I \sim 10^{-5}$ of the incident light) and frequency shifted $\nu_0 \pm \nu_m$ (ν_m is the vibrational frequency of the examined sample). $\nu_0 - \nu_m$ is the so-called Stokes, and $\nu_0 + \nu_m$ the anti-Stokes line. (65)

The vibrational frequency ν_m emitted from the sample is measured as a shift from the incident beam frequency ν_0 given in wavenumbers (cm^{-1}).

Raman scattering can be explained according to the classical theory (65; 66). Based thereon, an electric dipole moment P is induced by irradiation a molecule with light due to the charge separation:

$$P = \alpha E \tag{1}$$

where α is the polarizability, and $E = E_0 \cos 2\pi\nu_0 t$, the electric field strength of the laser beam.

The nuclear displacement q for a vibrating molecule is given by:

$$q = q_0 \cos 2\pi\nu_m t \tag{2}$$

where ν_m is the frequency of the molecular vibration, and q_0 is the vibrational amplitude. For a small amplitude of vibration, α becomes a linear function of q:

$$\alpha = \alpha_0 + (\delta\alpha/\delta q)_0\, q + \ldots \tag{3}$$

where α_0 is the polarizability at the equilibrium position, and $(\delta\alpha/\delta q)_0$ is the rate of change of α with respect to the change in q at the equilibrium position.

By combination of Eq. (1)-(3) P can be written as:

$$P = \alpha_0 E_0 \cos 2\pi\nu_0 t + ½\, (\delta\alpha/\delta q)_0\, q_0\, E_0\, [\cos\{2\pi(\nu_0 + \nu_m)t\} + \cos\{2\pi(\nu_0 - \nu_m)t\}] \tag{4}$$

where the first term represents an oscillating dipole that radiates light of frequency ν_0 (Raylight scattering), while the second term represents Raman scattering of frequency $\nu_0 + \nu_m$ (anti-Stokes) and $\nu_0 - \nu_m$ (Stokes). In conclusion, a vibration is Raman-active if the polarizability changes during vibration, $(\delta\alpha/\delta q)_0 \neq 0$. (65; 66)

An electric field can induce dipole components in each of the directions (x, y, z). Thus, the polarisability is a tensor:

$$\begin{pmatrix} P_x \\ P_y \\ P_z \end{pmatrix} = \begin{pmatrix} \alpha_{xx} & \alpha_{xy} & \alpha_{xz} \\ \alpha_{yx} & \alpha_{yy} & \alpha_{yz} \\ \alpha_{zx} & \alpha_{zy} & \alpha_{zz} \end{pmatrix} \begin{pmatrix} E_x \\ E_y \\ E_z \end{pmatrix} \tag{5}$$

This is important for the measured Raman intensity, which is depending on the orientation of a molecule or crystal and the polarization of the incident laser beam:

$$I \sim |e_i \cdot \Re \cdot e_s| \qquad (6)$$

where e is the polarization direction of the electric field of the incident (e_i) and scattered (e_s) light and $\Re$ is the Raman tensor, which reflects the symmetry of the molecule or crystal. By measuring Raman intensities in parallel ($e_i \parallel e_s$) and cross ($e_i \perp e_s$) polarization configurations, information on the molecule or crystal orientations can be obtained. (67; 68)

The theory described above is a simplification used to explain vibrations and the Raman effect in molecules. However, in this work Raman spectroscopy was applied to study different CVD coatings, i.e. crystalline solids. Therefore the vibrational spectra need to be defined by a frequency distribution. This can be illustrated by using a simple one-dimensional, crystalline, diatomic, linear lattice. (65; 69; 70)

For a one-dimensional, infinite chain consisting of atoms with alternating masses M and m, separated by the distance a with a force constant f, two neighboring atoms are located at the lattice points $2n$ and $2n$+1. The equations of motion for the corresponding displacements u_{2n} und u_{2n+1} are given by:

$$M\, u_{2n} = f\,(u_{2n+1} + u_{2n-1} - 2\, u_{2n}) \qquad (7)$$

$$m\, u_{2n+1} = f\,(u_{2n+2} + u_{2n} - 2\, u_{2n+1}) \qquad (8)$$

with u_{2n} and u_{2n+1}:

$$u_{2n} = y_1 \exp\,[i(2\pi\nu t + 2nka)] \qquad (9)$$

$$u_{2n+1} = y_2 \exp\,\{i[2\pi\nu t + (2n+1)\,ka]\} \qquad (10)$$

where k is the wave vector, which corresponds to the phase differences for each successive cell. Two equations for the amplitudes y_1 and y_2 are obtained, and the solution for these equations leads to the secular determinant:

$$\begin{vmatrix} 2f - 4\pi^2\nu^2 M & -2f\cos ka \\ -2f\cos ka & 2f - 4\pi^2\nu^2 m \end{vmatrix} = 0 \tag{11}$$

for which a dispersion formula results, based on the frequency dependency on masses, the force constant and the distance between the two masses:

$$\nu^2 = 1/4\,\pi^2[(f/\mu) \pm ((f^2/\mu^2) - (4f^2 \sin^2 ka)/Mm)^{1/2}] \tag{12}$$

where μ is the reduced mass. The value of k is restricted by the finite length of the lattice between $-\pi/2a \leq k \leq \pi/2a$, called the first Brillouin zone (69; 70). In the limit of small ka, two solutions for ν can be obtained, corresponding to the optical and acoustical branches:

$$\nu = 1/2\pi(2f/\mu)^{1/2} \tag{13}$$

$$\nu = 1/2\pi[2f\,(M+m)]^{1/2}\,ka \tag{14}$$

The optical branch is so-called because it represents frequencies occurring in the optical spectral region (infrared or Raman), whereas for the acoustical branch, which passes through $\nu = 0$, the frequencies correspond to the sonic or ultrasonic region (Fig. 8). (65; 69; 70)

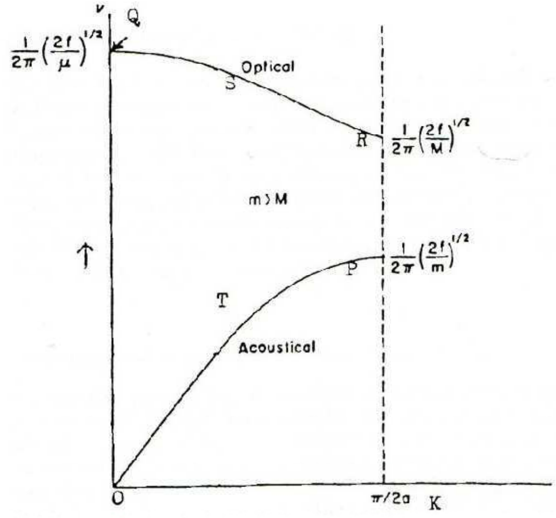

Fig. 8: Dispersion curves in the positive half of the first Brillouin zone for the longitudinal vibrations in a diatomic chain (65; 70).

In addition to the above described longitudinal vibrations also transversal vibrations (displacement of atoms perpendicular to the chain with a bending force constant f_{α}) need to be considered in a three-dimensional motion of a diatomic chain consisting of atoms with alternating masses M_1 and M_2. These can take place in two dimensions (two planes in right angle to another), and therefore one pair of dispersion curves (acoustical and optical branch) in each direction in space (transversal and longitudinal) is obtained (see Fig. 9). (69; 70)

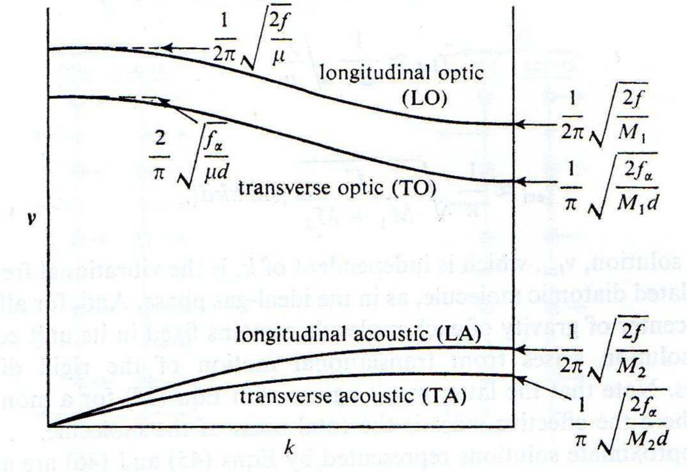

Fig. 9: Dispersion curves of longitudinal and transversal modes of a diatomic chain **(70)**.

In the case of a crystal with N atoms and n atoms per unit cell, 3N normal modes of vibration on 3n branches are observed of which 3 modes are acoustical and 3n-3 are optical modes.

In addition to classical considerations, the Raman effect can be explained according to the quantum theory (71). Here, it is based on the inelastic light scattering with energy and momentum transfer between the photons and scattering material. The energy of the photon is described as $E = h\nu_i$ and the momentum as $p = hk_i$. The interaction results either in an increase or decrease of the scattered photon energy ($h\nu_s$) as well as a momentum transfer (see Fig. 10).

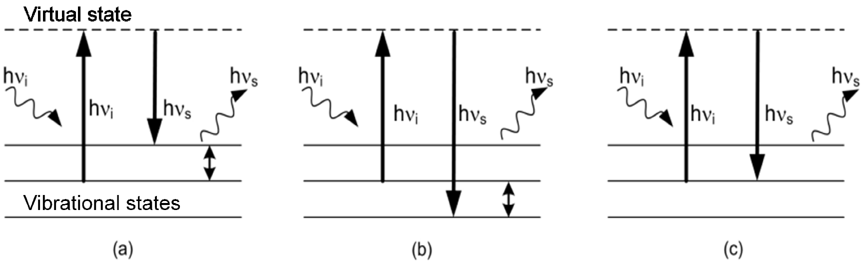

Fig. 10: The Raman effect: (a) Stokes, (b) Anti-Stokes, (c) Rayleigh **(68)**.

The Raman process can thereby be separated into three steps (68; 71; 72):

1. An incoming photon with frequency ν_i and wave vector k_i is absorbed, and the absorbing material is excited from its initial state i into an intermediate virtual state v.

2. An elementary excitation is created (Stokes) or annihilated (anti-Stokes) with a wave vector q and frequency ν.

3. The material undergoes a transition from the intermediate state v to the final state f, which is accompanied with the emission of a scattered photon (k_s, ν_s).

These three steps can occur all within the time limited by the Heisenberg uncertainty. Furthermore, the Raman effect can be described by all the possible permutations of these interactions resulting in six typical processes (Feynman's Theory). However, the above shown order presents the most important contribution. A phonon is thus created with energy and momentum transfer ($h\nu$ and hq) to or from the material. In the case of first-order Raman scattering, the energy and momentum conservation rules then lead to:

$$h\nu_s = h\nu_I \pm h\nu \tag{15}$$

$$k_s = k_i \pm q \tag{16}$$

If the energy transfer $h\nu$ from the photon to the material is positive (Stokes), the final state is above the initial state, otherwise the material transfers energy to the photon (anti-Stokes). (71)

For standard Raman experiments in solids with backscattering geometry k_s and thus q_{max} (= $2k_s$) is about 1000 times smaller than characteristic wave vectors of phonons. As a result, first-order Raman scattering experiments can only probe excitations in the limit $q \approx 0$. (69; 70; 71)

For second- and higher-order processes ν_s becomes the sum of the frequencies of two or more quanta, and the total wave vector k_s is (72):

$$k_s = \sum_j q_j \tag{17}$$

The summation is carried out over all elementary excitations, and q_j can range from zero to values at the Brillouin zone boundary. In second- and higher-order processes the prominent spectral features are known to be related to structures in the density of states (DOS) of the respective modes. (72) An experimental determination of the DOS is obtained by inelastic neutron scattering, which provides in general a good agreement to the Raman results (70).

Defect-induced Raman scattering

In imperfect crystals with a small concentration of defects, the energy and momentum conservation rules presented in Eq. (15)-(17) breaks down since the medium has no translation symmetry (or in quantum mechanical words, the Bloch theorem does not apply). Here, the first-order Raman spectra are expected to display features reflecting the DOS of the particular excitation. (72) The detailed theory of defect-induced phonon spectra is well established and can be found in (73; 74).

As an example for this correlation between first-order Raman scattering and the DOS, the here studied titanium carbides and nitrides need to be mentioned. Actually, first-order

Raman scattering is forbidden in stoichiometric TiN and TiC due to their cubic structure with a center of inversion symmetry and the mutual exclusion principle (65; 72). However, it is known that CVD coatings contain a certain amount of crystallographic defects, typically (see Chapter 2.2). These point defects reduce the effective local symmetry due to atomic displacements of neighboring atoms, and thus non-zero first-order polarizability derivatives become possible. Spengler et al. (43; 44; 45) have shown that such vacant ion positions can induce first-order Raman scattering in transition-metal carbides as well as nitrides. It was found, that the first-order Raman spectra are thereby directly proportional to the phonon density of states and a very good agreement between peaks in the Raman spectra and data collected by neutron scattering was obtained. The peaks in the acoustical range (typically 150-300 cm^{-1}) have been attributed primarily to vibrations involving the heavy Ti ions (longitudinal acoustical LA- and transversal acoustical TA- modes), whereas peaks in the optical range (400-650 cm^{-1}) have been attributed to the light-weight N and C ions (longitudinal optical LO- and transversal optical TO- modes). (35; 42; 43; 44; 45; 46; 47; 48)

Generally, it is known the main factors responsible for changes in defect-induced Raman spectra at a given temperature are the chemical composition, grain size, defects and internal stress in the sample (46). Especially in solid solutions like Ti-C-N, composition changes are assumed to primarily affect the peak positions due to changes in the lattice constant. The FWHM is expected to be correlated to the grain size and the total intensity of the Raman peaks is primarily determined by the defects concentration, thus a higher amount of defects in the coating is supposed to lead to higher total peak intensity. Furthermore, internal stresses may also affect the frequency and FWHM of the Raman peaks. (35; 42; 43; 44; 45; 46; 47) Such effects were examined in this work for the Ti-C-N and Ti-B-C-N coatings (see Chapter 4.1.1).

Temperature effects on Raman spectra

Different effects of temperature changes on first-order Raman scattering are known. These are for example the variation of the intensity ratio between Stokes and anti-Stokes scattering, as well as Raman peak shifts. At room temperature, Stokes Raman scattering is in general more intense, since most molecules and atoms are in the ground state. At elevated temperatures, the excited vibrational states will be more populated, and therefore the anti-Stokes signal will become more intense. Thus, the intensity ratio between Stokes and Anti-Stokes scattering is a function of the sample temperature (67):

$$I_A/I_S = [(\nu_0+\nu)/(\nu_0-\nu)]^4 \exp(-h\nu/kT) \tag{18}$$

Balkansi et al. (75) reported a further effect of temperature changes on Raman spectra of crystals. They observed a shift in wavenumber, which arises as a result of the contraction or expansion of crystal lattices upon heating or cooling. Therefore, here the temperature dependence of the anharmonicity of the interatomic potentials needs to be considered. With increasing temperatures, the Raman peaks shift toward lower wavenumbers. At temperatures < 1000K the nonlinear dependence of Raman peak positions as a function of temperature given by Balkansi et al. can approximatly be linearized (76; 77):

$$\Delta\omega(T)/\mathrm{cm}^{-1} = -C\cdot\Delta T/K \tag{19}$$

where C is the temperature coefficient, depending on material specific parameters. It should be mentioned that, although not examined in this work, in addition to the peak position the line widths of the Raman peaks can change (broaden) with increasing temperature (76; 77).

Especially in Raman micro-spectroscopy experiments, where the laser beams are focused to a spot size with a diameter of only a few micrometers ($d = 1.22\lambda/NA$ (78)), the local temperature at this point of measurement may increase by hundreds of degree Celsius owing to the absorption of radiation (79). This can cause a wavenumber shift of Raman modes as described above, and in addition also laser-induced oxidation can occur. Such an effect was examined in this work for the Ti-B-N coatings (see Chapter 4.4).

2.3.2 X-ray diffraction (XRD)

X-ray diffraction (XRD) is a commonly used analytical method for the characterization of hard coatings. It is based on the elastic scattering of X-rays from the electron clouds of the individual atoms and can be used to determine information about the crystallographic structure (lattice constants), chemical composition, crystallite size (grain size) and preferred orientation (texture). (60)

Bragg's law is the fundamental equation for XRD which defines constructive interference, i.e. certain angles under which X-ray diffraction occurs for a crystalline body:

$$n \lambda = 2 d \sin \theta \tag{20}$$

where n is an integer, λ the wavelength of incident wave, d the spacing between the planes in the atomic lattice, and θ the angle between the incident ray and the scattering planes. (67)

Phase identification

In XRD patterns, both the positions (corresponding to lattice constants) and the relative intensity of the peaks provide a "fingerprint" of a crystal. To identify different substances, diffraction data can be compared to a database maintained by the International Centre for Diffraction Data (ICDD). (60)

Lattice parameters

The position of a diffraction peak (d) is determined by the size of the unit cell of the crystal. Each peak corresponds to a certain lattice plane and can therefore be characterized by a Miller index. If the symmetry is high, e.g. cubic or hexagonal like in the here studied titanium coatings, the index of each peak can be easily identified and the corresponding lattice constants (a, c) can be calculated as follows (60; 80):

Cubic: $$a = d\,(h^2+k^2+l^2)^{1/2} \tag{21}$$

Hexagonal: $$a = d\,[(4/3)\cdot(h^2+k^2+hl) + l^2/(c/a)^2]^{1/2} \tag{22}$$

Especially for solid solutions like the examined Ti-C-N coatings, it is known (60; 61) that the lattice parameters show a linear dependence on the composition within the range from TiN to TiC (see also Chapter 2.2.2). This linear dependence is described through Vegard`s law (81). Thus, lattice constants can be used to estimate coatings compositions, or rather nitrogen or carbon concentrations (60):

$$C_{phase1}\ [\text{at.\%}] = (a_{phase2} - a_{phase1+2}) / (a_{phase2} - a_{phase1}) \tag{23}$$

However, the results obtained by this method can only be used for a coarse classification, since the titanium as well as the C+N concentration is here always assumed to be exactly 50 at.%. This is often not right for coatings deposited by CVD or PVD due to small amounts of additional amorphous phases (see Chapter 4.1.1).

Size of Crystallites

Crystallite size changes are indicated by a broadening or narrowing of the peaks in an X-ray diffraction (60; 82). According to the Scherrer Equation (83) the broadening of a peak in a diffraction pattern can be used to determine the size of crystals (D) in a solid:

$$D = K\,\lambda / \beta \cos\theta \tag{24}$$

where K is the shape factor , λ is the x-ray wavelength, β is the line broadness at half the maximum intensity (FWHM) in radians, and θ is the Bragg angle. The dimensionless shape factor has a typical value of ~ 0.9 (84).

In addition to XRD, grazing-incidence XRD (GIXRD) can be used to determine thicknesses and composition of oxide layers. By changing the angle of incidence (0.5-4°)

the penetration depth can be varied (e.g. 0.13 - 1.3 µm in the case of pure TiO_2 (85)), and near surface information as well as depth profiles can be obtained. (60)

2.3.3 Wavelength-dispersive X-ray spectroscopy (WDS)

Wavelength-dispersive X-ray spectroscopy (WDS) is a microphysical method for identifying the elemental composition of materials. In the field of materials science it is often used for determining the nitrogen, carbon and boron concentration in transition-metal compounds (49). It takes advantage of the characteristic X-rays generated by individual elements to enable quantitative analyses (down to trace element levels) measured at spot sizes of a few micrometers. The technique is complementary to energy-dispersive spectroscopy (EDS), but WDS spectrometers have a significantly higher spectral resolution and the low energy $B_{K\alpha}$, $C_{K\alpha}$ and $N_{K\alpha}$ radiation can easily be detected. Furthermore, WDS exhibits an enhanced quantitative potential by analyzing only one specific element. (86; 87)

A quantitative analysis with a wavelength-dispersive spectrometer involves following steps (86; 87; 88):

Exciting an atom to emit X-rays

To generate characteristic X-rays for the analyzed elements, electrons are accelerated in an evacuated electron column to the sample surface with sufficient energy (typically with a potential difference of 10-20 kV).

Focusing the X-rays by an analytical crystal to the detector

The generated X-rays are selected using analytical crystals with specific lattice spacings (86). The geometry of the X-ray generating sample and the analytical crystal thereby maintains a constant take-off angle. When the X-rays encounter the analytical crystal at a specific angle Θ, only those X-rays are reflected which satisfy Bragg's Law. Thus, only a single wavelength is passed on to the detector. Two types of analytical geometry are typically used, the Johann and the Johansson geometry. In the first one the analytical crystal is bended to a radius of 2R, where R is the radius of the focusing circle (see Fig. 11, Rowland Circle). In the latter one the crystal is bent to a radius 2R and ground to radius R. In this way all points of reflection lie on the Rowland circle, which maximizes the collection efficiency of the spectrometer. (86; 87)

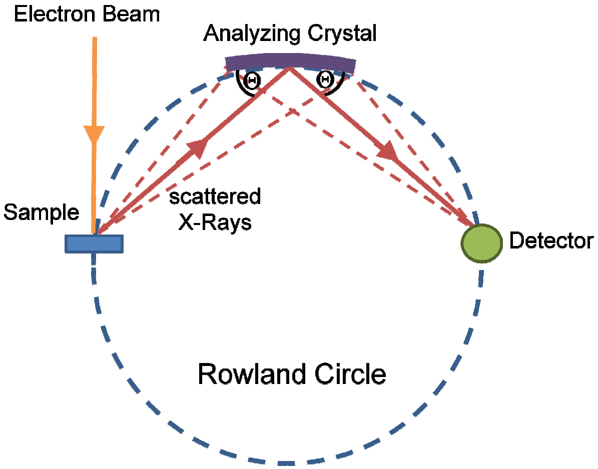

Fig. 11: Configuration of sample, analytical crystal and detector on the Rowland circle **(87)**.

Converting X-rays to photoelectrons

X-rays of specific wavelengths from the analytical crystal are passed on to the X-ray detector (gas proportional counter type). The incoming X-rays enter the detector through a collimator, get absorbed by atoms of the counter gas, and a photoelectron is emitted by each atom absorbing an X-ray. The photoelectrons are accelerated to a central wire and the additional ionization produces an electrical pulse with an amplitude proportional to the energy of the original X-ray photon. (86; 87; 88)

Once the x-ray intensities of each element of interest are counted in a detector at a specific beam current, the count rates are compared to those of standards containing known values of the elements of interest. The results are then given as a function of the weight % of the elements, which can easily be converted into atomic %.

2.3.4 Tribology

Tribology is the science of interaction of surfaces in relative motion. It deals with friction, wear and lubrication and is therefore an interdisciplinary field of physics, chemistry and materials science. (52; 67; 89; 90; 91; 92)

Friction

Friction is the force resisting the relative motion of solid surfaces sliding against each other (90; 92). The friction force and coefficient of friction are usually measured by a tribometer (Fig. 12). A typical set-up consists of a stationary ball under an applied load in contact with a rotating disc.

The friction coefficient μ is defined by the ratio of the frictional force F or shear stress τ to the loading force L or compressive stress σ on the ball (90):

$$\mu = F/L \tag{25}$$

F is thereby primarily determined by the energy of adhesion:

$$F = (d\gamma_{ad}/dx) \cdot A \tag{26}$$

where A is the effective contact area. Furthermore, elastic and plastic deformation γ_e and γ_p, crack formation γ_f , tribochemical reaction γ_c as well as the hardness H and roughness R have an influence. μ can therefore be written as (90):

$$\mu = [(d\gamma_{ad}/dx) + (d\gamma_e/dx) + (d\gamma_p/dx) + (d\gamma_f/dx) + (d\gamma_c/dx)]\, R\sigma/H \tag{27}$$

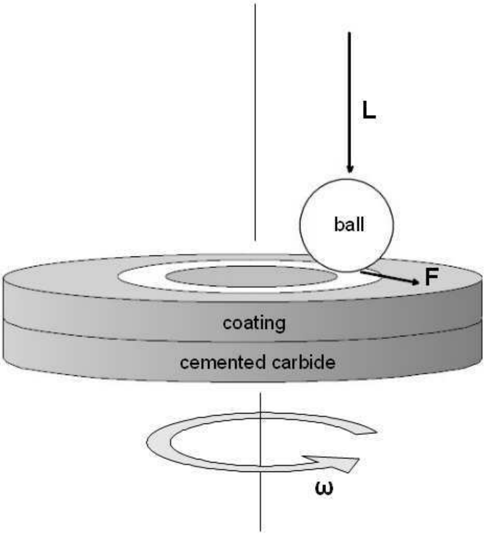

Fig. 12: Typical set-up of a tribometer. A stationary ball under an applied load is sliding on a rotating coating surface (L = loading force, F = frictional force, ω = rotational speed).

Wear

Wear is the loss of material resulting from the mechanical interaction of two sliding surfaces under load. It can coarsely be separated in adhesion, abrasion and tribochemical reactions. Adhesive wear is the most common type, which arises from material transfer from one surface to another during sliding. As a result, wear particles and transfer layers are formed on the wear tracks. Abrasive wear occurs when a hard, rough surface slides over a softer one, producing grooves on the latter. Severe abrasive wear can also result in surface fatigue by crack formation or even in form of flanking. Tribochemical reactions are chemical reactions occurring at the contact interface between the environment (oxygen, moisture, etc.) and the rubbing surfaces. One special case is for example tribooxidation, which can take place because of the increased temperatures during sliding due to the tribomechanical stress conditions prevailing at the fretting contact in ambient air. (67; 89; 91) A convenient way to distinguish the kind of wear behavior of a coating is to inspect the wear track by an optical microscope.

Lubrication

Lubrication includes any type of substance between sliding surfaces which reduces wear and friction. Such substances can be divided into fluid or solid lubricants. Since in this work only dry sliding tests were performed, in-situ formed solid lubricants are of interest. Solid-lubricants are often layer-lattice solids, e.g. materials such as graphite, molybdenum disulfide or boron nitride which have a crystal lattice structure arranged in layers. Strong bonds between atoms within a layer and relatively weak bonds between atoms of different layers allow the lamina to slide on one another. (67; 90; 93)

In the case of Ti-B-N coatings, possible solid lubricants are rutile, Magnéli-phases of titanium oxide (Ti_nO_{2n-1}) or boric acid. Further information about these substances can be found in (94; 95; 96; 97; 98; 99; 100; 101; 102; 103).

2.3.5 Further used analysis methods

In addition to the above described analysis methods, Scanning electron microscopy (SEM) was used to evaluate the fracture and surface morphology of some coatings. Detailed description of this technique can be found in (86). Furthermore, X-ray photoelectron spectroscopy (XPS) was applied to determine the binding properties and surface composition of the Ti-B-N coatings. Detailed description of this technique can be found in many PhD theses in the group of Prof. Dr. T. Chassé as well as in several textbooks (68; 104; 105; 106).

3. Experimental

3.1 Coating deposition

All investigated samples were coated cutting tools provided by the WALTER AG Tübingen. The different coatings were deposited onto cemented carbide inserts (ISOP10 grade with CNMA120412 geometry) using a Bernex BPX325S production scale low-pressure CVD system. Precursor flow rates were monitored by mass flow and liquid flow controllers. Deposition of all coatings started with an adhesive TiN base layer of 0.3 to 0.5 µm thickness. The main functional layers are of 5-8 µm thickness. Coating thicknesses were measured using the ball crater method (5; 6; 15; 16; 107). The statistical distribution was evaluated by measuring the coating thickness of 12 - 15 inserts evenly sampled from a full load of ~ 2500.

$TiC_{1-x}N_x$ coatings were deposited at 1015°C (HTCVD) using $TiCl_4$, CH_4 and N_2 as precursors and H_2 as the carrier gas. Different carbon and nitrogen concentrations in the coatings were obtained by varying the N_2:CH_4 ratio in the gas phase. These coatings will later be introduced as A-series.

Furthermore, $TiC_{1-x}N_x$ coatings were deposited at 850 - 1000°C (MTCVD) using CH_3CN as precursors instead of CH_4 and N_2 (a-series).

The $TiB_xC_yN_z$ coatings were deposited at 1015°C (HTCVD) using $TiCl_4$, CH_4, BCl_3 and N_2 as precursors as well as H_2 as the carrier gas. On the top of the $TiB_xC_yN_z$ layers an additional Ti-B-N (9 at.% B) layer of approximately 1 µm thickness was applied. In the design of CVD multilayer coatings on cutting inserts it is a common practice to cover dull or dark colored outer wear protecting layers with top layers of ≤ 1 µm thickness which have a brighter color for the purpose of wear indication, facilitating the differentiation between used and unused cutting edges. Two different series of HT-$TiB_xC_yN_z$ coatings were generated: first the BCl_3 concentration in the gas phase was kept constant (60 sccm) and the N_2:CH_4 ratio was varied from 0.25 - 18 (B-series). In the second series the N_2:CH_4

ratio was kept constant at 18, whereas the BCl_3 concentration in the gas phase was varied between flow rates of 0 - 240 sccm (C-series).

MT-$TiB_xC_yN_z$ coatings were deposited at 900°C using CH_3CN as precursor and varying BCl_3 concentrations in the gas phase between 20 - 240 sccm (c-series). Two coatings of this series (those deposited with 30 and 60 sccm BCl_3) exhibit again an additional wear-indicating Ti-B-N (9 at.% B) top layer.

For the deposition of the Ti-B-N coatings, $TiCl_4$ and N_2 were used as precursors as well as different flow rates of BCl_3 (30 - 480 sccm). The deposition temperature was set to 850°C (D-series).

The references coatings TiN, TiC and TiB_2 for XRD, WDS and Raman analysis were prepared in the same LPCVD system in order to ensure the comparability.

Detailed deposition parameters for the investigated coatings can be found in the appendix (Table 16, p.135).

3.2 Hardness measurements

For most coatings Vickers microhardness tests were performed by the WALTER AG Tübingen with a Fischerscope H100VP ultramicrohardness tester on plane polished metallographic cross sections (1 µm diamond paste in the final polishing step). The indenter was positioned in the central part of the main functional coating layer and at least ten indentations were performed and averaged on each cross section (107). The load was 100 mN for 20 s. The deviation is estimated to be lower than ±100 HV. Results are given in the appendix (Table 16, p.135).

Further details on deposition parameters, as well as coating thickness and hardness measurements for $TiC_{1-x}N_x$ and $TiB_xC_yN_z$ coatings can be found in (5; 6). Details on Ti-B-N coatings are given in (15; 16).

3.3 Syntheses of reference samples

Due to the deposition by an industrial LPCVD process, the surface layer of the TiB_2 coatings typically contains impurity phases (15). Thus, for the surface sensitive analysis methods WDS, XPS and Raman spectroscopy, an additional TiB_2 reference sample was synthesized. Furthermore, TiB, $FeBO_3$ and $TiBO_3$ were synthesized as reference samples for Raman measurements. All materials were made at the Institute für Anorganische Chemie, Universität Tübingen with the aid of Dr. J. Glaser.

Synthesis of TiB_2 and TiB

Appropriate quantities of Ti powder (purum, >98.5 %, Fluka) and B (crystal powder, 99.7 %, ABCR) were mixed thoroughly in an agate mortar. The mixtures (~ 100 mg) were pressed into pellets 6 mm in diameter and 1-2 mm in height. The pellets were arc welded under inert-gas atmosphere for several seconds in a water-cooled copper block. Reaction products were inspected by powder XRD (STOE StadIP) using germanium-monochromated $Cu\text{-}K_{\alpha 1}$-radiation. For mixtures containing Ti : B = 1 : 2, XRD patterns show only TiB_2 reflections. Hexagonal indexing resulted in lattice parameters of a = 3.0300(8) Å and c = 3.2294(7) Å, in accordance with literature data (108). For mixtures containing Ti : B = 1 : 1, XRD patterns show TiB as the main phase and TiB_2 (ca. 10 wt %) as a by-product. Orthorhombic indexing resulted in lattice parameters of a = 6.115(1) Å, b = 3.0541(5) Å, and c = 4.5616(9) Å. The values are in good agreement with previously published data (109).

Synthesis of $FeBO_3$

For $FeBO_3$, FeB (> 98%, Alfa Aesar) was heated in a corundum crucible for 60 h at 800 °C in a furnace under ambient conditions. Reaction products were inspected by powder XRD (STOE StadIP) using germanium-monochromated Cu-$K_{\alpha1}$-radiation. XRD patterns showed only $FeBO_3$ related reflections. Trigonal indexing resulted in lattice parameters of $a = 4.627(3)$ Å und $c = 14.48(2)$ Å, which are in good accordance with literature data (110).

Synthesis of $TiBO_3$

A boron covered Ti foil (B crystal powder, 99.7 %, ABCR; Ti 99.6+%, Goodfellow, 20x10x0.05 mm) was heated in a corundum crucible for 60 h at 1000 °C under a continuous argon flow. XRD investigation of the product showed reflections of $TiBO_3$, which were identified by comparison with the ICDD entry 85-165 (111).

Additional reference substances (B_2O_3, H_3BO_3, and TiO_2) were purchased from Sigma Aldrich and Alfa Aesar in reagent-grade purity.

3.4 Analysis methods

3.4.1 Raman spectroscopy

Raman spectra were recorded with a Jobin-Yvon LabRam HR800 confocal Raman spectrometer, equipped with a 600 l/mm grating and a CCD camera. The samples were excited using the 532.2 nm line from a frequency-doubled Nd-YAG laser in backscattering geometry with a spectral resolution of about 2 cm^{-1} and varying laser powers between 1.6 - 16 mW at the samples. All spectra shown in this work of TiN, TiC and $TiC_{1-x}N_x$ and $TiB_xC_yN_z$ were recorded with a laser power 8 mW except otherwise noted. For TiB_2 and the Ti-B-N coatings a laser power of 4 mW was used. The boron-rich coatings were thereby placed in a small glass cell under a flowing stream of argon to prevent laser-induced oxidation (see Chapter 4.4). The oxidized coatings as well as the tribotested samples were analyzed with 1.6 mW. Micro sampling was accomplished with an Olympus 100× objective (numerical aperture of 0.9) and a laser beam focal point diameter ($d = 1.22\lambda/NA$ (67)) of approximately 0.7 µm. The information depth ($d=\lambda/4\pi k$, where k is the extinction coefficient (35)) can be estimated to be in the sub-micrometer range (e.g. TiN ≈ 25 nm, TiO_2 ≈ 1 µm (112)) for the here studied titanium coatings.

In the case of the $TiB_xC_yN_z$ coatings, the high lateral resolution (< 1µm) allowed measurements in calottes or cross-sections to detect only the $TiB_xC_yN_z$ layer without any interfering signals of the top Ti-B-N or the TiN base layer. Spectra were taken from at least ten different points of the coatings to obtain consistent data sets.

The energetic positions, intensities, areas and full width at half maximum (FWHM) of the Raman peaks were determined using commercial software (Labspec 4.02, Horiba/Jobin-Yvon, Kyoto, Japan) by applying mixed Gaussian/Lorentzian peak functions (113; 114). The experimental error of this method can be estimated to ± 2 cm^{-1}.

3.4.2 X-ray diffraction analysis (XRD)

The microstructure, chemical composition, crystallite size and lattice parameters were investigated by applying Bragg-Bretano X-ray diffraction analysis. $TiC_{1-x}N_x$ coatings were analyzed twice with a Siemens D5000 diffractometer using Cu-K_a radiation at the Institut für Mineralogie, Universität Tübingen by Dr. C. Berthold as well as with a Bruker D8 GADDS using Co-K_α radiation (5; 6). The $TiB_xC_yN_z$ and Ti-B-N coatings were analyzed at the WALTER AG Tübingen with a PTS3003 diffractometer (GE Inspection Technologies) using Cu-K_α radiation (40 kV, 40 mA) and a Ni filter from 20° to 100° at a scanning rate of 0.025°/3s. To separate the overlapping peaks of the adhesive TiN layer (and in the case of the $TiB_xC_yN_z$ coatings also of the top Ti-B-N layer) least-squares fits to experimental points were carried out based on pseudo-Voigt functions (82). The overlapping $K_{\alpha1}$- and $K_{\alpha2}$-lines of the peaks were separated and the $K_{\alpha1}$-peaks were used for analysis. Lattice constants were calculated from the (111), (200) and (220) reflections of the cubic phases, as well as from the (100) reflection of the hexagonal phases. The uncertainty for the obtained values was found to be < 0.1 %.

To estimate the compositions of the coatings from the $TiC_{1-x}N_x$ series by XRD lattice parameter measurement using Vegard's law (81), TiN and TiC samples prepared in the same LPCVD system were used as references to ensure comparability. The uncertainty of this method can be estimated to be about ± 10% (30).

Grazing-incidence XRD (GIXRD) experiments were performed on a PTS3003 diffractometer (GE Inspection Technologies) to obtain surface informations as well as depth profiles of oxidized coatings. The angle of incidence was varied from 0.5 - 4° corresponding to a penetration depth of 0.13 - 1.3 µm in the case of pure TiO_2 (85).

3.4.3 Wavelength dispersive X-ray spectroscopy (WDS)

The chemical compositions of the coatings were determined by WDS using a JEOL Superprobe jx8900R instrument (10 kV, 20 mA, diameter of excitation volume ~ 1µm) at the Institut für Mineralogie, Universität Tübingen by Dr. T. Wenzel. Detailed description of the set-up and measurements conditions can be found in (115). At least five measurements were performed at different positions on the coatings, and the results were averaged. TiN, TiC coatings as well as a TiB_2 reference sample were used as standards for calibration. LDE1H, LDEB, and PETH were used as analyzing crystals for N, C, B and Ti, respectively (86). The deviation from the analytical total was found to be ± 2 wt%. This can most likely be explained by deviations from planar surfaces (porosity and roughness of a sample significantly affects the analytical total (115)) as well as heterogeneity of the TiB_2 standard which causes an uncertainty in boron of about 10%. Furthermore, a problem of the examined coatings was the close overlap of the titanium L1-line with the $N_{K\alpha}$-line, which cannot be separated by diffraction methods (49). Since for the analysis in this work no titanium-free nitrogen standard was available, a correction of the $L1+N_{K\alpha}$ peak was not possible. The uncertainty of nitrogen was therefore experimentally determined to be about 3 %.

3.4.4 Scanning electron microscopy (SEM) and optical micrographs

A scanning electron microscope (SEM, Zeiss SigmaVP), equipped with an energy dispersive X-ray spectrometer (EDX, Oxford INCA x-act), was used at the WALTER AG Tübingen to evaluate the fracture and surface morphologies of the coatings. In addition, SEM images (SEM, Zeiss DSM 962) were taken in secondary-electron contrast mode at the Institut für Physikalische Chemie, Universität Tübingen by E. Nadler. Optical micrographs are from the WALTER AG Tübingen by M. Schaible.

3.4.5 X-ray photoelectron spectroscopy (XPS)

XPS was used to determine the surface composition of the Ti-B-N coatings. The set-up consisted of a Specs XR 50 Mg-K_{α} x-ray source and a Specs PHOIBOS 100 hemispherical energy analyzer. The pass energy was set to 30 eV for the recording of all spectra. Prior to being transferred into the vacuum system, the samples were polished, but no further sputtering step was performed. Special attention was paid to the titanium 2p, boron 1s and nitrogen 1s core-levels. Since the samples were deposited by an industrial LPCVD process, the surfaces show contaminations like adsorbed carbon species as well as titanium, boron and nitrogen oxides. The measurements and analysis of the spectra were performed at the Institut für Physikalische Chemie, Universität Tübingen by C. Raisch.

3.5 Static oxidation

Heat treatment was typically performed with a Heraeus thermicon P furnace in ambient air at 300°C, 500°C and 700°C for 0.5, 1 and 3 h.

3.6 Tribological tests

Dry-sliding tribological tests were performed at 25, 300, 500 and 700°C against steel and alumina balls (100Cr6, Al_2O_3, 6 mm diameter) using a CSM high-temperature tribometer. The tests were performed in ambient air with a relative humidity of ~ 35 % using SPNN150408 inserts. The time to reach 700°C takes about 35 min. Prior to testing the inserts were polished to mirror shine with 3 µm diamond suspensions and cleaned with ethanol. Normal load, sliding speed and wear-track-radius were kept constant at 7 N, 7.5 cm/s and 3 mm. The sliding distance was 300 m in order to determine the friction coefficient after running-in. An average value was taken from 3 measurements. In addition, sliding distances of 0.3 m were used to determine tribochemical reactions at the contact interface. Turning tests against 100Cr6 bearing steel using CNMA120408 inserts with a P20 grade substrate were done without coolant at the following conditions: Cutting speed v_c: 150 m/min, 180 m/min, 200 m/min; feed f: 0,32 mm; depth of cut a_p: 2,5mm; cutting time 3 min.

4. Results and Discussion

In the following chapters the results obtained for different CVD coatings deposited in the $TiC_{1-x}N_x$, $TiB_xC_yN_z$ and Ti-B-N systems will be presented. The coatings were thereby studied with respect to their compositions, oxidation and tribological behaviors, mainly by means of Raman spectroscopy, XRD and WDS, but also by SEM. Furthermore, XPS experiments were performed for the Ti-B-N coatings.

Compared to XRD, WDS, SEM and XPS, which are all well established analysis methods for the characterization of CVD coatings, Raman spectroscopy is up to now not commonly used. Therefore, the results of the different techniques will be compared and correlated, in order to demonstrate the advantages of Raman spectroscopy in the study of such samples. The findings will be discussed in terms of the properties of the different coatings.

For further discussions the different HTCVD coatings will hereafter be labeled with capital letters as follows:

A-series - $TiC_{1-x}N_x$ coatings with varying C:N ratio.

B-series - $TiB_xC_yN_z$ coatings with varying C:N ratio.

C-series - $TiB_xC_yN_z$ coatings with varying B concentration.

D-series – Ti-B-N coatings with varying B concentration.

The corresponding MTCVD $TiC_{1-x}N_x$ and $TiB_xC_yN_z$ coatings will be denoted with lower case letters (a- and c-series).

4.1 $TiC_{1-x}N_x$ and $TiB_xC_yN_z$ coatings

First, coatings deposited in the $TiC_{1-x}N_x$ and $TiB_xC_yN_z$ systems will be discussed. They were analyzed using WDS, XRD, SEM and Raman spectroscopy with regard to different compositions. Therefore, the C:N ratio in the $TiC_{1-x}N_x$ (A1-A5) and $TiB_xC_yN_z$ (B1-B5) coatings was systematically changed as well as the boron concentration in $TiB_xC_yN_z$ coatings (C1-C5). Furthermore, different deposition techniques were chosen: high- and moderate-temperature CVD. MTCVD thereby refers to all coatings deposited by CH_3CN, although the deposition temperature was actually varied between 850-1000°C in the case of $TiC_{1-x}N_x$ coatings (a1-a4). For MT-$TiB_xC_yN_z$ coatings, the BCl_3 flow rate during the CVD process was systematical changed (20-240 sccm; c1-c5).

The results of the different analysis methods for the full set of samples will be correlated in order to demonstrate the analytical power of Raman spectroscopy for the characterization of these kinds of coatings.

4.1.1 High-temperature CVD coatings (A-, B- and C-series)

Deposition and microhardness

The known CVD reaction for the formation of HT-$TiC_{1-x}N_x$ proceeds according to the following equation:

$$TiCl_4 + 1/2x\ N_2 + 1\text{-}x\ CH_4 + 2x\ H_2 \rightarrow TiC_{1-x}N_x + 4HCl \qquad (x: 0\text{-}1)$$

As apparent from this equation, in HTCVD processes the C:N ratio in $TiC_{1-x}N_x$ coatings can easily be changed by varying the N_2:CH_4 precursor ratio in the gas phase.

This possibility was applied for the here studied $TiC_{1-x}N_x$ coatings A1-A5, where the N_2:CH_4 ratio was varied between 18 and 0.25 during the CVD process. It was found, that the microhardness of $TiC_{1-x}N_x$ coatings A1-A5 increases about linearly with the carbon concentration from 1800 HV in TiN to 2900 HV in TiC (see appendix Table 16, p. 135).

For the deposition of $TiB_xC_yN_z$ coatings B1-B5 an additional, constant BCl_3 flow (60 sccm) was supplied to the gas phase during the CVD process. This results in an increased microhardness. Independent from the C:N ratio in the coating, the hardness values are about 300 HV higher in $TiB_xC_yN_z$ compared to the corresponding $TiC_{1-x}N_x$ coatings deposited at the same N_2:CH_4 ratio (appendix Table 16, p. 135). This is in good accordance with other reports on $TiB_xC_yN_z$ coatings (7).

To study $TiB_xC_yN_z$ coatings with different boron concentrations (C1-C5) a precursor ratio of N_2:CH_4 = 18 with different BCl_3 flow rates (0-240 sccm) was applied. Samples C1 and C3 therefore correspond to A1 and B1, respectively, but they will always be listed separately in this work for clarity. Comparison of the hardness values of $TiB_xC_yN_z$ coatings C1-C5 shows an increase from 2022 HV (C1) to 2514 HV (C5) with increasing BCl_3 flow rates.

WDS analysis

The compositions of $TiC_{1-x}N_x$ coatings A1-A5 and $TiB_xC_yN_z$ coatings B1-B5 and C1-C5 were evaluated by WDS analysis. The results are summarized in Table 1. The compositions are given in atomic percent, and additionally in the normalized form $TiC_{1-x}N_x$ with x=0-1 and $TiB_xC_yN_z$ with x+y+z=1.

Although the total amount of N+C+B is somewhat beyond 50 at.%, the relative deviation (see titanium) hardly exceeds 10%. Furthermore, small amounts of amorphous phases may affect the nominal $TiC_{1-x}N_x$ and $TiB_xC_yN_z$ film compositions to a minor extent.

In $TiC_{1-x}N_x$ coatings the variation of the N_2:CH_4 ratio between 18 and 0.25 results in an increase of the carbon concentration from 7.7 to 35.8 at.%, and respectively a decrease of the nitrogen concentration from 43.5 to 17.6 at.%. In addition, the titanium concentration slightly decreases by about 2 at %.

In $TiB_xC_yN_z$ coatings B1-B5 the additional supply of a constant BCl_3 flow (60 sccm) leads to an increased carbon concentration and slightly reduced nitrogen and titanium concentration compared to $TiC_{1-x}N_x$ films A1-A5 deposited at the same N_2:CH_4 precursor ratios. Furthermore, at this constant BCl_3 flow, the observed boron concentration is higher in nitrogen-rich than in carbon-rich $TiB_xC_yN_z$ coatings (0.6 – 3.7 at.% B).

Table 1: Chemical composition determined by WDS of $TiC_{1-x}N_x$ and $TiB_xC_yN_z$ coatings deposited at different BCl_3 flow rates and N_2:CH_4 precursor ratios.

Sample	N_2:CH_4	BCl_3 flow	Coating composition [at.%]				Normalized composition
		[sccm]	Ti	N	C	B	with Ti=1 and N+C+B=1
A1	18	0	48.8	43.5	7.7	-	$TiC_{0.15}N_{0.85}$
A2	9	0	48.9	41.6	9.5	-	$TiC_{0.18}N_{0.82}$
A3	3.5	0	48.1	41	10.9	-	$TiC_{0.21}N_{0.79}$
A4	1	0	47.8	32.5	19.7	-	$TiC_{0.38}N_{0.62}$
A5	0.25	0	46.6	17.6	35.8	-	$TiC_{0.67}N_{0.33}$
B1	18	60	44.5	41.9	10.8	2.9	$TiB_{0.06}C_{0.19}N_{0.75}$
B2	9	60	44.3	41.6	10.6	3.5	$TiB_{0.06}C_{0.2}N_{0.74}$
B3	3.5	60	41.8	36.8	17.6	3.7	$TiB_{0.06}C_{0.3}N_{0.64}$
B4	1	60	46	22.1	31.1	0.8	$TiB_{0.02}C_{0.57}N_{0.41}$
B5	0.25	60	44.7	16.5	38.1	0.6	$TiB_{0.01}C_{0.69}N_{0.3}$
C1[a]	18	0	48.8	43.5	7.7	-	$TiC_{0.15}N_{0.85}$
C2	18	30	45.9	46.1	7.1	0.9	$TiB_{0.02}C_{0.13}N_{0.85}$
C3[a]	18	60	44.5	41.9	10.8	2.9	$TiB_{0.06}C_{0.19}N_{0.75}$
C4	18	120	45.2	40.4	9.4	5.0	$TiB_{0.09}C_{0.17}N_{0.74}$
C5	18	240	44.5	38.4	10.1	6.9	$TiB_{0.13}C_{0.18}N_{0.69}$

[a] Samples C1 and C3 are the same samples as A1 and B1, respectively. Listed separately for clarity.

With increasing BCl_3 flow rate in the $TiB_xC_yN_z$ coatings C1-C5 the boron (0.9 - 6.9 at.% B), and interestingly also the carbon concentration in the coating increase, whereas the nitrogen concentration decreases.

XRD and SEM analysis

In Table 2 the lattice constants determined by XRD measurements (see Experimental part) of $TiC_{1-x}N_x$ (A1-A5) and $TiB_xC_yN_z$ (B1-B5, C1-C5) coatings are summarized.

Table 2: Lattice constants obtained from XRD of $TiC_{1-x}N_x$ and $TiB_xC_yN_z$ coatings deposited at different BCl_3 flow rates and N_2:CH_4 precursor ratios.

Sample	Lattice constant [nm]	Sample	Lattice constant [nm]	Sample	Lattice constant [nm]
A1	0.42503	B1	0.42551	C1[a]	0.42503
A2	0.42564	B2	0.42616	C2	0.42538
A3	0.42670	B3	0.42690	C3[a]	0.42551
A4	0.42778	B4	0.42827	C4	0.42576
A5	0.43210	B5	0.43080	C5	0.42616

[a] Samples C1 and C3 are the same samples as A1 and B1, respectively. Listed separately for clarity.

For the $TiC_{1-x}N_x$ coatings, the expected nearly linear shift to higher lattice constants with increasing carbon concentration in A1-A5 is observed.

As described in Chapter 2.3.2, XRD lattice parameter measurement can be used to estimate compositions of $TiC_{1-x}N_x$ coatings according to Vegard's law (81). Although this method is not very accurate (the titanium concentration is always hypothesized as 50 at %) and it allows only a coarse classification of the coatings in the normalized form $TiC_{1-x}N_x$ with the assumption Ti = 1 and N+C = 1, a good correlation to the results obtained by WDS was found (see Table 3). Thus, for the here studied $TiC_{1-x}N_x$ coatings XRD may additionally be used to determine the composition when looking at the C:N ratio only.

Table 3: Comparison of the chemical composition determined by WDS and XRD of HT-$TiC_{1-x}N_x$ coatings A1-A5.

Sample	WDS	XRD
A1	$TiC_{0.15}N_{0.85}$	$TiC_{0.16}N_{0.84}$
A2	$TiC_{0.18}N_{0.82}$	$TiC_{0.18}N_{0.82}$
A3	$TiC_{0.21}N_{0.79}$	$TiC_{0.25}N_{0.75}$
A4	$TiC_{0.38}N_{0.62}$	$TiC_{0.37}N_{0.63}$
A5	$TiC_{0.67}N_{0.33}$	$TiC_{0.69}N_{0.31}$

The XRD patterns of the $TiB_xC_yN_z$ coatings B1, B3 and B5 as well as of the references TiC and TiN are displayed in Fig. 13. Note that reflections of the TiN adhesive layer and the top Ti-B-N layer are also present in these patterns.

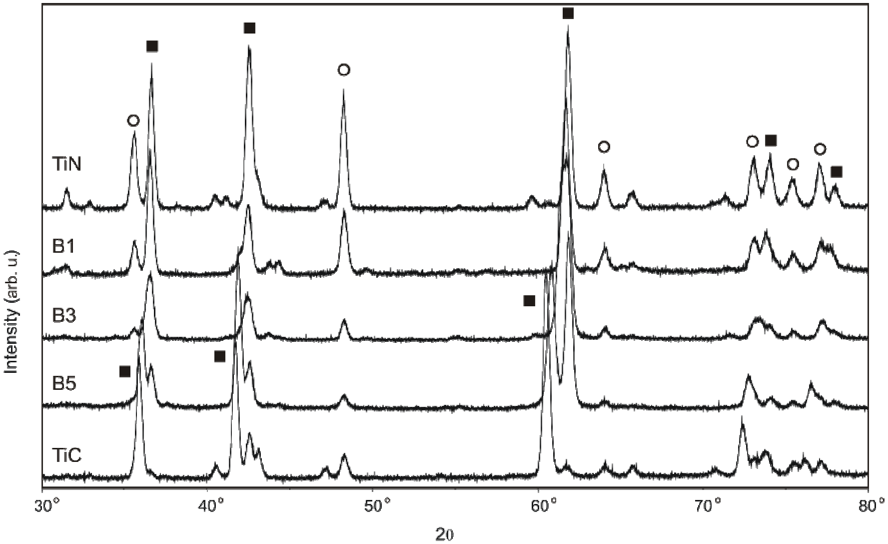

Fig. 13: XRD patterns of TiC, TiN and $TiB_xC_yN_z$ coatings B1, B3 and B5. ■ indicates the reflections of the cubic phase, ○ denotes WC, the substrate.

Analogous to the $TiC_{1-x}N_x$ coatings, the cubic $TiB_xC_yN_z$ reflections (■) shift from TiN toward the TiC positions with increasing C-concentration and the lattice constant show a very similar decrease (compare Table 2). In addition to this shift, a broadening of the reflections can be seen in the XRD patterns of $TiB_xC_yN_z$ coatings with increasing carbon concentration in B1-B5. The related reduction of the grain size was estimated by applying the Scherrer formula (83) (see Chapter 2.3.2), and it was found that the average grain size decreases by about 30% in B1-B3. The grain refinement of the $TiB_xC_yN_z$ coatings with increasing carbon concentration can also be seen in the SEM images in Fig. 14, showing the surface morphology of B1-B4.

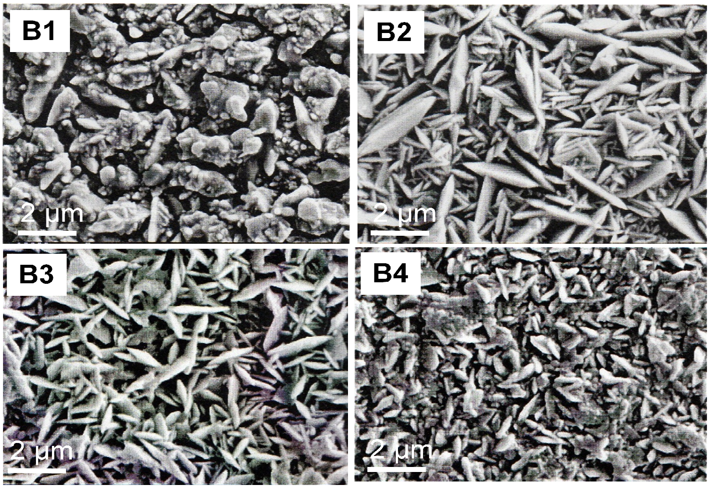

Fig. 14: SEM images (secondary-electron contrast, WD = 8 mm, EHT = 10 kV) showing the surface morphology of $TiB_xC_yN_z$ coatings B1-B4.

The XRD analysis of the $TiB_xC_yN_z$ coatings C1-C5 revealed that all coatings exhibit a cubic crystal structure (NaCl-type) independent from their boron concentration. Exemplary XRD patterns of the coatings C2 and C5 are provided in Fig. 15. The diffraction peaks of cubic $TiB_xC_yN_z$ are designated by ■ and those of WC, the substrate, by ○. Only traces of other compounds, likely h-BN and TiB_2, can be found at higher boron concentrations.

With increasing boron concentration (and decreasing nitrogen concentration) in C1-C5 a shift to lower 2Θ angles is observed. This indicates an increase of the lattice constants. The corresponding lattice constants are given in Table 2. Also included in Fig. 15 is an impression of the multilayer architecture of the coatings C2 and C5 provided by SEM images in the secondary-electron contrast mode. The TiN adhesive layer (bottom) exhibits a fine scale structure different from the polycrystalline $TiB_xC_yN_z$ layer (center) with a columnar microstructure. Furthermore, the Ti-B-N top layer shows much finer crystallites.

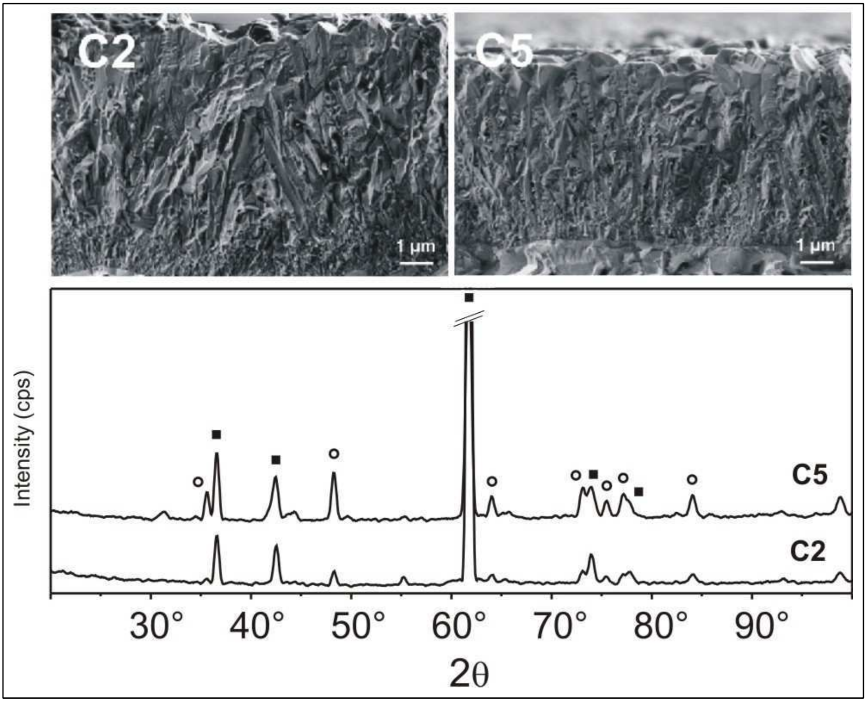

Fig. 15: SEM (secondary-electron contrast) images showing the fracture morphology of $TiB_xC_yN_z$ coatings C2 and C5 (WD = 3.2 mm, EHT = 2.5 kV) and XRD patterns of C2 and C5, ■ indicates the reflections of the cubic $TiB_xC_yN_z$, ○ denotes WC (substrate).

Additionally to the above described shifts, faint broadening of the reflections with an increasing amount of boron in the films can be detected in the XRD patterns of the

$TiB_xC_yN_z$ coatings C1-C5. The average grain size was estimated to decrease by about 20% from 84 nm (C2) to 69 nm (C5). This can also clearly be seen by the SEM images in Fig. 16, showing exemplarily the surface morphology of $TiB_xC_yN_z$ coatings C3 and C5.

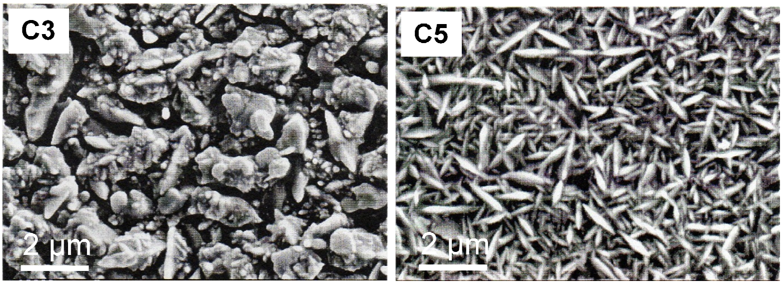

Fig. 16: SEM images (secondary-electron contrast, WD = 6 - 8 mm, EHT = 10 kV) showing the surface morphology of $TiB_xC_yN_z$ coatings C3 and C5.

Raman analysis

The Raman spectra of the coatings do not show significant D ("disorder", ~1355 cm^{-1}) and G ("graphitic" ~1555 cm^{-1}) bands, in this manner indicating the absence of amorphous carbon phases in all the cubic $TiC_{1-x}N_x$ and $TiB_xC_yN_z$ coatings. But characteristic modes of the coating materials due to defect-induced first-order Raman scattering as described in Chapter 2.3.1 are obtained in the range of 100-1000 cm^{-1}.

Fig. 17 exhibits the Raman spectra of the $TiC_{1-x}N_x$ (A1-A5, left) and $TiB_xC_yN_z$ coatings (B1-B5, right) with different C:N ratios. For comparison, the spectra of the TiC and TiN reference coatings are added at the bottom and top of the $TiC_{1-x}N_x$ series.

For TiN, four peaks at approximately 225 (TA), 315 (LA), 450 (2A) and 550 cm^{-1} (TO), and for TiC four peaks located at 280, 385, 585 and 675 cm^{-1} are identified in the Raman spectrum. All these Raman shifts are in good agreement with formerly published results (43; 44; 45; 46; 47; 48).

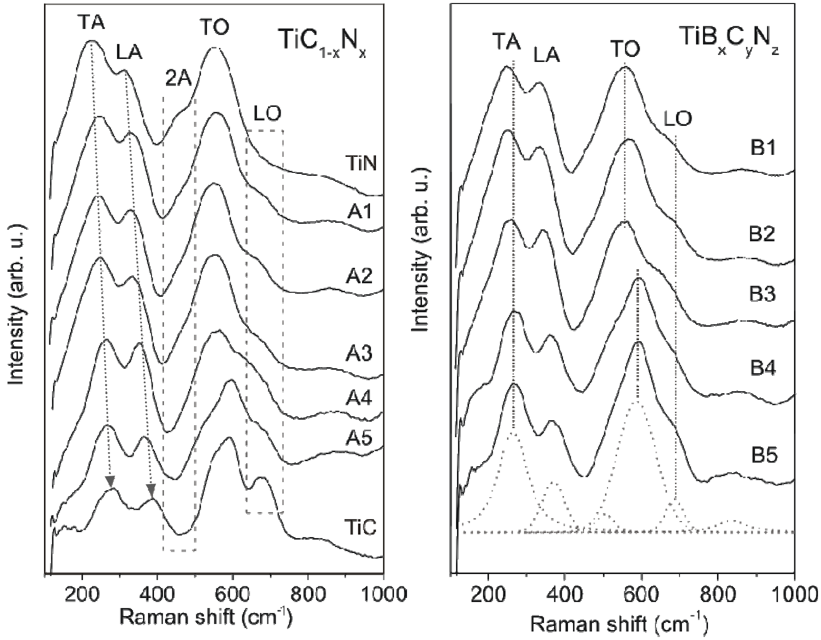

Fig. 17: Raman spectra (solid lines) of $TiC_{1-x}N_x$ coatings A1-A5 (left) and $TiB_xC_yN_z$ coatings B1-B5 (right) recorded in calottes including curve fittings for B5 as an example (dotted lines).

Since in the case of the $TiB_xC_yN_z$ coatings, the top Ti-B-N layer (9 at.% B) would show a sharp and intense peak at ~ 350 cm^{-1} (see Chapter 4.2.5), which cannot be observed here, the results confirm that only the $TiB_xC_yN_z$ sublayer is sampled with the used set-up. The Raman spectra of the coatings displayed in Fig. 17 exhibit significant changes regarding the positions of the peaks and also their relative intensities. Positions, heights, areas as well as FWHMs of the individual Raman peaks were obtained as described in the Experimental part and an exemplary fit of the signals of sample B5 is included in Fig.17 (dotted lines). Fig. 18 visualizes the derived wavenumbers for the TA, LA, TO and LO modes of $TiC_{1-x}N_x$ coatings (A1-A5) and $TiB_xC_yN_z$ coatings (B1-B5) and a summary of all values is given in Table 4.

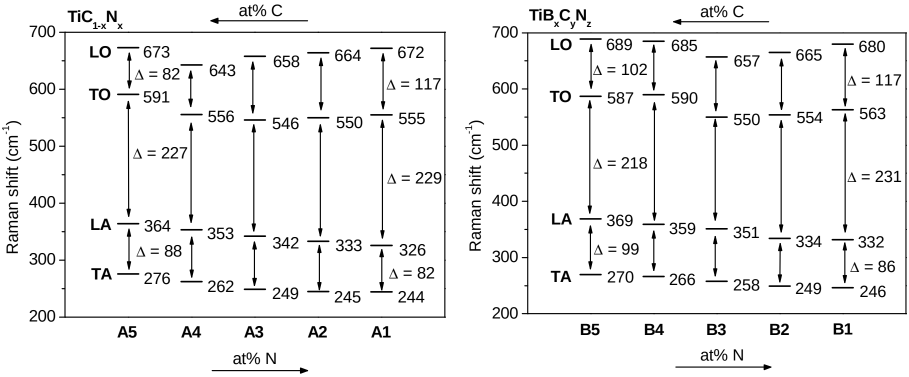

Fig. 18: Raman peak positions of the TA, LA, TO and LO modes of $TiC_{1-x}N_x$ coatings A1-A5 (left) and $TiB_xC_yN_z$ coatings B1-B5 (right).

The optical phonons are known to be primarily dominated by the vibrations of the lighter ions (43; 44; 45; 46; 47; 48), thus at first glance a variation of the C:N and B concentration is expected to contribute to the optical rather than the acoustical modes. However, in the here studied coatings, the Raman peaks in the acoustical range appear to shift in a nearly linear manner to lower wavenumbers (by about 30 cm^{-1}) with increasing nitrogen concentration in A5-A1 and B5-B1 (see Fig. 18), whereas in the optical range an apparent transition in the spectral shape of the Raman bands from C-rich to N-rich coatings can be observed. In rather carbon-rich (> 30 at.% C) coatings like A5, B4 and B5 the most intense peak in the optical range is located close to 590 cm^{-1}, which correlates well with the TO mode of TiC (48). The nitrogen-rich (> 30 at.% N) coatings A1-A4 and B1-B3 show a maximum peak intensity at approximately 560 cm^{-1}, resulting from the TO mode of TiN (35).

Table 4: Raman peak positions as determined from the investigated $TiC_{1-x}N_x$ (A1-A5) and $TiB_xC_yN_z$ (B1-B5) samples.

Sample	Raman peak position (cm^{-1})			
	TA	LA	TO	LO
A1	244	326	555	672
A2	245	333	550	664
A3	249	342	546	658
A4	262	353	556	643
A5	276	364	591	673
B1	247	331	559	671
B2	249	334	554	665
B3	258	351	550	657
B4	266	359	590	685
B5	270	369	587	689

Besides the shift of the peaks, also intensity changes are observed. The peak shoulder at ~ 450 cm^{-1} (see Fig. 17), which can be attributed to the second-order acoustical (2A) phonon of TiN (35) slowly disappears with increasing carbon concentration in A1-A5. In the same way the peak at 675 cm^{-1}, assigned to the LO mode of TiC (48), becomes more pronounced (see Fig. 17). Thus, a well-defined change in the spectral shape of the Raman bands is seen when the nitrogen or carbon concentration in the coatings exceeds at least 30 at.%. The evident changes of the complex spectral shape in the optical region between the C-rich and N-rich coatings suggest that the appearance of this region may serve as a fingerprint to discriminate between C- and N-rich coatings.

As an example, coatings B4 and A4, which were both deposited using the same N_2:CH_4 precursor ratio, can be clearly distinguished by their Raman spectra (see B4 and A4 in Figs. 17 and 18) due to the higher carbon concentration in $TiB_xC_yN_z$ coating B4 (31.1 at % C) compared to $TiC_{1-x}N_x$ coating A4 (19.7 at % C). The spectrum of A4 still resembles TiN with a TO peak maximum at ~560 cm^{-1}. In the case of sample B4, where more carbon than nitrogen is incorporated, the spectrum is already dominated by TiC with a maximum intensity at ~590 cm^{-1}.

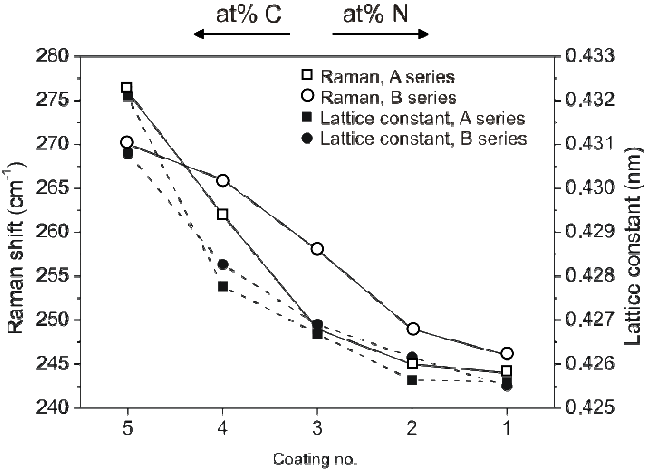

Fig. 19: Lattice constants (broken lines) and Raman peak positions of the TA mode (solid lines) of $TiB_xC_yN_z$ coatings B1-B5 (● and ○) and $TiC_{1-x}N_x$ coatings A1-A5 (■ and □).

On the other hand, the acoustical region may be reasonably well described by two overlapping peak structures, which gradually change with coating composition. Therefore, the TA (or LA) peaks are much better suited to characterize coatings by their Raman shifts than the TO (or LO) peaks. In Fig. 19, the peak shifts of the TA mode (solid lines) of coatings A5-A1 (□) and B5-B1 (○) are compared to the lattice constants (broken lines) of the coatings as determined by XRD. Obviously, the trends of Raman and XRD data correlate very well for the investigated coatings. It is worth noting that with decreasing lattice constant a shift to lower Raman wavenumbers is observed.

However, differences between C-rich and N-rich coatings may not only characterized by Raman peak positions, but also peak heights, areas and FWHM. These values exhibit significant changes in dependence on the coating composition. A subset of corresponding data is presented in Table 5. The TA mode is used to exemplarily demonstrate effects for the $TiC_{1-x}N_x$ coatings A1-A5 as well as $TiB_xC_yN_z$ coatings B1-B5. Generally, the main factors responsible for changes of Raman spectra at a given temperature are the chemical composition, grain size and defects in the sample (46). Composition changes in mixed crystals are assumed to primarily affect the peak positions due to changes in the lattice constant. The FWHM is expected to be correlated to the grain size. The total intensity of the Raman peaks of the cubic crystals is determined by defects (see Chapter 2.3.1), thus a higher defect concentration in the coating is supposed to lead to higher total peak intensity (35; 42; 43; 44; 45; 46; 47).

Table 5: Raman peak positions, intensities (peak height), FWHM and peak areas of the TA mode of the coatings A1-A5 and B1-B5.

Sample	mode	Peak Position (cm^{-1})	Normalized peak height	FWHM (cm^{-1})	Peak Areas (arb. u.)
A1	TA	244	0.56	86	33.79
A2		245	0.55	89	34.02
A3		249	0.54	105	43.61
A4		262	0.41	70	19.85
A5		276	0.39	58	15.73
B1	TA	247	0.54	96	37.58
B2		249	0.55	88	33.39
B3		258	0.53	99	39.11
B4		266	0.32	60	13.47
B5		270	0.36	61	15.35

The TA modes of the measured A- and B-samples (see Table 5) exhibit roughly similar heights, areas and FWHMs for CVD coatings deposited at the same N_2:CH_4 precursor ratios. Tentatively, the related quantities tend to increase with higher N-concentrations in the coatings. A significant drop to higher values is observed between A4-A5 and A1-A3, as well as B4-B5 and B1-B3, most likely accompanying the transition from nitrogen- to carbon-rich coatings.

Fig. 20 (right side) presents the Raman spectra of the $TiB_xC_yN_z$ coatings C1-C5. Again, the dotted lines at the bottom give an example for the separation into components by curve fittings. Interestingly, with increasing boron concentration in the $TiB_xC_yN_z$ coatings the overall spectral shape of the Raman bands does not change significantly. However, the peak positions of the different modes in the acoustical and optical range slightly shift to higher wavenumbers (about 10 cm^{-1}) with increasing boron concentration in C1-C5 (see Fig. 20, left).

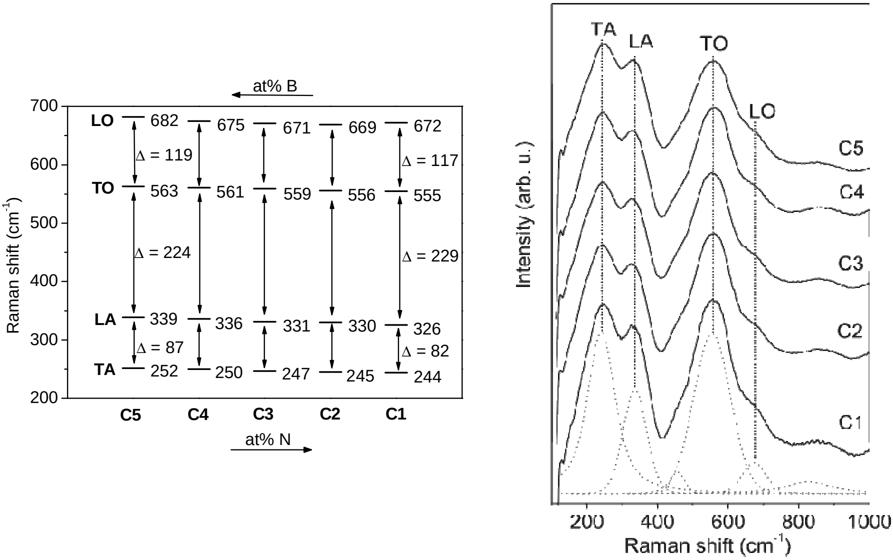

Fig. 20: left side - Raman peak positions of $TiB_xC_yN_z$ coatings (C1-C5); right side - Raman spectra (solid lines) of $TiB_xC_yN_z$ coatings C1-C5 with different boron-concentrations recorded in calottes including curve fittings for C1 as an example (dotted lines).

In Table 6 the derived wavenumbers of the Raman peaks are summarized. As indicated by the atomic concentrations from WDS measurements (see Table 1) increasing boron incorporation affects the C:N ratio in the coating by reducing the nitrogen concentration. As described above, increasing nitrogen concentration is found to cause a shift of the TA and LA modes to lower wavenumbers. The same trend can be found in the Raman spectra of C5-C1.

Table 6: Raman peak positions as determined from the investigated $TiB_xC_yN_z$ samples C1-C5.

Sample	Raman peak position (cm^{-1})			
	TA	LA	TO	LO
C1[a]	244	326	555	672
C2	245	330	556	669
C3[a]	247	331	559	671
C4	250	336	561	675
C5	252	339	563	682

[a] Samples C1 and C3 are the same samples as A1 and B1, respectively. Listed separately for clarity.

Comparison of the TA peak positions (Fig. 21; △, solid line) with the lattice constants (Fig. 21; ★, broken line) of coatings C2-C5 again demonstrates a good correlation between the Raman and XRD data.

Obviously, an increase in the lattice constant results in a shift of the peaks to higher frequencies. The increase of the lattice constant with higher boron concentrations may be an effect of the larger atomic radius of boron (0.098 nm) compared to nitrogen (0.071 nm). Furthermore, an excess of boron may exist in a form of interstitial atoms. This may also result in higher lattice constants. On the other hand, the frequency changes may in addition be related to mass changes (B=10.81 g/mol, N=14.01 g/mol). (46)

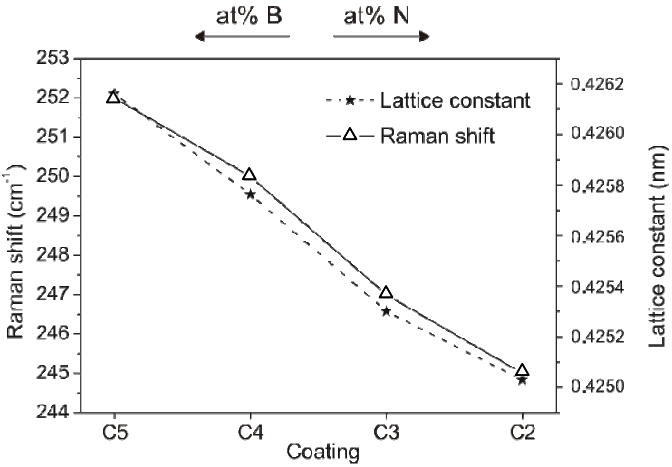

Fig. 21: Lattice constants (★ broken line) and Raman peak positions of the TA mode (△ solid line) of $TiB_xC_yN_z$ coatings C2-C5.

By increasing the boron concentration in $TiB_xC_yN_z$ coatings C1-C5, XRD and SEM measurements indicate grain refinement takes place. This should correspond to an increase of the FWHM in the Raman spectra of C1-C5.

However, the modes in the acoustical range do not show significant changes in their peak intensity, area or FWHM. The TO mode, on the other hand, exhibits a slight increase of the FWHM from C1-C5, most likely correlated to the grain refinement found by XRD and SEM. In Table 7 the observed FWHMs, peak intensities and areas of the prominent TO mode of coatings C1-C5 are summarized. In contrast to the FWHM of the Raman peaks, the intensities and areas remain nearly constant with increasing boron concentration. Therefore, it can be assumed that the lattice-defect concentration does not change considerably with higher boron concentrations in the coatings.

Table 7: Raman peak positions, intensities (peak height), FWHM and peak areas of the TO mode of the coatings C1-C5.

Sample	mode	Peak Position (cm^{-1})	Normalized peak height	FWHM (cm^{-1})	Peak Areas (arb. u.)
C1[a]	TO	555	0.61	96	43.02
C2		556	0.61	98	43.25
C3[a]		559	0.62	102	44.65
C4		561	0.60	103	43.21
C5		563	0.56	107	42.41

Correlation of Raman results with WDS and XRD

In order to shed light on the general trends of the structural coating properties, Raman data of all examined $TiC_{1-x}N_x$ and $TiB_xC_yN_z$ coatings are compared to the composition and lattice constants as independently derived from WDS and XRD measurements. The focus was set on the wavenumbers determined for the TA Raman peaks. The dependence of the TA Raman shifts on the composition and lattice constant is presented in Fig. 22. All subsets of data as well as the binary reference compounds TiC and TiN have been included in the figures, and the data of the subsets have been characterized by different symbols. The composition is characterized by the carbon concentration only. Despite of minor scattering, the measured Raman shifts change rather systematically with either carbon concentration or lattice constant, quite similar to the well-known one-mode behavior of the optical phonons in pseudobinary mixed-crystal alloys (116). Here, the dependencies may be described by a nearly linear behavior in case of the N-rich coatings, but the variation of Raman shifts of the C-rich coatings is much reduced in comparison to the N-rich region of the figures. Lines of the functional form [$a + b\cdot x + c\cdot x\cdot(1-x)$, with $x = 0\ldots1$, e.g. relative carbon concentration] have been drawn in both figures to match the

TiC$_x$N$_{1-x}$ data (A-coatings) closely. Similar deviations from Vegard's law have frequently been reported, especially for semiconductor alloys, where c is typically called the 'bowing parameter' (117; 118).

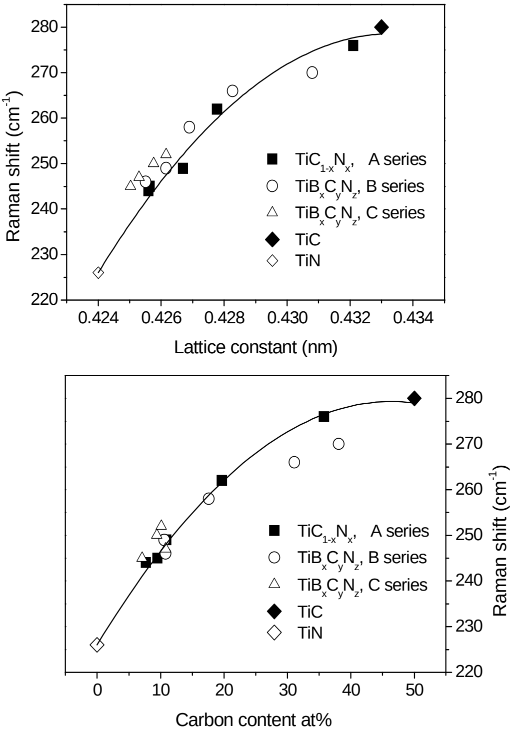

Fig. 22: Raman shifts of the TA modes of TiB$_x$C$_y$N$_z$ (B- and C-series) and TiC$_{1-x}$N$_x$ (A-series) in dependence of lattice constant (top) and coating composition (bottom).

Interestingly even the data of quaternary coatings (B- and C-coatings) fall close to these lines. The apparent deviation from a linear behavior of the Raman shifts seems to be somewhat larger in case of the dependence on carbon concentration. This may be explained by a slightly higher uncertainty in the composition compared to the lattice constants, especially for the boron-containing coatings (see Chapter 3.4.3). Nevertheless, these results clearly demonstrate the close correlation of Raman shifts to the structural coating properties, even for the more complex $TiB_xC_yN_z$ coatings. Thus, Raman spectroscopy may be used to estimate local lattice constants for such coatings. In the case of $TiC_{1-x}N_x$, also the composition may be derived locally, and even for $TiB_xC_yN_z$ coatings concentrations of the major C and N components may be estimated. Due to the high spatial resolution, these information may be provided locally by using Raman micro-spectroscopy as is demonstrated here.

4.1.2 Moderate-temperature CVD coatings (a- and c-series)

MT- $TiC_{1-x}N_x$ coatings (a-series)

In addition to HT-$TiC_{1-x}N_x$ coatings, moderate-temperature (MT-)$TiC_{1-x}N_x$ coatings were investigated in this work by Raman spectroscopy. The results are compared to those of the HTCVD coatings. MT-$TiC_{1-x}N_x$ coatings hereby refer to all coatings using the precursor acetonitrile (CH_3CN), although the actual coating temperatures were varied from 850 to 1000°C.

The composition of the MT- $TiC_{1-x}N_x$ coatings can be compared with the values reported by Bonetti et al. (13). The overall reaction at 850°C is assumed to be (12):

$$6TiCl_4 + 2\ CH_3CN + 9\ H_2 \rightarrow 6\ TiC_{0.63}N_{0.37} + 24\ HCl$$

From this equation, it is suggested that the composition of MTCVD coatings is directly proportional to the C:N ratio in the precursor CH_3CN. Therefore, in contrast to HTCVD coatings, it is not possible to vary the composition of MT- $TiC_{1-x}N_x$ in a wide range.

Fig. 23 shows SEM images of MT-$TiC_{1-x}N_x$ coatings deposited at 850°C and 1000°C (5; 6). It was found, that the microstructure in MT- $TiC_{1-x}N_x$ coatings is columnar when prepared at temperatures between 850-1000°C. The average column width grows from 0.4 µm at 850°C to 0.6 µm at 1000°C when keeping the concentration of the precursors constant, while coating deposition rates changes from 1.5 to 2.5 µm/h. On the other hand, no influence on microhardness (2400 ± 100 HV, see appendix Table 16, p. 135) and scratch adhesion is observed. (5; 6)

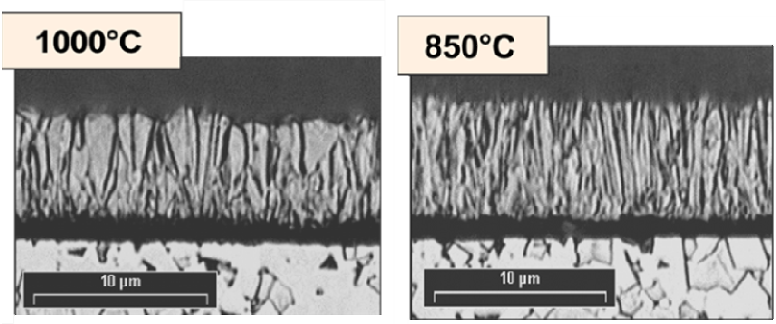

Fig. 23: SEM images showing the microstructure of MT-$TiC_{1-x}N_x$ coatings deposited at 850°C and 1000°C (5; 6).

The compositions of the here studied MT- $TiC_{1-x}N_x$ coatings deposited at temperatures between 850-1000°C (in the following labeled a1-a4) were estimated by XRD lattice parameter measurements. To recheck the results, the compositions of three of the MTCVD coatings (a1, a3 and a4) were further determined by WDS (Table 8). Again, both methods show very good agreement for the examined coatings.

Table 8: Comparison of the chemical composition determined by WDS and XRD of MT-$TiC_{1-x}N_x$ coatings.

Sample	Temperatur	WDS	XRD
a1	850°C	$TiC_{0.57}N_{0.43}$	$TiC_{0.57}N_{0.43}$
a2	900°C	-	$TiC_{0.54}N_{0.46}$
a3	950°C	$TiC_{0.51}N_{0.49}$	$TiC_{0.51}N_{0.49}$
a4	1000°C	$TiC_{0.47}N_{0.52}$	$TiC_{0.48}N_{0.51}$

The carbon concentration, at a deposition temperature of 850°C, was found to be quite similar to those reported by Bonetti et al. (13). However, with increasing temperature, the nitrogen concentration of MT-$TiC_{1-x}N_x$ coatings slightly increases from $x = 0.43$ for a1 to 0.52 for a4. Thus, the C:N ratio is to some extent dependent on the deposition temperature.

Fig. 24 exhibits the Raman spectra of MT-$TiC_{1-x}N_x$ coatings a1-a4. Spectra of all coatings show peaks located at approximately 275, 365, 550 and 620 cm^{-1}. No significant changes of the peak positions in the acoustical range are obtained, in contrast to the results of HT-$TiC_{1-x}N_x$ coatings. However, the quite small composition changes from a1 to a4 seem to be visible in the different intensities of the optical modes located at 550 and 620 cm^{-1}. With higher deposition temperatures, the nitrogen concentration slightly increases, and the peak at 550 cm^{-1} becomes more pronounced. In addition the peak at ~ 620 cm^{-1} shifts slightly to higher wavenumbers (from 610 for a1 to 620 cm^{-1} for a4).

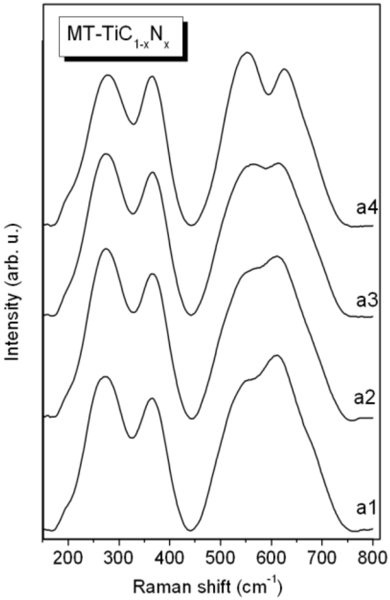

Fig. 24: Raman spectra of MT- TiC$_{1-x}$N$_x$ coatings a1-a4 deposited at temperatures of 850, 900, 950 and 1000°C, respectively.

Furthermore, direct comparison of the MT-TiC$_{1-x}$N$_x$ coating a4 (deposited at a similar temperature as used in HTCVD processes) with the HT-TiC$_{1-x}$N$_x$ coatings reveals that a4 fits very well into the above described regularities of TiC$_{1-x}$N$_x$ with varying C:N concentration (shift in wavenumbers and intensity changes). In Fig. 25 (left side) the Raman spectra of different HT-TiC$_{1-x}$N$_x$ coatings (A1, A2 and A4) and the MT-TiC$_{1-x}$N$_x$ coating a4 are compared with TiN. The corresponding wavenumbers are also given in Fig. 25 (right side). In the acoustical range, the expected shift to lower wavenumbers is obtained (30 - 40 cm^{-1}) by increasing the N-concentration from MT-TiC$_{0.47}$N$_{0.52}$ (a4) over A4, A2 and A1 to TiN, whereas the optical modes shift toward higher values (~ 50 cm^{-1} in the case of the LO mode). In addition, intensity changes can be clearly observed (Fig. 25, dashed-boxes). With increasing nitrogen concentration, the intensity of the LO mode of TiC gradually decreases, whereas that of the 2A mode of TiN increases.

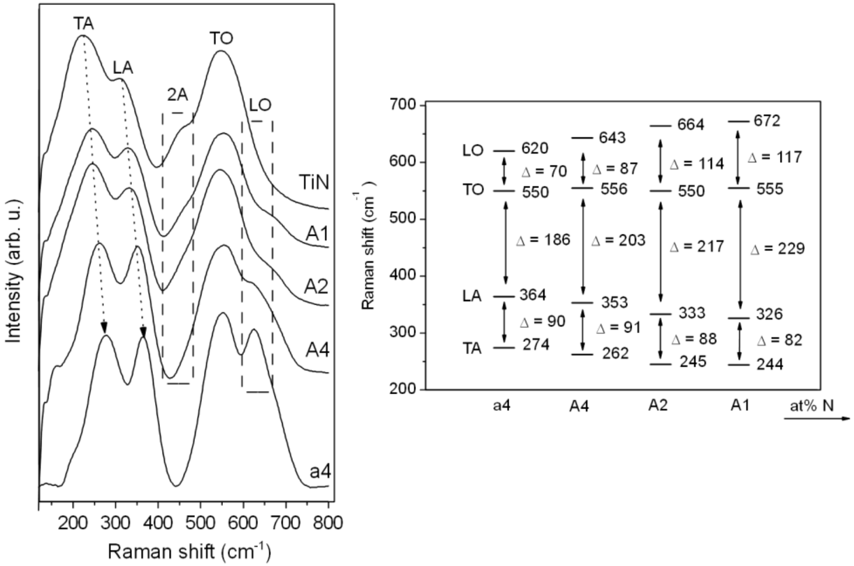

Fig. 25: Comparison of the Raman spectra (left side) and Raman peak positions (right side) of TiN with HT- and MT-$TiC_{1-x}N_x$ coatings A1, A2, A4 and a4.

MT- $TiB_xC_yN_z$ coatings (d-series)

Cubic MT-$TiB_xC_yN_z$ coatings can be deposited under similar conditions as used for MT-$TiC_{1-x}N_x$ by the addition of BCl_3 to the gas phase during the CVD process (5; 6). The BCl_3 flow rate was therefore varied between 20 - 240 sccm comparable to the C-series HTCVD coatings. Thus, the MT-$TiB_xC_yN_z$ coatings will hereafter be labeled as c1–c5. Further deposition details can be found in the appendix (Table 16, p. 135).

It should be mentioned, that the compositions of the here studied MT- $TiB_xC_yN_z$ coatings was not determined by WDS measurements, but results of former analysis are given in (5; 6).

The SEM images of the MT-$TiB_xC_yN_z$ coatings (Fig. 26) show grain refinement by increasing the BCl_3 flow rate in c1-c5, but the Raman spectra (Fig. 27) do not exhibit significant changes in the spectral shape of the individual Raman bands. These results are in good agreement with the HT-$TiB_xC_yN_z$ coatings C1-C5.

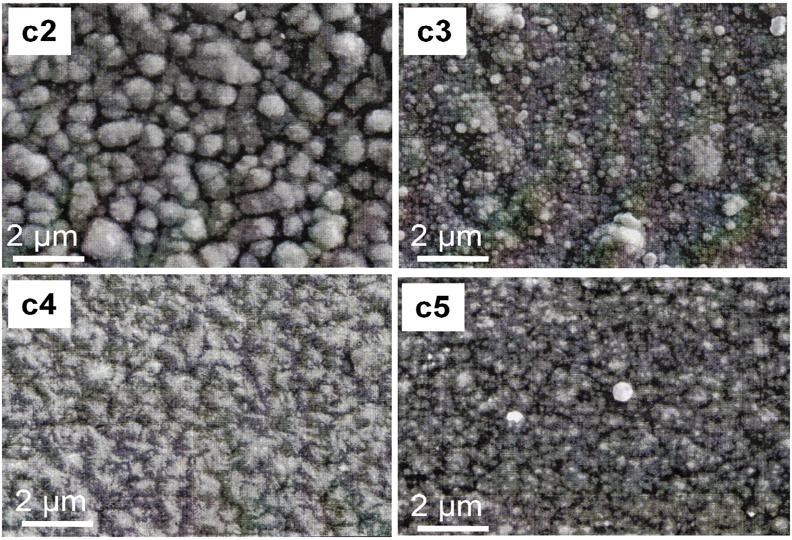

Fig. 26: SEM images (secondary-electron contrast, WD = 7 - 10 mm, EHT = 10 kV) showing the surface morphology of MT-$TiB_xC_yN_z$ coatings c2-c5.

Although no considerable changes of the peak positions are obtained, the intensities of the Raman bands in the optical range vary systematically. This observation seems similar to the MT-$TiC_{1-x}N_x$ coatings a1-a4, where an increase of the TO mode intensity was observed with an increasing nitrogen concentration. With regard to the WDS results of HT- $TiB_xC_yN_z$ coatings, it can be assumed that boron addition decreases the N-concentration and increase the C-concentration. Thus, compared to a4 (shown at the bottom of Fig. 27) the relative intensity of the TO mode at ~ 550 cm^{-1} should abate with higher BCl_3 flow rates, whereas the intensity of the LO mode at ~620 cm^{-1} should increase. Indeed, this can clearly be seen in Fig. 27.

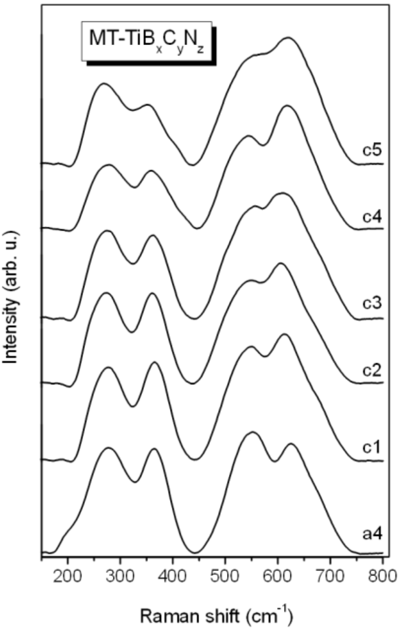

Fig. 27: Raman spectra of MT- TiB$_x$C$_y$N$_z$ coatings deposited at different BCl$_3$ flow rates.

In conclusion, for the MTCVD coatings, the rather small variation in the C:N and B concentration seems to contribute to the optical rather than the acoustical modes. This is in contrast to the results obtained for HTCVD coatings, but in good agreement with results of other authors (35; 42; 43; 44; 45; 46; 47; 48).

4.1.3 Summary

$TiC_{1-x}N_x$ and $TiB_xC_yN_z$ coatings have been prepared applying HT- and MT-LPCVD and characterized using Raman spectroscopy, WDS, XRD and SEM. It was shown that first-order, defect-induced Raman spectra of good quality can be obtained from the coatings, even if buried within a multilayer stack like the $TiB_xC_yN_z$ coatings.

Even small changes in the C:N ratio result in systematical shifts of the Raman peaks. With increasing nitrogen concentration, the acoustical phonons shift to lower frequencies (30 - 40 cm^{-1}). In the optical range, on the other hand, a well-defined change in the spectral shape of the Raman bands is obtained when the nitrogen or carbon concentration in the coatings exceeds at least 30 at.%. Direct comparison of the MTCVD coatings with the HTCVD coatings reveals that they fit very well into these regularities.

Furthermore, a high correlation of the Raman shifts with the lattice constants derived from XRD measurements has been found. Both methods show the same transition trends for the examined coatings. Additionally to the peak positions, intensity and FWHM of the Raman bands change during the transformation from carbon- to nitrogen rich coatings.

The sensitivity of the TA-mode shifts to changes in the structural properties of the investigated coatings (composition and lattice constants) was found to be largest for N-rich coatings. Looking at the full range of coatings ($TiC_{1-x}N_x$ and $TiB_xC_yN_z$) the dependence of the Raman shifts is slightly nonlinear.

In conclusion, for coatings deposited in the $TiC_{1-x}N_x$ and $TiB_xC_yN_z$ system, Raman spectroscopy may be used to estimate locally compositions and lattice constants due to the high spatial resolution as is demonstrated here.

4.2 Ti-B-N coatings (D-series)

In this chapter, coatings deposited by MTCVD in the Ti-B-N system will be discussed. The influence of different boron concentrations (9.6 - 55.4 at %) on the coating composition is studied by means of WDS, XRD, SEM, XPS and Raman spectroscopy.

XRD, SEM, WDS and XPS are commonly used techniques for the analysis of such coatings. However, Raman spectroscopy has not before been used for this coating system.

The findings of the different analysis methods will be correlated with regard to their varying information depths (e.g. XPS $\leq$ 10 nm, XRD $\geq$ 10 µm) and information contents (crystallographic structure, chemical composition…) for the characterization of the different phases in Ti-B-N coatings with varying boron concentrations (hereafter labeled as D-series).

4.2.1 Deposition and microhardness

Coatings in the Ti-B-N system with increasing boron concentrations were deposited by systematically varying the BCl_3 flow rate (30 - 480 sccm; D1-D5) during the CVD process (850°C, 900 mbar) at a constant $TiCl_4$:N_2 ratio ($TiCl_4$= 2 ml/min, N_2= 6 l_N/min). The hardness values were found to constantly increase from 3490 HV for D1 to the very high value of 4360 HV for D5.

4.2.2 WDS analysis

The compositions of the Ti-B-N coatings were evaluated by WDS analysis. The results are given in Table 9. An increasing BCl_3 flow rate from 30 to 480 sccm during the CVD process leads to an increased boron concentration in the coatings from 9.6 - 55.4 at.%, whereas the nitrogen and titanium concentrations decrease.

Table 9: Chemical composition of Ti-B-N coatings deposited at different BCl_3 flow rates determined by WDS.

Sample	BCl_3 flow [sccm]	Coating composition [at.%] Ti	N	B
D1	30	46.7	43.7	9.6
D2	60	44.7	37.1	18.2
D3	120	40.1	24.4	35.5
D4	240	37.6	20.1	42.3
D5	480	33.3	11.3	55.4

Fig. 28 presents the positions of coatings D1-D5 within the simplified ternary Ti-B-N phase diagram according to Ref. (19; 21). As described in Chapter 2.2.4, the Ti-B-N system comprises several elementary regions and binary phases, but no ternary phase exists.

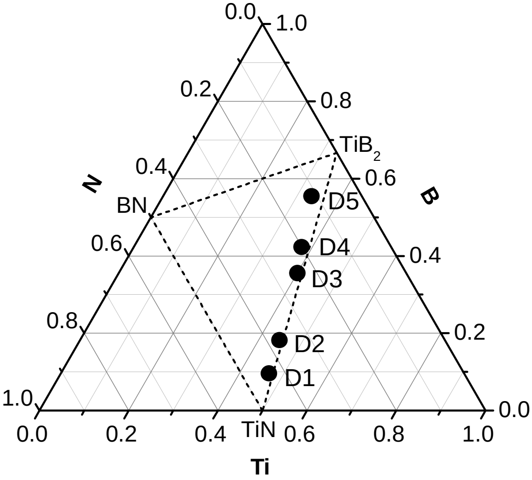

Fig. 28: Positions of coatings D1-D5 in the phase diagram of Ti-B-N as determined by WDS.

The coatings D1-D5 can be found in the section TiB_2+TiN+BN, very close to the quasi-binary tie-line of TiN and TiB_2. The positions of coatings D1-D5 in the phase diagram suggest a nearly pure two-phase structure.

4.2.3 XRD and SEM analysis

The crystallographic structures of the Ti-B-N coatings were examined by XRD. Fig. 29 shows characteristic reflections of the XRD patterns of D1-D5 compared to the references TiN (bottom) and TiB_2 (top) coatings. The diffraction peaks of cubic TiN are designated by ●, those of hexagonal TiB_2 by ■, and those of WC, the substrate, by □.

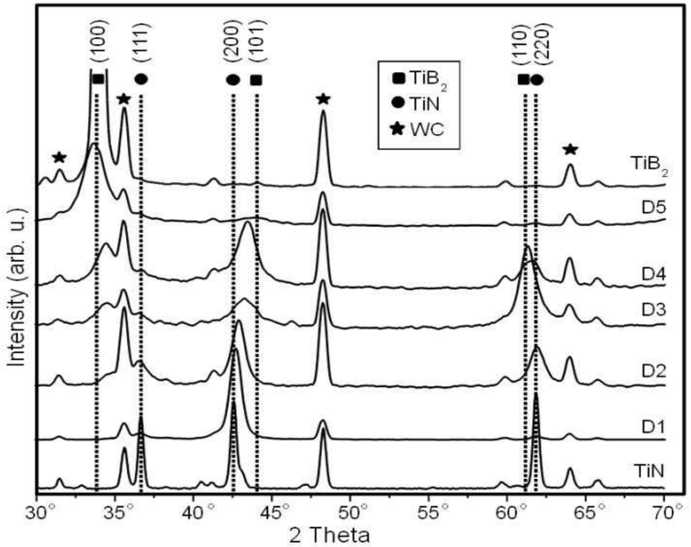

Fig. 29: XRD patterns of TiN, TiB_2 and Ti-B-N coatings D1-D5. ■ indicates the reflections of the hexagonal phase, ● reflections of the cubic phase, and ★ denotes WC.

For the TiB_2 coating, a pronounced (001) texture was found by an intense diffraction peak at 2θ = 33.94°. The TiN coating exhibits three characteristic reflections located at 2θ = 36.6, 42.7 and 61.8°, that are assignable to the (111), (200) and (220) reflections, respectively, of the cubic TiN structure. With incorporation of B into the coatings, different transition trends in the XRD patterns (peak positions, intensity and FWHM) appear, which will be discussed in the following sections.

It is evident that the addition of 9.6 at.% boron (A1) to TiN leads to a decrease in the (111) and (220) reflections intensity, whereas the (200) diffraction peak broadens and shifts toward higher 2θ angles.

At a boron concentration of 18.2 at.% (D2), a weak shoulder located at 2θ = 34.55° appears, which may be attributed to the (100) reflection of TiB_2. This reflection becomes more intense with increasing boron concentrations in coatings D2-D5 and shifts to lower 2θ angles (correlating to a higher lattice constant) toward the peak position of the TiB_2 reference coating (2θ = 33.94°).

In addition to the intensity of the (100) reflection of TiB_2 in D2-D5 increasing, the (111) reflection of TiN gradually decreases. Furthermore, with increasing boron concentrations in the Ti-B-N coatings, the (200) and (220) reflections of TiN broaden and shift toward the positions of the (101) and (110) reflections of TiB_2, respectively. This can also be seen in Table 10, where the cubic and hexagonal lattice constants *a* and the corresponding FWHMs of the coatings are given, determined from the cubic (200) reflection and the hexagonal (100) reflection.

According to Vegard`s law (81) the formation of a continuous solid solution between TiB_2 and TiN is impossible, because TiB_2 crystallizes in a hexagonal lattice, and TiN forms the well-known cubic structure. Nevertheless, the obtained shifts of the TiN reflections toward TiB_2 positions in D1 to D5 are in agreement with the results of other studies (21; 22; 119). They attributed a supersaturated cubic $TiN_{1-x}B_y$ phase to the coatings deposited with low boron concentrations (D1-D2, $B \leq 18$ at %), whereas higher boron concentrations ($B \geq 18$ at %) in the Ti-B-N coatings resulted in the coexistence of a hexagonal TiB_2 and a cubic TiN phase. This phase behavior was observed in the XRD spectra of D2-D4. The coatings with even higher boron concentrations (D5) may be interpreted as a single-hexagonal $TiB_{2-x}N_y$ phase in which nitrogen substitutes boron in the hexagonal TiB_2 framework (22).

Table 10: Cubic and hexagonal lattice constants *a* and the corresponding FWHM of Ti-B-N coatings D1-D5 as determined by XRD.

Sample	Lattice constant *a* from cubic (200) [nm]	FWHM of (200) [°]	Lattice constant *a* from hexagonal (100) [nm]	FWHM of (100) [°]
TiN	0.42466	0.41	-	-
D1	0.42310	0.83	-	-
D2	0.42140	0.93	0.29951	0.91
D3	0.41638	1.51	0.29968	1.72
D4	0.41648	1.51	0.30074	1.35
D5	0.41194	3.45	0.30671	1.75
TiB_2	-	-	0.30474	0.51

Other than those of TiN and TiB_2, no significant reflections of other phases, such as BN, boron or TiB were observed in the XRD patterns of D1-D5, in accordance with the Ti-B-N phase diagram (Fig. 29).

The increased broadening of the diffraction peaks with increasing boron concentration in the Ti-B-N coatings can be attributed to a decreasing grain size. An estimation of the grain size according to the Scherrer equation (83) indicates a nanocrystalline phase for all of the Ti-B-N coatings. Furthermore, the grain size of the nanocrystallites decreases with increasing boron concentration. This assumption is supported by the SEM images in Fig. 30, which show the multilayer architecture of coatings D1, D2, D4 and D5. The TiN adhesive layer (bottom) exhibits a columnar microstructure with coarse grains that are different from those of the polycrystalline Ti-B-N layer (top). For D1, the addition of small amounts of boron results in Ti-B-N coatings with interrupted TiN columns. A further increase of the boron concentration in D1-D5 decreases the grain size to a larger extent and leads to a fine-crystalline structure (coatings D4 and D5). This is in good agreement with other reports on Ti-B-N (20; 120).

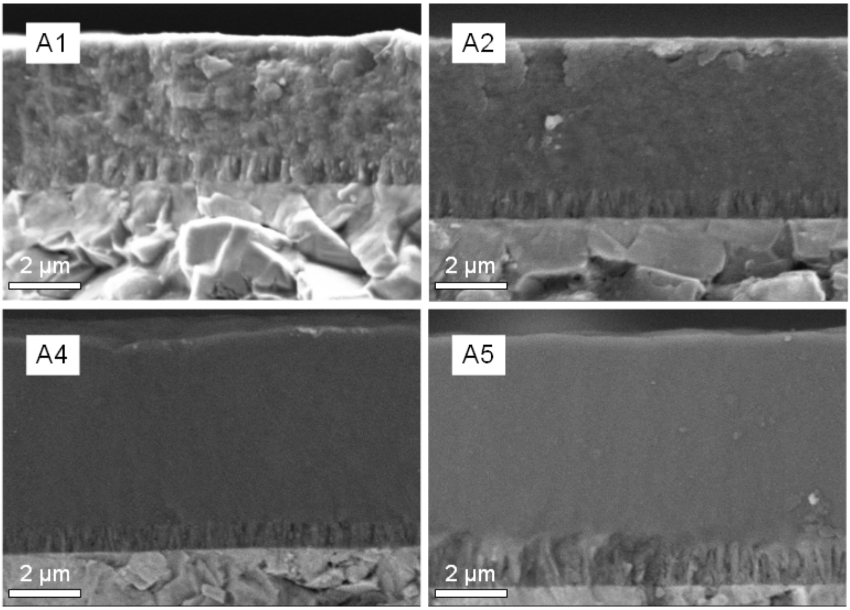

Fig. 30: SEM images (secondary-electron contrast, WD = 7 - 11 mm, EHT = 10 kV) showing the fracture morphology of Ti-B-N coatings D1, D2, D4 and D5 (top) and the adhesive TiN layer and WC/Co substrate (bottom).

4.2.4 XPS analysis

XPS analysis provides unique information about the binding properties of elements in compounds. Thus, it was used to study the chemical environment of the atoms in the Ti-B-N coatings. The information depth of XPS ($3\lambda_m$) is dependent on the inelastic mean free path (IMFP) λ_m in the examined energy range, which is here approximately 2 - 3 nm (68;

104; 105; 106). Thus, only surface information is obtained with an information depth of ~ 6 - 9 nm. By comparing the energetic positions of the core-level signals to literature data (121) or reference samples different components in the examined coatings can be identified.

Fig. 31 shows the evolution of the boron B1s core-level signals with increasing boron concentration for D1-D5 compared to data of the TiB_2 reference sample (Fig 31, top). Three main signals (vertical bars) are observed at energies of 187.5 eV, 190.8 eV and 192.2 eV. They are identified as belonging to boron in TiB_2, BN and B_2O_3, respectively (26; 122; 123).

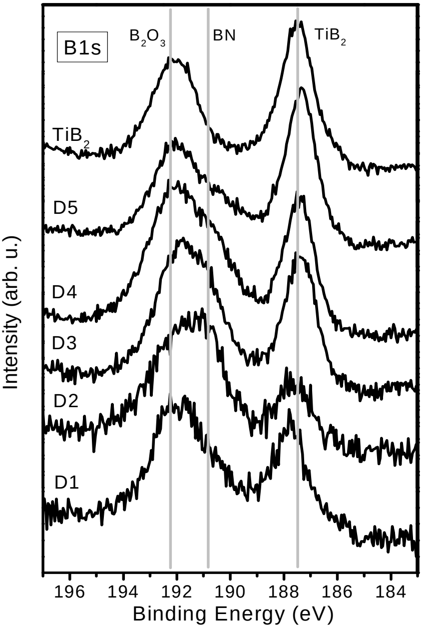

Fig. 31: XPS spectra of the B1s core-level signal of Ti-B-N coatings D1-D5 compared to data of the TiB_2 reference sample. Grey lines indicate the positions of the binding-energies of boron in TiB_2 (187.5 eV), BN (190.8 eV) and B_2O_3 (192.2 eV).

Boron nitride and boron oxide are assumed to be found mainly in the surface region due to the preparation conditions (15) and the high surface sensitivity of XPS, because their peak intensities vanish after sputter etching (15; 16). This assumption is further supported by the absence of BN and B_2O_3 signals in the XRD patterns (see above) as well as by the Raman spectra (see below), which are both more bulk sensitive methods.

Nevertheless, the relative amount of BN increases by the addition of boron in D1-D2, and decreases at the expense of TiB_2 in D2-D5. The relevant feature at the lowest binding-energy can be associated with TiB_2, the intensity of which clearly increase in samples D2 to D5. Furthermore, D2 shows an additional shoulder located at about 188.0 eV, and only this peak at 188 eV is obtained for D1. A comparison with the literature suggests that this signal may be attributed to boron that replaces nitrogen in the TiN lattice or substoichiometric titanium boron compounds, like TiB (121; 26; 122; 123). These results correlate well with data obtained from XRD, that show no TiB_2 phase in the coating with the lowest boron concentration (D1, B < 18 at %). Furthermore, the results suggest the formation of a boron-containing phase in D1 that was not evident from XRD measurements, most likely because the boron phase exhibits an amorphous structure.

The evolution of the titanium 2p core-level signals with increasing boron concentration for D1-D5 compared to data for the TiB_2 (top) and TiN (bottom) reference samples is shown Fig. 32. The most prominent features are found at energies of 454.3 eV, 455.7 eV and 458.8 eV (vertical bars) and are attributed to the $Ti2p_{3/2}$ species in TiB_2, TiN and TiO_2, respectively (26; 122; 123). The higher binding-energy peaks are derived from the $Ti2p_{1/2}$ components. TiO_2 is found on all surfaces and its formation results from the preparation process (15) and the contact of the samples with ambient air. With decreasing boron concentration, the peak located on the low-binding-energy side of TiO_2, which is related to TiB_2, shifts toward higher binding-energies, i.e., to the position associated with TiN. The transition from nitrogen-rich to boron-rich coatings is therefore directly reflected in the surface-sensitive XPS data presented here. Again, these results are in good agreement with the XRD data; both methods show the same trends.

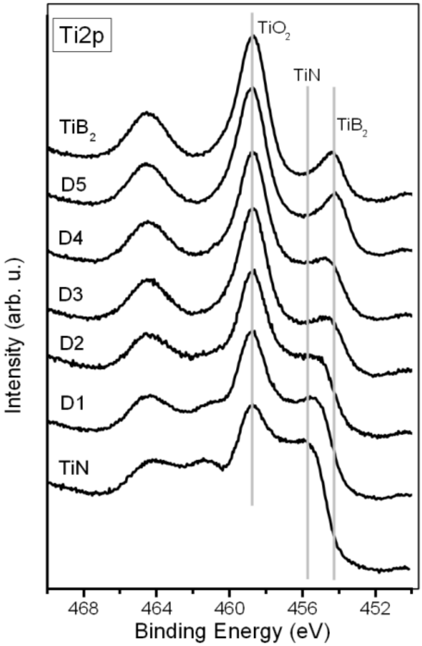

Fig. 32: XPS spectra of the Ti2p core-level signal of Ti-B-N coatings D1-D5 compared to data of the TiB_2 and TiN reference samples. Grey lines indicate the positions of the binding-energies of titanium in TiB_2 (454.3 eV), TiN (455.7 eV) and TiO_2 (458.8 eV).

Comparison of the N1s spectra of D1-D5 to the reference data for TiN (Fig. 33) indicates that there is no significant difference between TiN (397.1 eV) and the coating with the lowest boron concentration (D1). But with increasing boron concentration the TiN-related signal is reduced in favor of a peak related to BN at a binding-energy of 398.6 eV. As previously noted, this observation is most likely due to the very high surface sensitivity of XPS (≤ 10 nm) compared to the other techniques used in this study.

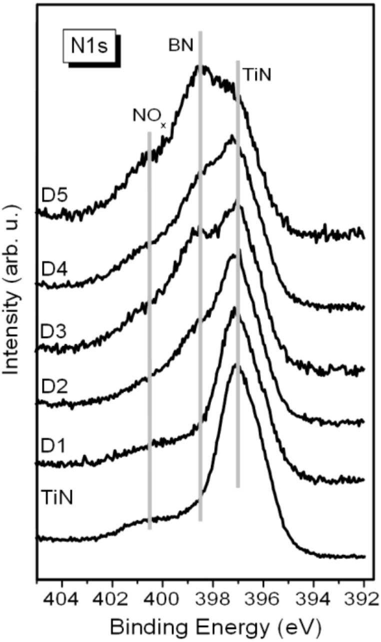

Fig. 33: XPS spectra of the N1s core-level signal of Ti-B-N coatings D1-D5 compared to data of the TiN reference samples. Grey lines indicate the positions of the binding-energies of nitrogen in TiN (397.1 eV), BN (398.6 eV) and NO_x (400.5 eV).

The results derived from the XPS datasets show good agreement with the XRD results and allow the identification of the relevant species formed during the CVD deposition process of Ti-B-N coatings D1-D5. The transition from TiN to TiB_2 is clearly observed in the core-level spectra of N1s, B1s and, in particular, Ti2p. The boron spectra show a discrepancy between the lowest and the higher boron concentrations, as also observed in the XRD analyses. Furthermore, the high surface sensitivity of the XPS probes, allows the detection of surface-enriched species, such as TiO_2, BN and B_2O_3, which are not observed in the bulk phases. However, in contrary to Raman spectroscopy no local information can be obtained.

4.2.5 Raman analysis

Characteristic modes of the examined coating materials are again obtained in the range between 100-1000 cm^{-1} due to defect-induced first-order Raman scattering (Fig. 34). These results will be discussed below. Furthermore, no significant peaks were detected by Raman spectroscopy (information depth in TiN ≈ 25 nm (112)) in the range between 1000-2000 cm^{-1}, where characteristic modes of BN phases are located (124). This supports the assumption, that the BN phases detected by XPS are only present in the very surface region.

Fig. 34 shows the Raman spectra of Ti-B-N coatings (D1-D5) with different boron concentrations. For comparison, the spectra of TiN and TiB_2 have been added at the bottom and top, respectively. The spectrum of TiN has already been described in Chapter 4.1.1.

For TiB_2 five signals at 245, 332, 433, 559 and 662 cm^{-1} are obtained. To the best of knowledge, Raman spectra of TiB_2 have not yet been reported, and therefore an assignment of the peaks to reference data is not possible. On the other hand, these spectral contributions may be ascribed to peaks in the density-of-states spectrum of TiB_2 (125; 126), similar to the case with TiN and as previously reported for the Raman spectra of other AlB_2-type transition-metal borides (127). Based on previous data (35), these bands may be ascribed to different acoustical and optical modes, i.e., TA (245 cm^{-1}), LA (332 cm^{-1}), 2A (433 cm^{-1}), TO (559 cm^{-1}) and LO (662 cm^{-1}). Compared to those of TiN and TiB_2, the spectral shape of the Raman spectra of Ti-B-N coatings D1-D5 shows some differences and becomes more complex. The differences in the acoustical range (150-350 cm^{-1}) are the most pronounced. Here, the spectra of coatings D1 and D2 (low boron concentration, $B \leq 18$ at %) exhibit a reproducible sharp and intense peak at 350 cm^{-1} (Fig. 34, grey line). This signal cannot be easily observed in the spectra of coatings D3-D5 with high boron concentrations ($B \geq 18$ at.%), TiN or TiB_2. It is therefore attributed to a compound, that forms only at low boron concentrations in the Ti-B-N system.

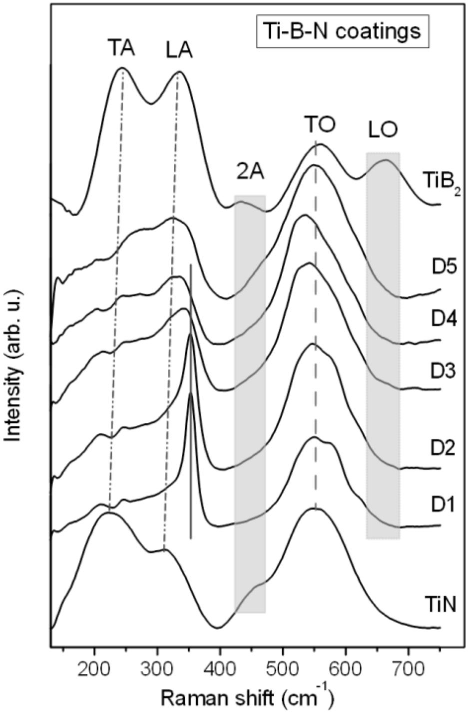

Fig. 34: Raman spectra of Ti-B-N coatings D1-D5 compared to TiN (bottom) and TiB_2 (top). TA, LA, 2A, TO and LO indicate the different phonon modes of the samples. The grey dotted and dashed lines are added for discussion in the text.

According to published accounts, TiB can be deposited by CVD from BCl_3 and TCl_4 at low partial pressures of boron trichloride (128). Therefore, TiB was synthesized as described in the Chapter 3.3 and examined by XRD and Raman spectroscopy. Indeed, by comparison with the Raman measurements of the reference sample, the peak at 350 cm^{-1} can unambiguously be attributed to TiB (see Fig. 35). Thus, the Raman spectrum of D1 can be well characterized as a superposition of the TiN and TiB spectrum, where all characteristic peaks of TiB (Fig. 35, *a*-*e*) can be found. The different relative intensities of the TiB and TiN peaks in the acoustical and optical region of the Ti-B-N spectrum may be explained by orientation effects. Whereas the CVD coatings exhibit a preferred orientation, the synthesized TiB sample is completely disordered. This may result in different intensities of the individual Raman modes.

In conclusion, the results of Raman spectroscopy confirm, in accordance to XRD and XPS, that a TiB_2 phase is hardly formed in the boron-poor ($B \leq 18$ at %) Ti-B-N coatings. Furthermore, these data demonstrate the high sensitivity of Raman spectroscopy to composition changes in the examined coatings. The appearance of this sharp and characteristic peak correlates also well with the XPS results (see above), in which a signal located at 188.0 eV was found in the B1s spectra of coatings D1 and D2.

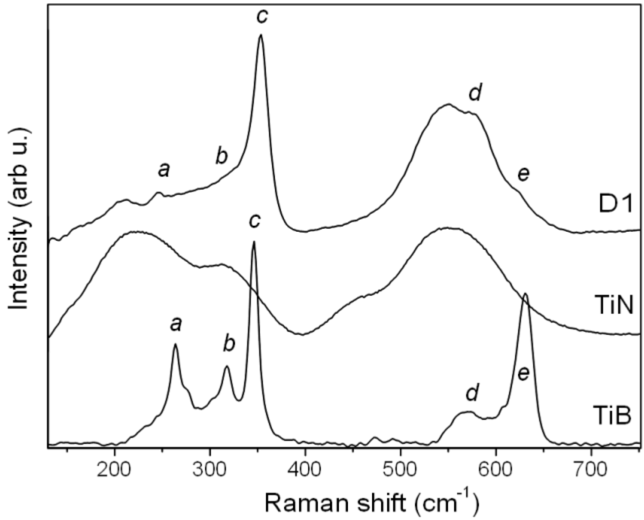

Fig. 35: Raman spectra of Ti-B-N coating D1 compared to the spectrum of TiN and TiB. *a-e* indicate the characteristic bands of TiB.

The Raman spectra of D2 is similar to that of D1, although small amounts of TiB_2 are assumed to be present, as indicated by XPS and XRD (see Figs. 29 and 31), in addition to the TiB. However, the signals of TiB_2 cannot clearly be identified in the Raman spectra of D2, most likely because of the superposition of the intense signals of excess TiB and TiN.

With increasing boron concentration in D3-D5, the TiB-related peaks vanish, whereas those of TiB_2 appear (see LA mode of TiB_2 in Fig. 34 – dashed-dotted line). This demonstrates the formation of TiB_2 in addition to TiN in these coatings, as also found by XRD and XPS. The spectra of D3-D5 may therefore result from a strong overlap between the Raman bands of TiN and TiB_2.

In the optical range, the transition from TiN over TiB to TiB_2 can also be observed. The TO mode (grey dashed line in Fig. 34) of D1 and D2 shows additional shoulders at 580 and 630 cm^{-1} compared to that of TiN, which correlate to peaks of TiB (see Fig. 35). As the TiB signals attenuate, the spectral shape of the TO mode becomes asymmetric in D3 and D4. This may also be attributed to internal stresses in these coatings due to the coexistence of the TiN and TiB_2 phases. Coating D5 mainly exists of TiB_2, as determined by XRD, XPS and WDS, and the TO mode is rather symmetric and similar to that of TiB_2. Furthermore, with the addition of boron, the 2A mode of TiN at 448 cm^{-1} vanishes, whereas at higher boron concentrations the 2A mode of TiB_2 at 433 cm^{-1} appears as a shoulder (Fig. 34, grey left box). Interestingly, the TO mode of TiB_2 completely disappears with the addition of nitrogen (grey right box). This may be due to the preferred orientations of the CVD coatings compared to the disordered TiB_2 reference sample, as already described for TiB (see above).

Nevertheless, the results clearly demonstrate that Raman spectroscopy is a complementary technique compared to XRD, SEM, WDS and XPS. The same transition trends were found in the examined Ti-B-N system during the transformation from TiN to TiB_2 by the addition of boron, and a good correlation between the different techniques was achieved. Furthermore, the high sensitivity of Raman spectroscopy regarding composition changes in the examined material system is clearly demonstrated by the spectra of coatings D1 and D2 with low boron concentrations. Here, only Raman spectroscopy was capable of detecting the existence of a boron containing phase, namely TiB.

4.2.6 Summary

Ti-B-N coatings with different boron concentrations have been prepared by MTCVD. The composition was characterized by WDS, XRD, SEM, XPS and Raman spectroscopy.

The results clearly demonstrate a good correlation between the different techniques. Despite the varying information depths and information contents, the same transition trends were observed in the examined Ti-B-N system in the progression from TiN to TiB_2 by the addition of boron.

At boron concentrations ≥ 18 at.%, the examined Ti-B-N coatings exhibit a two-phase structure of TiN and TiB_2 which was found by XRD and XPS. The high sensitivity of Raman spectroscopy to composition changes in the investigated system enabled on the other hand the clear identification of TiB in the Ti-B-N coatings with boron concentrations ≤ 18 at %. This phase was not detectable by XRD, most likely because of an amorphous structure, and it was only indicated by a weak (additional) signal in the XPS spectra.

In conclusion, the combination of different analysis methods, like WDS, XRD, SEM, XPS and Raman spectroscopy as demonstrated here, allows a precise characterization of the different phases in Ti-B-N coatings with varying boron concentrations.

4.3 Oxidation behavior of titanium-based hard coatings after static annealing

To gain better understanding of the high-temperature oxidation, Raman spectroscopy was used to study the oxidation processes of TiC, TiN, $TiC_{1-x}N_x$, $TiB_xC_yN_z$ and Ti-B-N coatings by the spectroscopic detection of the formed oxidation products. In addition to Raman spectroscopy, WDS and GIXRD were used to determine the oxidation depth and the oxide layer composition in the case of the Ti-B-N coatings. The aim was to develop a qualitative picture for the oxidation behavior of these kinds of coatings with different compositions.

Therefore, the coatings were annealed for 1 h under ambient conditions at 500 and 700°C. The possible oxidation products are primarily anatase and rutile. Anatase, the low-temperature (metastable, $T \geq 450°C$) modification of TiO_2, exhibits characteristic Raman peaks at 143, 397, 516 and 638 cm^{-1} (125). Rutile, the high-temperature (thermodynamically stable, $T \geq 600°C$) modification, shows peaks at 236, 444 and 608 cm^{-1} (125; 129). Furthermore, for $TiB_xC_yN_z$ and Ti-B-N coatings, boron oxide (B_2O_3; 500, 732, 801, 1260 cm^{-1}) is also a possible oxidation product (130). It is known that crystalline B_2O_3, formed at $T \geq 600°C$, easily transforms to volatile H_3BO_3 (heat of formation $\Delta_f H° = -1094.8$ kJ/mol) in the presence of moisture (33; 131; 132). Consequently boric acid (209, 499, 880, 1166 cm^{-1}) may also be detected in the Raman spectra of the oxidized samples (133).

As described in Chapter 2.3.4, boric acid is known to act as a self-lubricant and it is therefore a highly desired oxidation product with regard to the tribological behavior of coatings (95; 97; 98; 99).

Furthermore, volatile oxides of carbon and nitrogen, which possibly evaporate during annealing, may only be detected by in-situ Raman spectroscopy. However, this was not performed in this work.

Reference Raman spectra of the above listed oxidation products are summarized in Fig. 36.

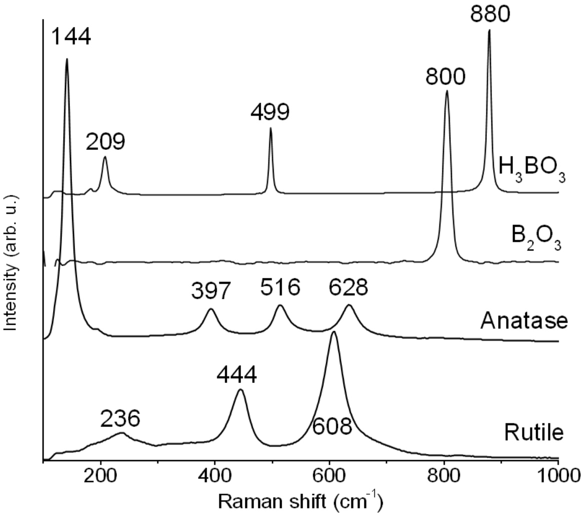

Fig. 36: Raman spectra of B_2O_3, H_3BO_3, rutile and anatase.

It should be mentioned, that the coatings were also annealed for 1h at 300°C in addition to 500 and 700°C. However, none of the investigated coatings oxidized under these conditions to such an amount that it was detectable by Raman spectroscopy (the information depth in the case of pure TiO_2 is $\approx$ 1µm (112)) or even GIXRD (information depth 0.13-1.3 µm for TiO_2 at angle of incidences between 0.5 - 4° (85)). These data are thus not shown or discussed herein.

4.3.1 Oxidation behavior of $TiC_{1-x}N_x$ coating (A- and a-series)

After being annealed at 500°C for 1 h the TiC, TiN, HT- (A1, A2 and A4) and MT- $TiC_{1-x}N_x$ (a4) coatings oxidized to different products within the information depth of Raman. This can be seen in Fig. 37.

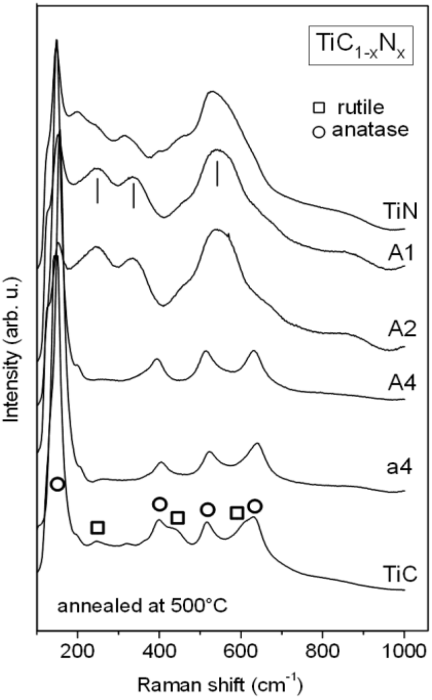

Fig. 37: Raman spectra of different $TiC_{1-x}N_x$ coating after annealing for 1h at 500°C. ○ denotes anatase, □ rutile, vertical bars indicate signals of un-oxidized $TiC_{1-x}N_x$.

The spectrum of TiC in Fig. 37 already exhibits a mixture of anatase and rutile at this temperature, and carbon-rich $TiC_{1-x}N_x$ coatings like a4 and A4 are completely oxidized to anatase. On the other hand, the nitrogen-rich coatings A1 and A2 show only a beginning oxidation to anatase (sharp and intense peak at 143 cm^{-1}) and still bands of the un-oxidized coating surface can be obtained (indicated by the vertical bars). Thus, a correlation between C:N ratio and oxidation behavior in the coatings can be observed. The higher the carbon concentration in the $TiC_{1-x}N_x$ coatings, the easier they get oxidized (correlating to a higher oxidation depth). It is well known that the oxidation resistance generally decreases with increasing carbon concentration (134). This fact can be explained by the Gibbs energy of oxidation which is more negative for TiC (- 1122 kJ/mol) than for

TiN (- 582 kJ/mol). Accordingly the tendency for oxidation is stronger for TiC and carbon rich $TiC_{1-x}N_x$ coatings (2; 29; 134; 135).

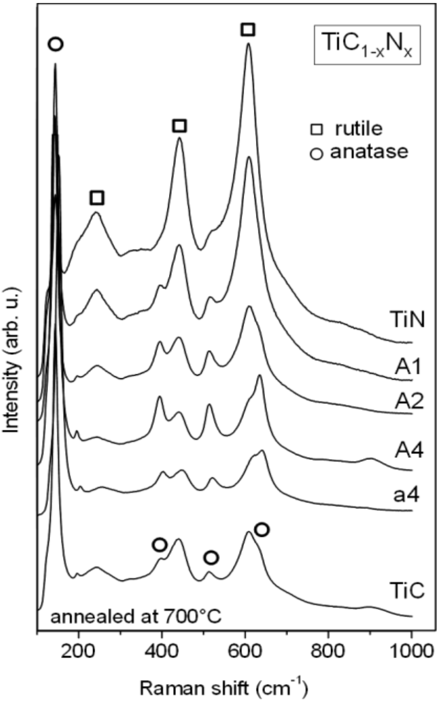

Fig. 38: Raman spectra of different $TiC_{1-x}N_x$ coating after annealing for 1h at 700°C. ○ denotes anatase, □ rutile.

However, after being annealed at 700°C for 1 h, the oxidation trends of the coatings changed (see Fig. 38). The nitrogen-rich coatings (TiN and A1) predominantly oxidize to rutile, which is the expected oxidation product at 700°C, with only small peaks of anatase left. The carbon-rich coatings, on the other hand, still show a mixture of anatase and rutile in different ratios In conclusion, with decreasing carbon concentration in the $TiC_{1-x}N_x$ coatings the rutile peaks get more pronounced.

The oxidation behavior of the coatings at 700°C seems to be in contradiction with the Gibbs energies of oxidation. Looking at thermodynamics only, rutile, the high-temperature modification of TiO_2, is most likely to be formed by the less oxidation stable coatings with high carbon concentrations. The reason for the observed opposite behavior may be related to the different composition of the oxide layer. For TiC, a change in oxidation kinetics as well as in the relative anatase and rutile concentration with temperature has been reported (2; 136). At higher temperatures further oxidation was inhibited by forming a denser oxide layer. Following these reports, it can be assumed that at 700°C the coatings with high carbon concentrations will form a denser oxide layer than those formed at 500°C. Therefore the oxidation of the coating may be retarded due to kinetic effects.

4.3.2 Oxidation behavior of $TiB_xC_yN_z$ coatings (B-, C- and c-series)

Oxidation behavior of HT- $TiB_xC_yN_z$ (B-series)

Low boron concentrations in TiN coatings are known to improve the thermal stability (23; 32). To compare the oxidation resistance of low boron containing $TiB_xC_yN_z$ coatings with $TiC_{1-x}N_x$, the coatings B1-B5 were annealed under analogous conditions as used for the A- and a-coatings.

As described in Chapter 3.1, the $TiB_xC_yN_z$ coatings are covered by a wear-indicating Ti-B-N layer. But influences of boron diffusion through the thermal treatment from the top layer into the examined $TiB_xC_yN_z$ coating could be excluded by SEM-EDX line scans through the calottes. Furthermore, Raman spectra of the oxidized samples were taken at various positions in calottes to confirm homogeneity and reproducibility.

After being annealed at 500°C for 1 h, Raman spectroscopy evidently indicates oxidation of the coatings by significant changes in their spectra (see Fig. 39). The Raman spectrum of nitrogen-rich B1 can be well characterized by a mixture of $TiB_xC_yN_z$ and anatase. With increasing carbon concentration in B1-B3, the anatase related peaks become more pronounced. The spectra of B2 and B3 correlate to a full oxidation of the sampled layer to anatase. Interestingly, with even higher carbon concentrations in B4 and B5, the spectra already exhibit a mixture of rutile and anatase at this temperature similar to TiC.

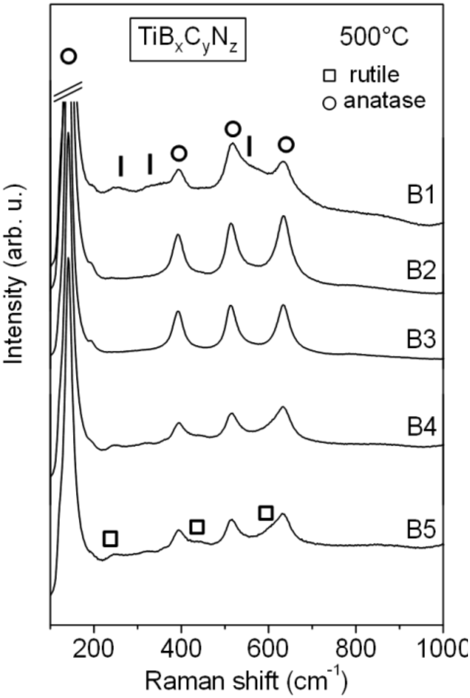

Fig. 39: Raman spectra of HT-$TiB_xC_yN_z$ coatings B1-B5 after annealing for 1h at 500°C. ○ denotes anatase, □ rutile, vertical bars indicate signals of un-oxidized $TiB_xC_yN_z$.

These results suggest that the boron-doped $TiB_xC_yN_z$ coatings show the same tendencies as $TiC_{1-x}N_x$. The higher the carbon concentration in $TiB_xC_yN_z$ coatings, the easier they get oxidized at 500°C. This is again in accordance to the Gibbs energy of oxidation (see above). Furthermore, it seems that boron-doping of carbon-rich $TiC_{1-x}N_x$ coatings reduces the oxidation resistance to such an amount that rutile is already formed at 500°C although it is expected to be the stable modification of TiO_2 at T > 600°C (20).

Raman spectra of coatings after being annealed at 700°C show similar to $TiC_{1-x}N_x$ different relations between coating composition and oxidation products (Fig. 40). The nitrogen-rich coatings B1-B3 predominantly oxidize to rutile with only weak peaks of anatase left in the spectra. The spectra of carbon-rich coatings B4 and B5 exhibit features of a mixture of anatase and rutile in different ratios. Yet again, the oxidation behavior of the coatings at 700°C seems to be in contrast to the Gibbs energies of oxidation and may therefore be explained by kinetic effects.

Furthermore, the Raman spectra of some oxidized coatings show a sharp peak located at 880 cm^{-1} which may be attributed to H_3BO_3 (133), likely formed during oxidation in presence of ambient humidity.

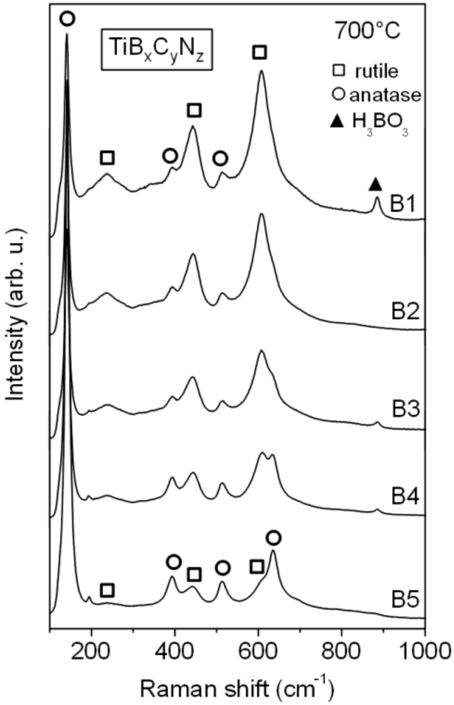

Fig. 40: Raman spectra of HT-$TiB_xC_yN_z$ coatings B1-B5 after annealing for 1h at 700°C. ○ denotes anatase, □ rutile, ▲ H_3BO_3.

Oxidation behavior of HT- $TiB_xC_yN_z$ (C-series)

To confirm the possible formation of boric acid as well as to shed further light on the capacity of boron to affect the thermal stability of $TiC_{1-x}N_x$, the $TiB_xC_yN_z$ coatings C1-C5 were annealed at 500 and 700°C (Fig. 41).

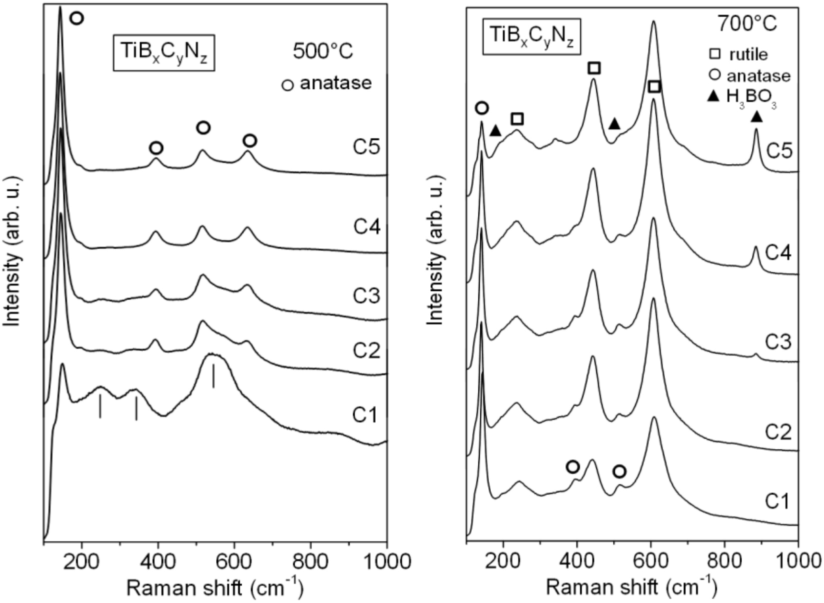

Fig. 41: Raman spectra of HT- $TiB_xC_yN_z$ coatings C1-C5 after annealing for 1h at 500°C (left) and 700°C (right). ○ denotes anatase, □ rutile, ▲ H_3BO_3, vertical bars indicate signals of unoxidized $TiB_xC_yN_z$.

After thermal treatment at 500°C, the Raman spectrum of the boron free $TiC_{1-x}N_x$ coating (C1) shows only a small amount of oxidized material, indicated by a sharp and intense peak at 143 cm^{-1} (anatase). With increasing boron concentration in $TiB_xC_yN_z$ coatings C2-C5, the anatase peaks get more intense, and the spectra of coatings C4 and C5 correlate to full oxidation to anatase within the information depth of Raman. After being annealed at

700°C, Raman spectra of all coatings show a mixture of anatase and rutile peaks, whereas $TiB_xC_yN_z$ features cannot be observed anymore. The rutile-related peaks increase with the boron concentration at the expense of the anatase peaks. In conclusion, with increasing boron concentration in the coatings, a higher degree of oxidation is observed at 500°C and 700°C. Furthermore, with a higher concentration of boron in $TiB_xC_yN_z$, the peak located at 880 cm^{-1} gets more pronounced, likely confirming the presence of H_3BO_3 as an oxidation product of boron (133).

As already mentioned above, boric acid is a very attractive oxidation product due to its self-lubricating characteristics (95; 97; 98; 99). Therefore with regard to the practical application, it can be assumed that the $TiB_xC_yN_z$ coatings exhibit a higher wear resistance compared to $TiC_{1-x}N_x$, which may further increase with higher boron concentrations, although the oxidation resistance was found to be lower and likewise decreases with increasing boron concentration.

Oxidation behavior of MT- $TiB_xC_yN_z$ (c-series)

Since the MT-$TiB_xC_yN_z$ coatings c1-c5 showed quite similar oxidation tendencies as the HT-$TiB_xC_yN_z$ coatings C1-C5, only a short summary of their oxidation behavior will be given.

It was found that with increasing BCl_3 flow rate the oxidation resistance of MT-$TiB_xC_yN_z$ coatings decreases at 500 and 700°C. The spectra of oxidized coatings c1-c5 after being annealed at 700°C for 1 h are exemplarily shown in Fig. 42.

It can clearly be seen, that with increasing BCl_3 flow rate, the anatase related peaks vanish, whereas those of rutile increase. This observation correlates very well with the results of the HT-$TiB_xC_yN_z$ coatings C1-C5.

However, in contrast to the HTCVD coatings, no signals of H_3BO_3 could be obtained for any of the MT-$TiB_xC_yN_z$ coatings. A possible explanation for this observation can be given by following the reports on former coatings analysis (5; 6). They reveal that in the

MTCVD process the boron concentration in the coatings cannot be varied in a wide range by changing the precursors flow rates. Furthermore, due to the lower deposition temperature, it can be assumed that less boron is incorporated into the growing film compared to the HTCVD process. Thus, identification of oxidation products of boron is most likely not possible in MT-TiB$_x$C$_y$N$_z$ coatings c1-c5 since their amount appears to be less than the detection limit of Raman spectroscopy.

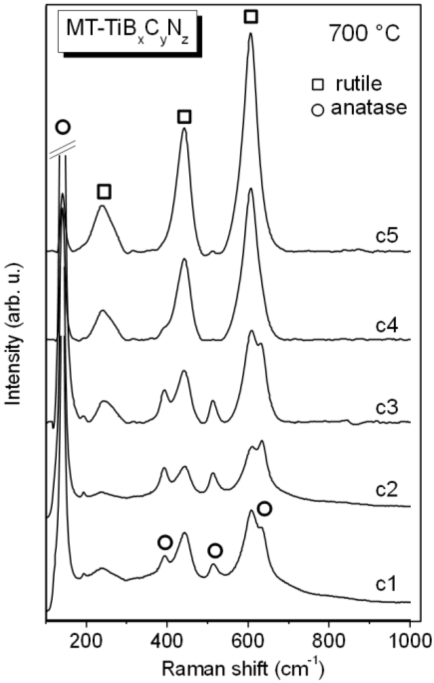

Fig. 42: Raman spectra of MT-TiB$_x$C$_y$N$_z$ coatings c1-c5 after annealing for 1h at 700°C. ○ denotes anatase, □ rutile.

3.3.3 Oxidation behavior of Ti-B-N coatings (D-series)

As mentioned before, low boron concentrations in TiN coatings are known to improve the thermal stability (23; 32). To compare the oxidation resistance of Ti-B-N coatings D1-D5 with TiN, the samples were similarly annealed for 1 h at 500 and 700°C under ambient conditions.

Here, in addition to Raman spectroscopy, GIXRD and WDS were used for analyzing the oxidized coatings.

The influence of boron diffusion and the oxidation depth was estimated by WDS line scan measurements, i.e. the variation in the X-ray intensity of boron, oxygen and titanium was analyzed across a straight line over the whole coating on cross-sections. The line scans on the cross-sections of the annealed samples revealed a rather homogeneous boron distribution over the whole Ti-B-N layer with an overall boron concentration similar to the un-annealed coatings. For the coating with the highest boron concentration (D5), the oxidation depth, as estimated by oxygen line scans, was approximately 1 µm after the sample was annealed at 500°C (see beam location (= y-axis) in Fig. 43, right side of the scans), and it increased to about 2 µm after it was annealed at 700°C (Fig. 43, left side of the scans).

GIXRD was further used to evaluate the oxidation depth and to identify the composition of the oxide layers. Diffraction patterns were taken at incident angles of 0.5-4°, which correspond to penetration depths of 0.13-1.3 µm in the case of pure TiO_2. After boron-rich coatings (D3-D5) were annealed at 500°C, only reflections from TiO_2 could be obtained at incidence angles from 0.5-2°, but none were observed from the Ti-B-N coating. At an incidence angle of 3°, peaks related to TiB_2 began to appear, which correlats to an oxide layer thickness of approximately 1 µm. This is in good agreement with the WDS measurements. The reflections of the oxides observed at lower angles and therefore at the top of the layer could be attributed primarily to anatase and only small amounts of rutile. Compared to the Raman results of the oxidized $TiC_{1-x}N_x$ and $TiB_xC_yN_z$ coatings, these compounds are the expected oxidation products after annealing at temperatures < 700°C.

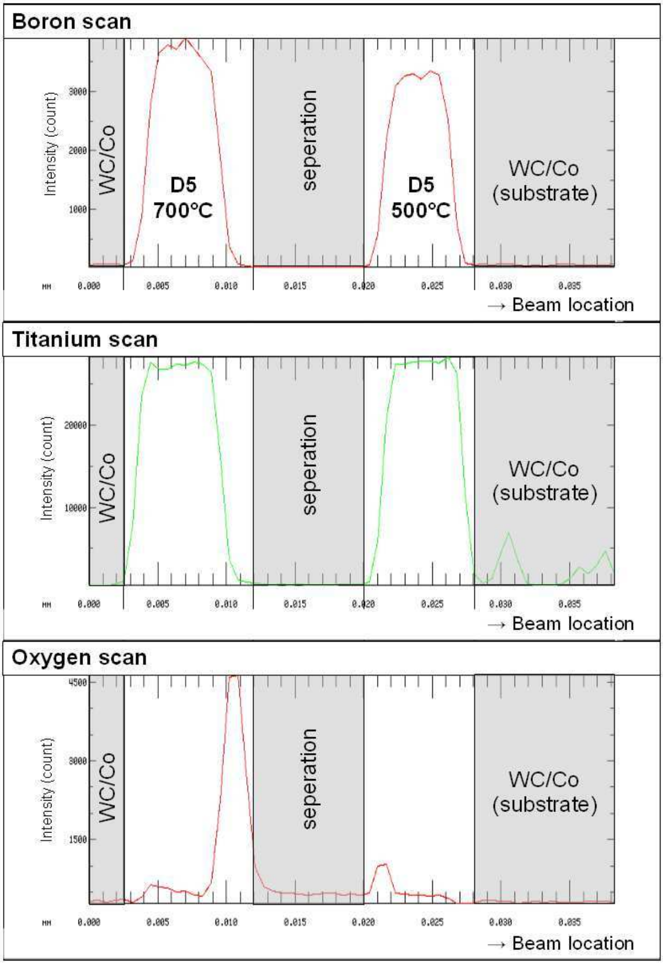

Fig. 43: WDS line scans analyzing the variation in the X-ray intensity of boron, titanium and oxygen across a straight line over two cross-sections of D5 (sperated by a metall foil, grey areas in the middle) after oxidation for 1h at 500°C (right side) and 700°C (left side). The Ti-B-N layer is given by the white areas, the grey areas at the right and left side correlate to the substrate (WC/Co).

After coating D5 was annealed at 700°C, no significant reflections of Ti-B-N could be observed by GIXRD, even at an incidence angle of 4°; therefore, the oxide layer is assumed to be thicker than 1.3 µm. The bulk of the oxide layer (higher incidence angle) mainly consists of rutile, whereas anatase and boron oxides are more pronounced at the outer part of the oxide layer (see Fig. 44, ○ anatase, □ rutile,□ boron oxide).

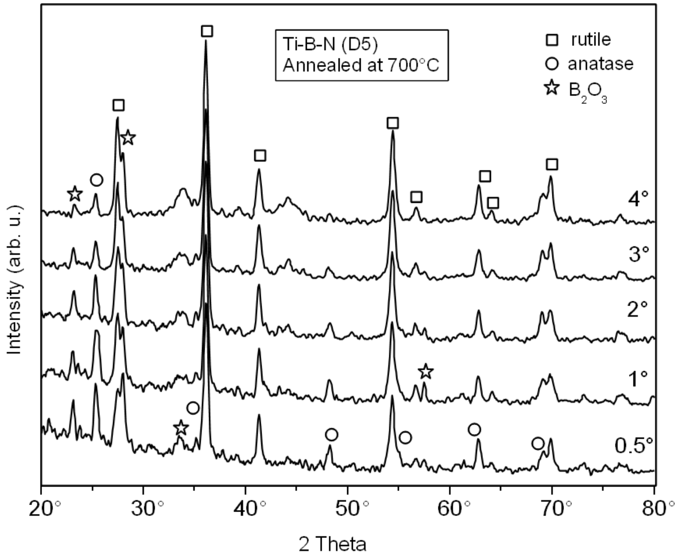

Fig. 44: GIXRD patterns of Ti-B-N coating D5 after annealing at 700°C for 1h with incidence angles varying from 0.5-4°. ○ denotes anatase, □ rutile, ☆ B_2O_3.

For TiB_2 coatings, similar results have already been reported (137; 138). The formation of a double oxide layer was observed after oxidation at temperatures between 600-800°C; the layer consists of a rutile inner layer, and a two-phase top layer composed of B_2O_3 with anatase inclusions. These authors suggested the strong protective qualities of B_2O_3 as an explanation, which may lead to the formation of the metastable anatase rather than rutile (137).

In the present investigation, Ti-B-N coatings with low boron concentrations (D1 and D2), however, exhibited only small amounts of oxides signals in the GIXRD patterns. After the samples were annealed at 500°C, primarily anatase was observed, and the oxide layer thickness was estimated to be approximately 0.5 µm. After being annealed at 700°C, the coatings produced diffraction peaks of predominantly rutile, and an oxidation depth of approximately 1 µm was observed.

In addition to XRD, Raman spectroscopy was used to study the composition of the oxide layers. The Raman spectra of the oxidized Ti-B-N coatings (Figs. 45 and 46) also include the spectra of TiN at the bottom for a better comparison, although the oxidation behavior of TiN is already described in Chapter 4.3.1.

After being annealed at 500°C, Ti-B-N coatings D1-D5 exhibit significant changes in their Raman spectra (Fig. 45, ○ anatase, □ rutile) compared to the un-oxidized samples (see Chapter 4.2.5). The spectra of boron-poor Ti-B-N coatings D1-D2 can be well characterized by a mixture of the un-oxidized samples and TiO_2 (mainly anatase, only weak shoulders of rutile). With increasing boron concentration in D1-D5, the TiO_2-related peaks become more pronounced, whereas those of Ti-B-N vanish. The spectrum of D5 correlates to full oxidation of the sampled layer within the information depth of Raman (~ 1 µm), and the spectrum exhibits a mixture of anatase and rutile at 500°C.

In conclusion, the degree of oxidation (oxidation depth) increases with increasing boron-concentration in Ti-B-N from D1-D5, which is in accordance with the GIXRD and WDS results, and furthermore correlates very well with the results obtained for $TiB_xC_yN_z$ coatings (see Chapter 4.3.2).

The Raman spectra of samples annaeld at 700°C (Fig. 46, ○ anatase, □ rutile, □ B_2O_3, ▲ H_3BO_3) show the same trends in the devolution of the coating composition and the degree of oxidation, but differences were observed regarding the generated oxidation products.

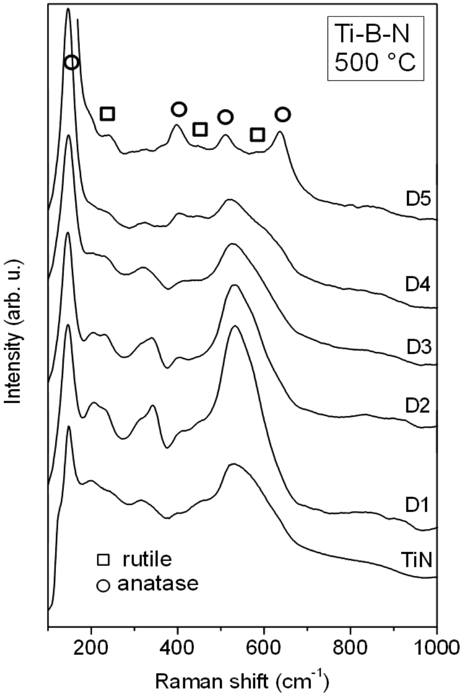

Fig. 45: Raman spectra of Ti-B-N coatings D1-D5 and TiN (bottom) after annealing at 500°C for 1h. ○ denotes anatase, □ rutile.

As already described above, the spectrum of TiN exhibits only features of oxidation products after being annealed at 700°C. In contrast, D1 and D2 still exhibit peaks of the un-oxidized Ti-B-N coating surface in their spectra, as indicated by the sharp peak at ~ 350 cm^{-1} of TiB (see Fig. 46), owing to a lower degree (depth) of oxidation. The observation of an increased oxidation resistance at 700°C by the addition of small amounts of boron (≤ 18 at %) to TiN is in good agreement with the results of other studies (23; 32; 33; 34). Most likely, the increased oxidation resistance is correlated to the existence of TiB in these coatings, and TiB is reported to be stable up to 800°C. Furthermore, TiB is known to improve oxidation resistance and to decrease the oxide layer thickness (139; 140).

The important role of TiB in oxidation behavior is further supported by the observation that Ti-B-N coatings with higher boron concentrations (> 18 at %; D3-D5) show, in contrast to D1 and D2, full oxidation in their Raman spectra after oxidation at 700°C (Fig. 46). The oxide layer mostly consists of rutile, and in addition, peaks of boron oxide at 800 cm^{-1} and of the possible self-lubricant boric acid at 210, 500 and 880 cm^{-1} are found.

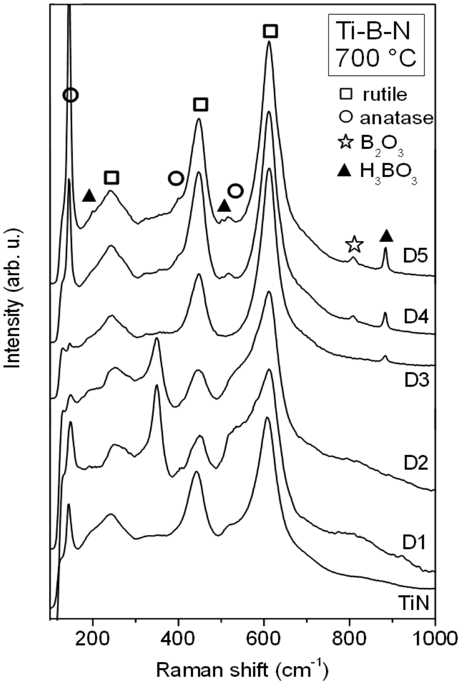

Fig. 46: Raman spectra of Ti-B-N coatings D1-D5 and TiN (bottom) after annealing at 700°C for 1h. ○ denotes anatase, □ rutile, ☆B_2O_3, ▲ H_3BO_3.

Crystalline B_2O_3 reportedly possesses strong protective qualities. It has also been reported to effectively heal pores and macro-defects, and seems to support the formation of anatase instead of rutile (137). Furthermore as already mentioned before, it easily transforms to

H_3BO_3 in the presence of residual moisture (33; 131; 132), which would be favorable for tribological applications (see Chapter 2.3.4).

The protective role of B_2O_3 against the formation of the thermodynamically more stable rutile is indicated by the well-pronounced anatase peak at 143 cm^{-1} observed in Ti-B-N coatings D4 and D5, where boron oxide was observed. In Ti-B-N coating D3, only small amounts of boric acid were detected, and the coating surface was completely transformed to rutile.

4.3.4 Summary

The oxidation behavior of TiC, TiN, $TiC_{1-x}N_x$, $TiB_xC_yN_z$ and Ti-B-N coatings were studied by annealing the samples for 1h at 300, 500 and 700°C and inspecting the oxidation products by Raman spectroscopy, GIXRD and WDS.

It was found that oxidation products like anatase, rutile and different boron oxides can easily be distinguished by Raman spectroscopy. The oxidation depth and the oxide layer composition correlates well with results obtained by WDS and GIXRD.

The degree of oxidation is largely dependent on the coating composition (C:N ratio as well as boron concentration). In $TiC_{1-x}N_x$ and $TiB_xC_yN_z$ coatings the extent of static oxidation at 500°C can be explained by decreasing oxidation resistance with increasing carbon concentration. Kinetic effects retard the further oxidation at 700°C, therefore a higher relative anatase concentration is observed in carbon-rich coatings. Direct comparison of $TiC_{1-x}N_x$ with $TiB_xC_yN_z$ coatings shows a higher degree of oxidation with increasing boron concentration as well as an evolution of boron oxides.

The oxidation behavior of the Ti-B-N coatings was found to be highly affected by the boron concentration. Low boron-concentrations ($B \leq 18$ at %) improve the thermal stability compared to TiN at annealing temperatures up to 700°C. This behavior most likely correlates to the TiB phase in these coatings, which obviously enhances the oxidation resistance and decreases the thickness of the oxidation layer. Coatings with a high boron concentration exhibit a higher degree of oxidation compared to TiN after being annealed at 500°C. In contrast, at $T_a > 600°C$, these coatings form boron oxides on their surfaces, which exhibits protective qualities and leads to the formation of metastable anatase rather than the thermodynamically stable rutile.

4.4 Laser-induced effects on titanium-based hard coatings

In addition to the oxidation after static annealing, it was found that the boron-rich Ti-B-N coatings as well as the TiB_2 coating begin to oxidize at ambient conditions upon increasing the laser power on the sample surface. For the other titanium coatings investigated in this work, also different laser-induced effects could be observed. In this chapter such effects will be discussed.

It is well known (79; 141; 142; 143) that the high density of power from a laser excitation source often poses a problem in Raman experiments. This is particularly true for Raman micro-spectroscopy, where the laser beam is focused to a spot size of only a few micrometers or less. Due to the absorption of the applied radiation, the local spot temperature may increase by hundreds of degrees. The temperature rise depends thereby on quantities such as laser power, dimension of the excited sample surface, exposure time, wavelength of radiation as well as color reflectivity and thermal conductivity of the sample (142; 143). As a result, wavenumber shifts of the Raman modes may occur, or even the alteration of the examined samples due to oxidation, recrystallization, phase transition or decomposition. (75; 79; 141; 144; 145; 146)

In order to demonstrate the laser-induced effects on TiB_2 and Ti-B-N, exemplary Raman spectra of the TiB_2 coating obtained with irradiation at different power levels from 1.6-16 mW are shown in Fig. 47. The spectrum recorded at the highest laser power (16mW) resembles that of the high-temperature form of TiO_2, rutile. The intermediate spectra taken at 4 and 8 mW laser power, however, show a peak between 147 and 150 cm^{-1} which is quite close to the characteristic, very strong peak of anatase (143 cm^{-1}), indicating the transition of TiB_2 to such an anatase structure at lower laser powers. On the contrary, the spectrum recorded at the lowest laser power does not appear to be affected, even at repeated and longer measurement times.

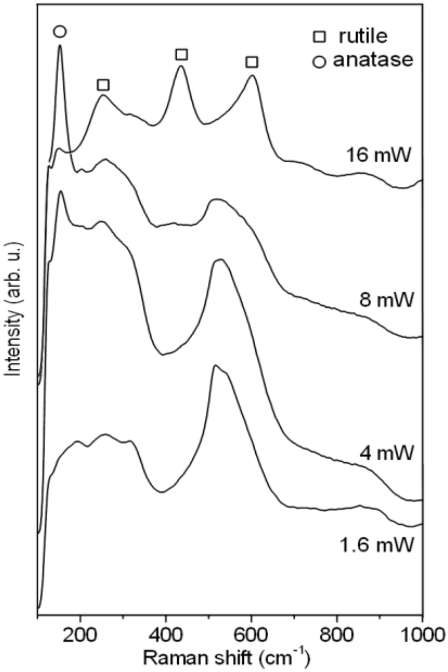

Fig. 47: Raman spectra of a TiB_2 coating recorded at different laser powers from 1.6 – 16 mW. ○ denotes anatase, □ rutile.

For a comparative study, Raman spectra of two rutile single crystals (100) and (111) are compared with the completely oxidized spectra taken at high laser powers of TiB_2 and Ti-B-N coatings D4 and D5 (Fig. 48). The spectra of the oxidized TiB_2 and Ti-B-N coatings still show a small anatase peak at 147-152 cm^{-1}. However, the intense high energy peak at 600-604 cm^{-1} reveals the almost complete transformation to rutile.

Even if the spectral shape does not change significantly with additional irradiation, their two lower energy peaks do not match exactly with the corresponding peaks of rutile at 236 and 444 cm^{-1}. The observed shift of the lower-energy peaks in both anatase and rutile can be attributed to oxygen deficiencies as reported by Parker and Siegel (147). This may indicate a slight deviation from stoichiometry in the laser-formed TiO_2. Furthermore, thermal shifting of the peaks due to thermal load as described in the next sections may contribute as well.

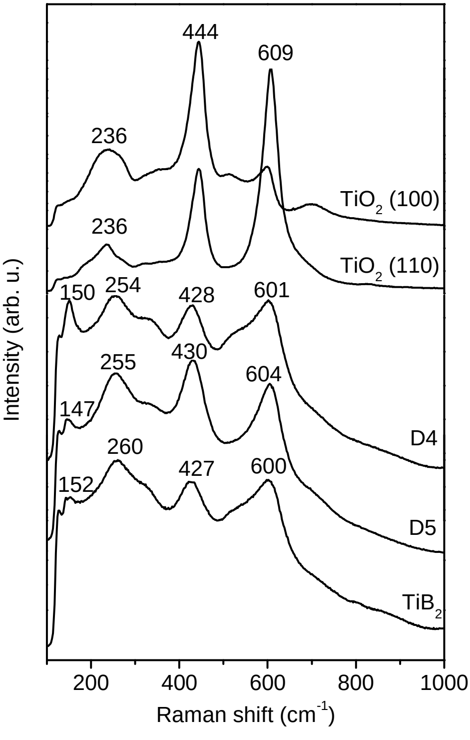

Fig. 48: Raman spectra of two rutile single crystals (100) and (111) compared to the completely oxidized spectra of TiB_2 and Ti-B-N coatings D4 and D5 taken at high laser powers of 16 mW.

The spectra of the boron-poor coatings D1 and D2 do not show such changes even with the highest laser power used in this study of 16 mW. This is in good agreement with the results of oxidation after annealing (see Chapter 4.3.3) and can most likely be explained by the existence of an oxidation-stabilizing TiB phase in these coatings.

Furthermore, laser induced oxidation can only take place, if of course oxygen is present, and the temperature sufficiently increases as a result of the absorption of the exciting radiation. As already mentioned above the temperature rise depends thereby on various quantities such like the thermal conductivity of the sample. As described in Chapter 4.2.3, with higher boron concentration the grain size of the Ti-B-N coatings decreases and as a result the thermal conductivity of these coatings may decrease. This may further lead to a higher local spot temperature in the boron-rich coatings.

The problem of laser induced oxidation could easily be prevented by placing the samples in a small inert atmosphere cell under a flowing stream of argon. However, the local heating through laser irradiation still causes a band-shift to lower wavenumbers (see Fig. 49) which may be related to thermal expansion of band lengths. This has to be taken into account carefully, when specifying precise peak positions.

$TiC_{1-x}N_x$ coatings, on the other hand, do not undergo laser-induced oxidation at the different laser powers used in this work. Therefore it was not necessary to measure under argon. But similar band shifting as found for Ti-B-N coatings were obtained.

Fig. 49 exemplarily demonstrates the dependence of the band position of the transversal optical mode at ~550 cm^{-1} of the HT-$TiC_{1-x}N_x$ coatings A1-A3 (black lines) as well as the vibration at ~ 545 cm^{-1} of Ti-B-N coatings D2, D4 and D5 (grey lines) on different laser powers. With increasing laser power, and thus higher local temperature, a nearly linear shift is observed. This shift may become up to 10 cm^{-1} from 1.6-16 mW. Similar results were obtained for the other titanium coatings investigated in this work.

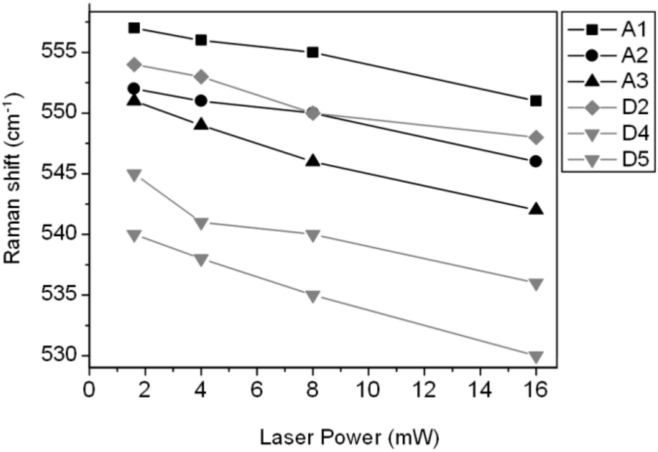

Fig. 49: Dependence of the Raman band position of HT- $TiC_{1-x}N_x$ coatings A1-A3 (black lines) and Ti-B-N coatings D2, D4 and D5 (grey lines) on different laser powers.

In conclusion, when analyzing Raman spectra of $TiC_{1-x}N_x$, $TiB_xC_yN_z$ and Ti-B-N coatings, not only the C:N ratio and boron concentration has to be taken into account, but also the laser power has to be chosen appropriately to avoid measurement artifacts.

To compare different peak positions (like in Chapter 4.1.1) same laser powers, exposure times, wavelengths of radiation and focal point diameters need to be used. The laser power should thereby be chosen in that way, that a sufficient signal-to-noise ratio is obtained, but on the other hand, no laser-induced alternation of the examined coatings occur. Therefore, all spectra shown in this work of TiN, TiC and $TiC_{1-x}N_x$ and $TiB_xC_yN_z$ were recorded with a laser power 8 mW, whereas for TiB_2 and Ti-B-N coatings a laser power of 4 mW was chosen. The boron-rich coatings were thereby examined under an argon atmosphere to prevent oxidation (see also Chapter 3.4.1).

4.5 Tribological behavior of Ti-B-N coatings

Motivated by the detection of large amounts of the self-lubricating compound boric acid in boron-rich Ti-B-N coatings after annealing (see Chapter 4.3.3), the tribological properties of the Ti-B-N coating D5 were studied at room and elevated temperatures (25-700°C) and compared to those of single-phase TiN. The results will be discussed in the following Chapter.

Ball-on-disk sliding tests were performed using Al_2O_3 and 100Cr6 bearing steel as counterparts. The sliding distance was set to 300 m, a typical value in tribology testing to determine the wear behavior and friction coefficient, and furthermore comparable to the turning tests performed in this work. These kind of sliding tests will hereafter be abbreviated as LTS (= long track sliding). Post-test ex-situ Raman analysis was performed on the samples to examine the types of formed oxides on the wear track after sliding. The identified compounds were correlated to the observed friction coefficients of the coatings.

Since thick transfer layers hindered the detection of the interfacial composition of the Ti-B-N coating after LTS testing against 100Cr6, a complementary set of ball-on-disk tests was performed at exceptionally short sliding distances of 0.3 m (= STS – short track sliding) at room temperature. In this way a comparatively thin transfer layer is obtained and the surface chemistry changes in the wear tracks can be analyzed by Raman spectroscopy. For better comparison with the samples after LTS testing at elevated temperatures, the STS-samples were post-annealed at different temperatures and durations, since the surface composition is likely to change during tribological testing (i.e. during heat-up and cooling-down). In this way the temperature dependence of chemical reactions at the interfaces could be studied more precisely.

In addition to the ball-on-disk tests, turning tests with Ti-B-N (D5) coated inserts were performed at various turning speeds. The compounds identified by Raman spectroscopy on the rake face were compared to those found on the wear tracks after LTS and STS testing. In this way, an approximate value for the contact temperature in machining operations could be estimated.

4.5.1 Characteristics of the Ti-B-N coating D5

For the direct comparison of the tribological properties of the Ti-B-N coating D5 with single-phase TiN, it is important to directly compare the coatings characteristics. Therefore, an XPS analysis was performed to analyze the surface composition of the coatings.

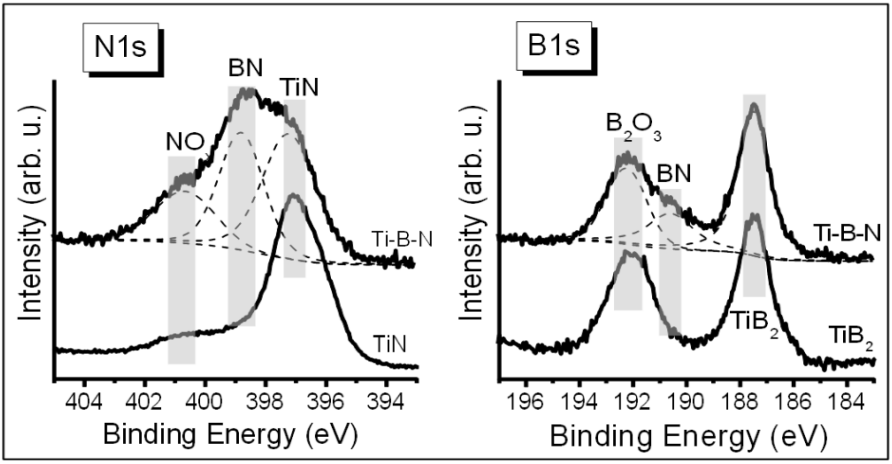

Fig. 50: XPS data of the N1s region (left) of TiN and Ti-B-N coating D5 as well as in the B1s region (right) of TiB_2 and D5, showing the coexistence of titanium nitride and titanium diboride in the investigated sample.

As already described in Chapter 4.2, the Ti-B-N coating D5 is predominantly composed of hexagonal TiB_2, and small amounts of cubic TiN. This becomes evident by the curve fittings of the XPS core-level spectra of D5 in the N1s (Fig. 50, left) and the B1s (right) regions compared to the reference TiN and TiB_2 samples. In the N1s region three main signals can be found (grey vertical bars in Fig. 50) at energies of 397.1 eV, 398.6 eV and 400.9 eV. They can be attributed to nitrogen in TiN, BN and NO_x respectively (26; 122; 123). Furthermore, in the B1s region three signals are located at 187.5 eV, 190.8 eV and 192.2 eV correlating to boron in TiB_2, BN and B_2O_3 (26; 122; 123). The different oxide phases as well as the boron nitride found in the XPS spectra are assumed to exist mainly in the surface region as explained in Chapter 4.2. In addition to XPS, the XRD patterns of D5 (Fig. 51, left side, top) confirms the coexistence of TiB_2 and TiN. An intensive hexagonal (100) reflection of TiB_2 is obtained (correlating to a pronounced (001) texture of D5) and also weak cubic reflections of TiN are visible.

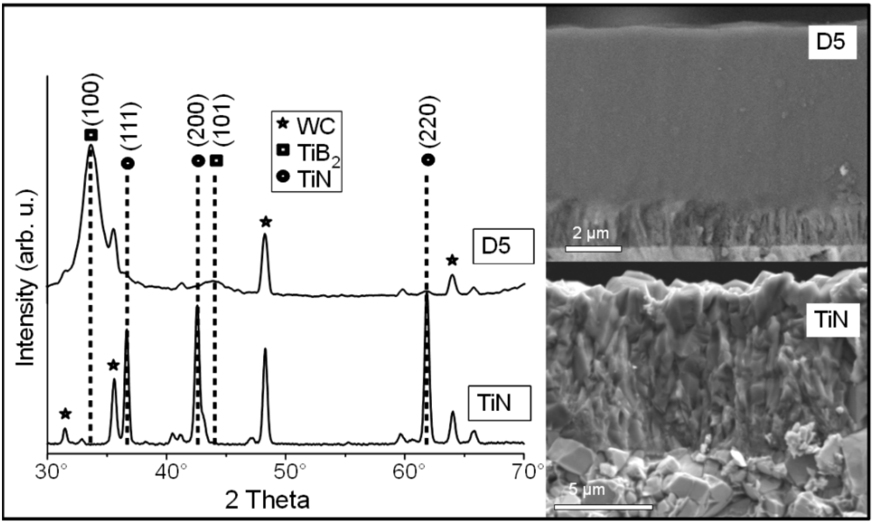

Fig. 51: left side - XRD patterns of the investigated TiN and D5 coating (top). ■ indicates the reflections of the hexagonal phase, ● reflections of the cubic phase, and ★ denotes WC, right side - SEM images (secondary-electron contrast mode, WD = 7 mm, EHT = 10 kV) showing the fracture morphology of TiN and D5.

Direct comparison of the SEM images of D5 and the TiN coatings (Fig. 51, right side) indicates much finer grains for D5. Furthermore, the addition of boron increases the hardness from HV 1890 for TiN to HV 4360 in D5 (see appendix Table 16, p. 135). In contrast to TiN, for which the hardness typically decreases at elevated temperatures due to a reduction in defect density, it is known that Ti-B-N coatings exhibit thermally induced self-hardening. Hardness values of Ti-B-N coatings are reported to increase up to T = 800°C (17; 33; 120; 148).

4.5.2 Tribological behavior against Al_2O_3

Friction coefficients and wear behavior

Measured friction coefficients μ (mean value from 3 measurements) of Al_2O_3 balls sliding on TiN and D5 coatings at ambient and elevated temperature are shown in Fig. 52. The μ values were obtained after LTS when running-in had occurred in all cases except for the measurement of the TiN coating at 700°C. In this case, the coating had been worn through and friction coefficients were measured after 40 m before the coating was used up. Two exemplary friction curves of D5 coatings against Al_2O_3 at r.t. can be found in the appendix (Fig. 60, p.137).

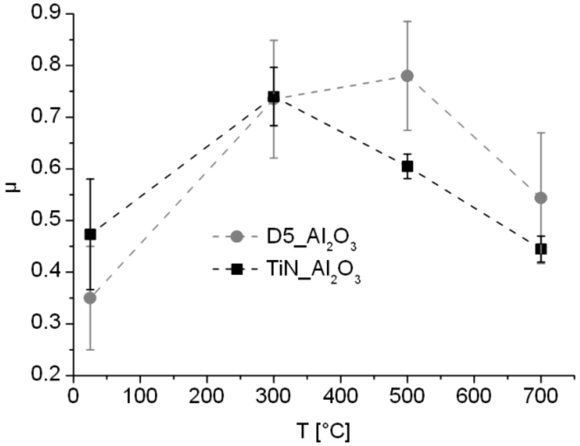

Fig. 52: Friction coefficients (mean value from 3 measurements, error bars give standard deviation) of Ti-B-N coatings D5 and TiN against Al_2O_3 (L = 300 m, F_N = 7 N, v = 7.5 cm/s, r = 3 mm).

The friction values of coating D5 against Al_2O_3 correspond well with previously published results obtained on CVD Ti-B-N coatings with high boron concentrations (20). The lowest μ value (μ = 0.35) is obtained at room temperature. It increases up to 500°C (μ = 0.82). However, at 700°C the friction coefficient dramatically decreases to a value again closer to that at room temperature (μ = 0.5). For TiN the friction coefficient at first shows an increase from μ = 0.59 at r.t. to μ = 0.72 at 300°C, whereas at higher temperatures it decreases (μ = 0.44 at 700°C).

Both optical micrographs and SEM images of the wear tracks were recorded to obtain information on the dominating wear mechanism. Some exemplary optical microscope images of D5 (left side) and TiN (right side) coatings after sliding against Al_2O_3 at r. t., 300, 500 and 700°C are summarized in Fig. 53. Calottes on the wear tracks (similar drill depths) are made to show the influence of ball-on-disk sliding tests on the coating thickness (abrasive/adhesive wear) as well as the oxide layer thickness at elevated temperatures.

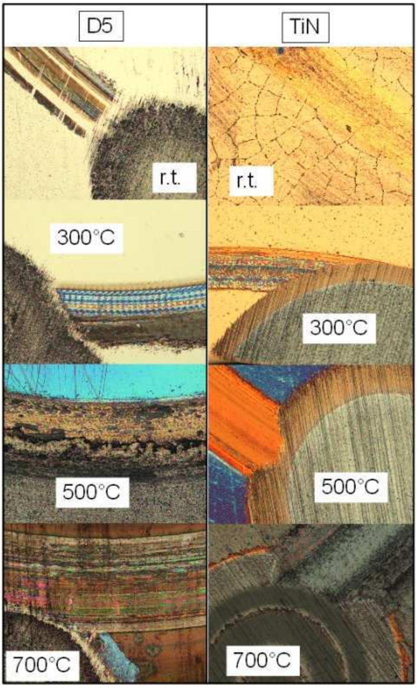

Fig. 53: Optical micrographs of the wear tracks after ball-on-disk sliding tests of D5 and TiN against Al_2O_3 at r. t., 300, 500 and 700°C (L = 300 m, F_N = 7 N, v = 7.5 cm/s, r = 3 mm). Calottes on the wear tracks show the influence of ball-on-disk sliding tests on the coating thickness (abrasive/adhesive wear).

At all examined temperatures, no adhesive wear occurred after sliding Al_2O_3 on TiN and D5 coatings most likely due to the hardness and inertness of the counterpart (20). For TiN coatings, the observed wear mechanism was mildly abrasive wear at r.t. and 300°C (Fig. 53 - right side, top) and severely abrasive wear at higher temperatures (Fig. 53 – right side, bottom). At 700°C the TiN coatings were worn through.

The optical micrographs of the wear tracks of coating D5 (Fig. 53, left side) show most notably differently colored areas. These may be explained as resulting from interference effects at transparent oxide layers, and therefore indicate substantial oxidation (94). Thus, it can be assumed that the dominant wear mechanism of Ti-B-N against Al_2O_3 is tribochemical oxidation.

Raman analysis of the wear tracks and correlation to the observed friction coefficients

Since all coatings were polished to possess a comparable roughness prior to testing, the observed trends of friction coefficients with temperature are assumed to primarily correspond to the nature of the formed oxides after ball-on-disk testing as well as to the different hardness values of TiN (1890 HV) and D5 coatings (4360 HV). The absence of adherent material from the ball as well as the transparency of Al_2O_3 permitted to identify different titanium compounds by Raman spectroscopy on the wear tracks (Table 11). Note that the compounds identified by Raman spectroscopy for TiN at 700°C are from measurement points located on the wear track where the coatings was not yet worn through.

In Fig. 54 exemplary Raman spectra taken on the wear tracks after sliding D5 and TiN coatings against Al_2O_3 are shown and correlated to the observed friction coefficients. Interestingly, after sliding at room temperature, rutile (indicated by □ in Fig. 54) could already be detected by Raman spectroscopy in the middle of the wear track of D5, most likely formed through tribochemical oxidation. Obviously, the flash temperature in the contact zone during sliding must have reached values of $T \geq 600°C$, the temperature where rutile has been reported to be the stable TiO_2 modification (20). This observation may be explained by the high hardness values of both parts of the tribocouple.

Table 11: Compounds identified on the wear track by Raman spectroscopy after LTS testing D5 and TiN coatings against Al_2O_3.

Coating	**Counterpart**	**Temperature [°C]**			
		25	300	500	700
TiN	Al_2O_3	TiN	TiN, carbon	anatase, rutile	rutile, anatase
D5	Al_2O_3	Ti-B-N, rutile	Ti-B-N, carbon	Ti-B-N, anatase	rutile, anatase

On the other hand the spectra taken on the wear track of TiN were similar to those measured for the as-deposited TiN surface (compare Fig. 54 with Fig. 17, page 54). This may correlate to the lower hardness values of TiN compared to D5 (1890 HV compared to 4360 HV) resulting in lower contact temperatures during sliding.

The formation of a lubricious oxide transfer layer of rutile in the presence of environmental humidity has been frequently reported (94; 135; 134; 149; 150). Here, this could not be observed for TiN but for Ti-B-N and may therefore explain the lower friction coefficient of D5 compared to TiN at r. t. (see Fig. 54).

After sliding at 300°C the Raman spectra of both coatings showed two intense bands at 1375 and 1595 cm^{-1}. These bands can be attributed to the D- and G- band characteristic for carbon, most likely due to C-adsorption at this temperature (94) as well as C-contaminations of the Al_2O_3 balls found by EDX (see appendix Fig. 61, p. 138). This observation likely explains the similar friction coefficient of both coatings at 300°C (see Fig. 54).

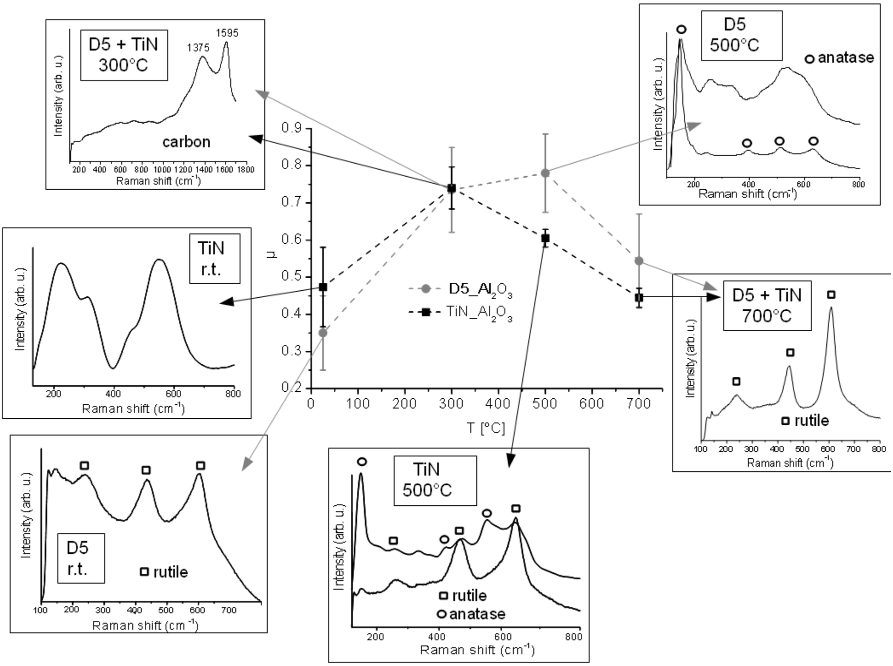

Fig. 54: Correlation between Raman results and friction coefficients. Raman spectra were taken on the wear track of D5 and TiN coatings after sliding against Al_2O_3 balls at r.t, 300, 500 and 700°C (L = 300 m, F_N = 7 N, v = 7.5 cm/s, r = 3 mm).

The wear tracks after ball-on-disk testing at 500°C show different oxidation products for TiN and D5 coatings. For D5, the center of the wear track can be well characterized by a mixture of the un-oxidized sample and anatase (indicated by ○ in Fig. 54), whereat the initial oxidation to anatase is indicated by a sharp and intense peak at 143 cm^{-1}. In addition, at the border zones of the wear track, the Raman spectra already correlate to full oxidation to anatase, where all characteristic peaks can be identified.

For TiN in contrast, the Raman spectra taken on marginal positions of the wear tracks already exhibit a mixture of anatase and rutile. Furthermore, in the center on the wear track full oxidation to rutile is observed.

By comparison with the above described results on TiN and D5 coatings after static oxidation at 500°C (see Chapter 4.3.3) the observed differences may be explained as follows: after heating up to 500°C (about 30 min) the surface of the D5 coating is most likely oxidized to anatase. Thus, the sliding tribocouple is anatase against Al_2O_3, where the oxide layer is protecting the underlying coating during sliding (20; 151). However, due to the large differences in molar volume between anatase and the coating, formation of compressive stresses may lead to oxide spallation (20; 152; 153). As a result of this effect, at some measurement points in the center on the wear track, where the oxide layer is spalled off, also the spectrum of the un-oxidized D5 coating can be detected by Raman spectroscopy. In addition, such oxide spallation is supposed to lead to rough surfaces, and therefore higher friction values (20; 152; 153). This can be seen in Fig. 54.

In contrast, the oxidation behavior of the TiN coatings reveal that after static oxidation at 500°C only beginning oxidation of TiN to anatase is observed (Chapter 4.3.1). It can thus be assumed that no protective oxide layer is formed during heating up. Consequently severe abrasive wear occurs during sliding, due to the decreasing hardness of TiN with increasing temperature (see Fig. 53). This severe abrasive wear further seems to lead to higher flash temperatures in the contact zone, and as a result the TiN coating oxidizes to rutile due to tribooxidation. This observation was found here by Raman spectroscopy and further correlates well with literature data (20). As mentioned above, rutile is said to lower friction by acting as a solid lubricant, whereas anatase is assumed to increase friction due to oxide spallation. Thus, the differences in the formed oxides may be the reason for the lower friction coefficient of TiN compared to D5 at 500°C (Fig. 54).

Raman spectra measured on the wear tracks after sliding at 700°C show that both coatings favor the formation of stable rutile. Thus the friction coefficients of TiN and D5 are assumed to decrease at this temperature, which is demonstrated by the µ values in Fig. 54.

4.5.3 Tribological behavior against 100Cr6

Friction coefficients and wear behavior

In addition to the sliding tests using Al_2O_3, similar experiments as described above were carried out on TiN and Ti-B-N coating D5 with balls of 100Cr6 bearing steel as counterpart. Steady-state friction coefficients obtained after LTS testing are shown in Fig. 55. Similar to experiments described in Chapter 4.5.2, the TiN coating at 700°C had been worn through after a sliding distance of 300 m, and friction coefficients were measured after 40 m.

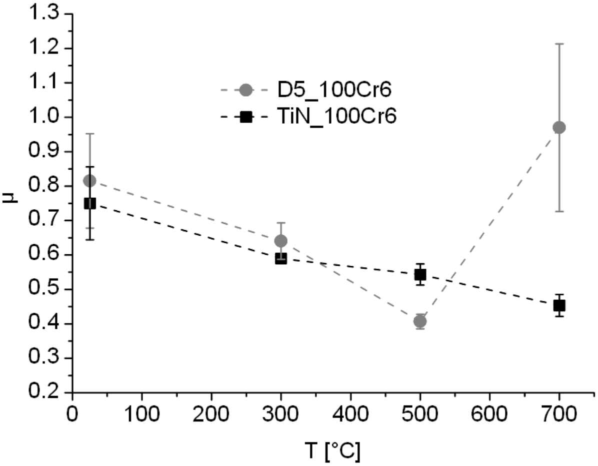

Fig. 55: Friction coefficients (mean value from 3 measurements, error bars give standard deviation) of Ti-B-N coatings D5 and TiN against 100Cr6 (L = 300 m, F_N = 7 N, v = 7.5 cm/s, r = 3 mm).

At room temperature, the friction coefficient for TiN (μ = 0.79) is in good agreement with previously published results were μ was reported to be 0.8 (94). However, with increasing temperature the friction values continuously decrease to μ = 0.5 at 700°C.

For D5 the friction coefficient at room temperature (μ = 0.82) correlates well with values reported in earlier studies on PACVD Ti-B-N coatings $^{(18)}$. Furthermore, at r. t. and 300 °C (μ = 0.62) it is quite similar to that of TiN. But in contrast to TiN, μ decreases much stronger for D5 at 500°C (μ = 0.4) and considerably increases again at 700°C (μ = 0.93).

Optical micrographs and SEM images (secondary-electron contrast mode) in Fig. 56 indicate that the dominant wear mechanism for TiN against 100Cr6 is primarily transfer of ball material to the coating at r. t. and 300°C (see Fig. 56, right side). At higher temperatures, the wear mechanism changes to abrasive wear, and at 700°C the coating was worn through.

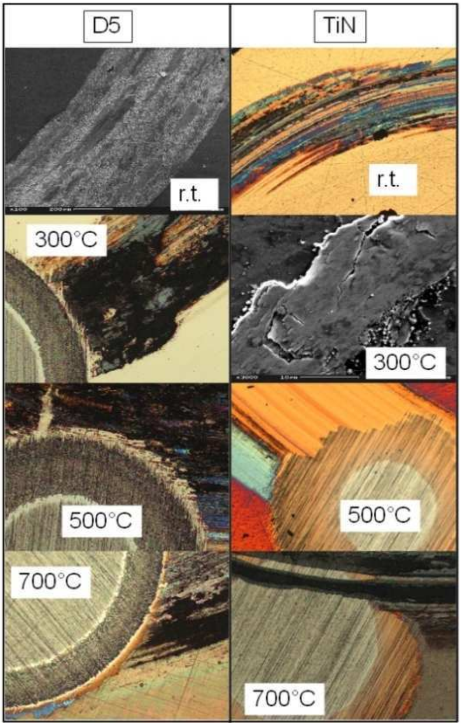

Fig. 56: Optical micrographs and SEM images of the wear tracks after ball-on-disk sliding tests of D5 and TiN coatings against 100Cr6 at r. t., 300, 500 and 700°C (L = 300 m, F_N = 7 N, v = 7.5 cm/s, r = 3 mm). Calottes on the wear tracks show the influence of ball-on-disk sliding tests on the coating thickness (abrasive/adhesive wear).

Similar to TiN, coating D5 shows adhesion of ball material after sliding (Fig. 56, left side). But in contrast to TiN, this effect is found for all examined temperatures. At 700°C, the coating was not worn through, but severely oxidized. The evidently different wear mechanism active for TiN and D5 at $T \geq 500°C$ may be related to the varying hardness values of these two coatings at elevated temperatures (see Chapter 4.5.1).

Raman analysis of the wear tracks

The compounds identified by Raman spectroscopy on the wear tracks after LTS against 100Cr6 bearing steel are listed in Table 12.

Table 12: Compounds identified on the wear track by Raman spectroscopy after LTS testing D5 and TiN coatings against 100Cr6.

Coating	**Counterpart**	**Temperature [°C]**			
		25	300	500	700
TiN	100Cr6	Fe, Fe_3O_4, Fe_2O_3	Fe_3O_4, Fe_2O_3	Fe_2O_3, anatase, rutile	Fe_2O_3, rutile, anatase
D5	100Cr6	Fe, Fe_3O_4, Fe_2O_3	Fe_3O_4, Fe_2O_3	Fe_2O_3	Fe_2O_3

Obviously it was not possible to detect any of the formed titanium compounds at the interface of the wear track by Raman spectroscopy due to the large amount of transferred material from the 100Cr6 ball. However, at 500°C and 700°C the wear mechanism of TiN changed to abrasive wear (see Fig. 56) and here the same titanium oxides were found as after sliding against Al_2O_3. This is also indicated by the similar friction coefficients of TiN against 100Cr6 and Al_2O_3 at these two temperatures. For all other sliding tests, typical spectra obtained from the wear tracks (Fig. 57) only exhibit different iron oxides like

Fe_3O_4 (222, 242, 289, 410, 498, 610, 658, 1318 cm^{-1}) and Fe_2O_3 (309, 541, 669 cm^{-1}) (142; 143). Thus, a correlation of the Raman results with the observed friction coefficients was not possible in this case.

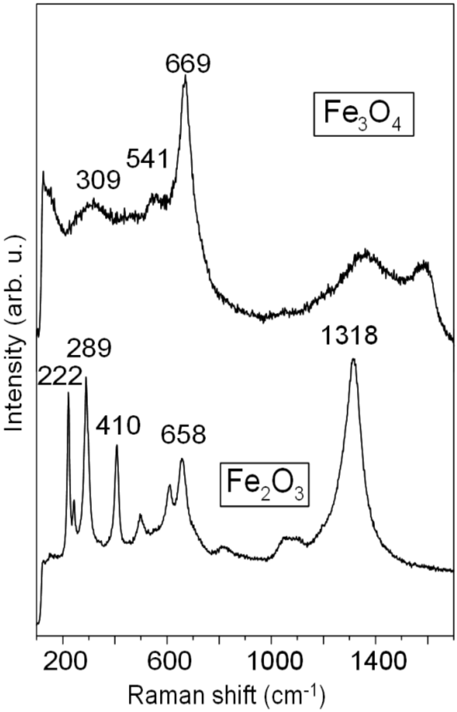

Fig. 57: Exemplary Raman spectra demonstrating the formation of different iron oxides on the wear tracks after LTS testing D5 and TiN against 100Cr6 (L = 300 m, F_N = 7 N, v = 7.5 cm/s, r = 3 mm).

4.5.4 Temperature dependent chemical reactions at the interface (coating – ball)

Considering that adhesive wear is the dominant mechanism in the above described material pairing (coating – 100Cr6 ball), it was expected that a comparatively thin transfer layer should be formed when sliding an exceptionally short distance. Tribochemical reaction products at the interface between the coating and the counter material may thus be detectable by Raman spectroscopy and a correlation of the results to the friction coefficients may be possible.

For that reason, a complementary set of ball-on-disk tests was performed with sliding distances of only 0.3 m (= STS) at room temperature. For a better comparison with the LTS tests at high temperatures, the samples were post-annealed at 300, 500 and 700°C for 0.5, 1 and 3 h. In this way influences of frictional heating, heat-up and cooling down phases as well as temperature gradients across the insert (the thermocouple was placed below the coated insert, the temperature drop to the upper surface may be roughly estimated to 100 °C) are avoided, and the temperature dependence of chemical reactions at the interfaces can be studied more precisely.

Since in this work the tribological behavior of Ti-B-N coatings was of interest, the STS post-annealing experiments were only performed with D5 and not with TiN coatings. However, for a better comparison, not only 100Cr6 was used as counter material, but also Al_2O_3.

Raman analysis of the wear tracks and correlation to the observed friction coefficients

The compounds found by Raman spectroscopy on the wear tracks of the post-annealed D5 samples after STS testing against Al_2O_3 and 100Cr6 are summarized in Table 13.

As a matter of fact, the usage of shorter sliding distances enabled the detection of different titanium compounds in the contact zone of the 100Cr6-tested samples. With longer annealing times and higher annealing temperatures the wear tracks on the samples were found to oxidize to a higher extent and the amount of the thermodynamically stable oxides (rutile and Fe_2O_3) obviously increases. Furthermore, the titanium and iron compounds identified on the post-annealed STS samples are in good agreement with the results after LTS testing at high temperatures (compare Table 13 with Tables 11 and 12).

Table 13: Compounds identified by Raman spectroscopy on the wear tracks after post-annealing STS-tested Ti-B-N coatings (D5) against Al_2O_3 and 100Cr6.

		Duration of post-annealing [h]		
T [°C]	**Counterpart**	**0.5**	**1**	**3**
25	Al_2O_3	Ti-B-N	Ti-B-N	Ti-B-N
300		Ti-B-N	Ti-B-N + anatase	anatase
500		Ti-B-N + anatase	anatase	anatase + rutile
700		rutile + anatase + $\mathbf{H_3BO_3}$	rutile + anatase + $\mathbf{H_3BO_3}$ + $\mathbf{B_2O_3}$	rutile + $\mathbf{H_3BO_3}$
25	100Cr6	Ti-B-N / Fe	Ti-B-N / Fe	Ti-B-N / Fe
300		Ti-B-N / Fe_3O_4	Ti-B-N + anatase / Fe_3O_4 + Fe_2O_3	anatase / Fe_2O_3
500		Ti-B-N + anatase + $\mathbf{H_3BO_3}$ / Fe_2O_3	anatase + $\mathbf{H_3BO_3}$ / Fe_2O_3	anatase + rutile / Fe_2O_3
700		rutile + anatase, + $\mathbf{H_3BO_3}$ + $\mathbf{B_2O_3}$ / Fe_2O_3	rutile + anatase + $\mathbf{H_3BO_3}$ + $\mathbf{B_2O_3}$ / Fe_2O_3	rutile / Fe_2O_3 + $\mathbf{FeBO_3}$

Although the titanium compounds found on the STS-tested samples correlate very well for 100Cr6 and Al_2O_3, significant differences can be found regarding the formed boron oxides.

In the case of Al_2O_3, boric acid H_3BO_3 (209, 499, 880, 1166 cm^{-1}) and traces of boron oxide B_2O_3 (500, 732, 801, 1260 cm^{-1}) could be detected at $T_a \geq 700$°C. Fig. 58 (right side, bottom) shows the Raman spectrum taken on the wear track of a coating D5 after STS and post-annealing at 700°C for 1h. For better comparison, the spectra of anatase, rutile, boron oxide and boric acid are added in grey. All the characteristic Raman shifts of the latter species can be found in the spectra of D5 (Fig. 58, right side, bottom, black line).

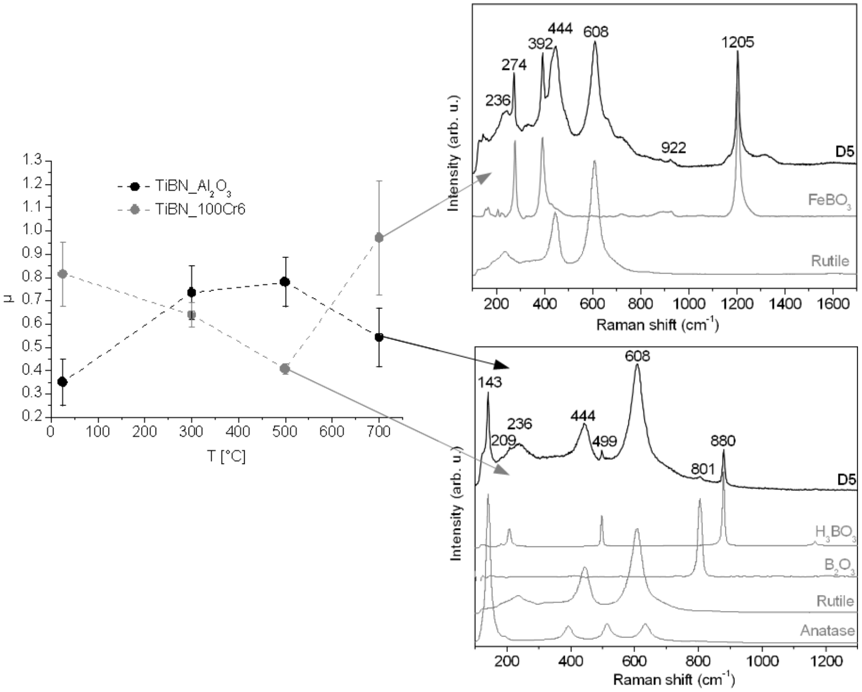

Fig. 58: Correlation between Raman results and friction coefficients. Raman spectra were taken on the wear tracks of D5 coatings after ball-on-disk testing against Al_2O_3 and 100Cr (L = 0.3 m, F_N = 7 N, v = 7.5 cm/s, r = 3 mm) at r.t. and post-annealing at different temperatures and durations. Raman spectra of reference samples (anatase, rutile, B_2O_3, H_3BO_3 and $FeBO_3$) are added for comparison (grey lines).

As already mentioned before, boric acid is well known to act as a self-lubricant (95; 97; 98; 99), and thus it most likely contributes to the lower friction coefficient of D5 at 700°C compared to 500°C as well as compared to TiN (see Fig. 58, left side).

However, H_3BO_3 could not be detected in the wear track after LTS testing against Al_2O_3 at 700°C (see Table 11). This may be explained by the enhanced mechanical stresses in the latter case which result in an easier release of the boron atoms from the coating as well as in an increased flash temperature at the contact zone. Boric acid has been reported to evaporate at $T \geq 900°C$ (33). Therefore, after LTS (300 m sliding takes 1.1 h), it can be assumed that a loss of boron had occurred due to evaporation of this volatile species.

In contrast to the STS tests against Al_2O_3, with 100Cr6 as counterpart boric acid H_3BO_3 and boron oxide B_2O_3 could already be detected at $T_a \geq 500°C$. This result may be explained by two effects: (i) Although the thermal formation of B_2O_3 is said to occur at 600°C, the oxidation of TiB_2 can even be initiated at much lower temperatures due to the tribomechanical stress conditions prevailing at the fretting contact as reported in the literature (150; 154). (ii) Boron atoms easily diffuse into ferrous alloys because of their relatively small size and very mobile nature. They can dissolve in iron interstitially and readily react with ambient oxygen and moisture to form H_3BO_3 (131). The high solubility of boron in ferrous alloys may thus be the reason why boron oxide and boric acid could already be found at 500°C after STS against 100Cr6, whereas after sliding against Al_2O_3 both compounds could not be detected until 700°C are reached. Furthermore, here again the appearance of boric acid seems to be strongly connected to the very low friction coefficient of D5 against 100Cr6 at 500°C (Fig. 58, left side).

It is known, that boron - after dissolving in iron and forming H_3BO_3 - can react in a subsequent step with iron oxides to form $FeBO_3$ (155). And indeed, after prolonged annealing of the 100Cr6-STS-tested D5 samples at 700°C the formed boron oxides seem to undergo such reaction. In Fig. 58 (right side, top) the spectrum taken on the wear track after annealing at 700°C for 3 h is shown (black line). By comparison with reference measurements of $FeBO_3$ (grey line) and literature data (156), the sharp peaks located at 274, 392, 922 and 1205 cm^{-1} can be clearly assigned to iron borate. Furthermore, signals of rutile (reference spectrum is also added in grey) can be found.

The strong re-increase of friction of the coatings D5 after sliding against 100Cr6 at 700°C (see Fig. 58, left side) may therefore be explained by the formation of $FeBO_3$ found in these STS tests after prolonged annealing at 700°C. At this temperature, the entire H_3BO_3 - formed at 500°C in the contact zone - is assumed to react with the iron oxides from the transfer layer. As a result, it can no longer act as a self-lubricant, and consequently friction increases.

In conclusion, the usage of a shorter sliding distance and post-annealing the samples at different conditions seems to be a suitable technique to study the temperature dependence of tribochemical reactions at the interface coating – ball. Although dissimilarities were obtained for D5 coatings at r.t. and 700°C after LTS and STS testing against Al_2O_3 (most likely due to higher flash temperatures in the first case) both results provide support for the observed friction coefficients.

4.5.5 Turning of 100Cr6 with Ti-B-N coated inserts

In addition to the ball-on-disk tests, turning test with D5-coated inserts were performed at different turning speeds. Fig. 59 includes SEM images (secondary-electron contrast mode) showing the inserts after turning 100Cr6 steel. The dominant wear mechanism in the tests was crater wear, and the crater width increasing with cutting speed. Raman spectra were recorded at different positions on the rake face to characterize the coating and adherent work piece material. The identified compounds are summarized in Table 14. Note, that the considerable amounts of carbon detected on the inserts may result from the work piece material (1 wt% C, see appendix Table 17, p. 138) since no lubricant was used.

In order to estimate an approximated value for the contact temperatures during machining operations, the detected phases of the inserts from the turning tests were correlated with the results of the LTS and STS tests.

Table 14: Phases identified by Raman spectroscopy on inserts from turning tests (summary of measurements at different positions on the rake face).

v_c [m/min]		
150	180	200
Ti-B-N anatase (*small amount*) Fe_3O_4 Fe_2O_3 carbon	Ti-B-N anatase Fe_3O_4 Fe_2O_3 carbon	Ti-B-N anatase rutile Fe_3O_4 Fe_2O_3 $TiBO_3$ carbon (*small amount*)

Within the cutting time of 3 min, only slight oxidation of the coating (Ti-B-N and anatase) was found at moderate cutting speeds of v_c = 150 m/min and v_c = 180 m/min. Comparison of the detected phases with the results given in Tables 11-13 suggests that the contact temperature on the rake face did not exceed 500 °C in these two cases.

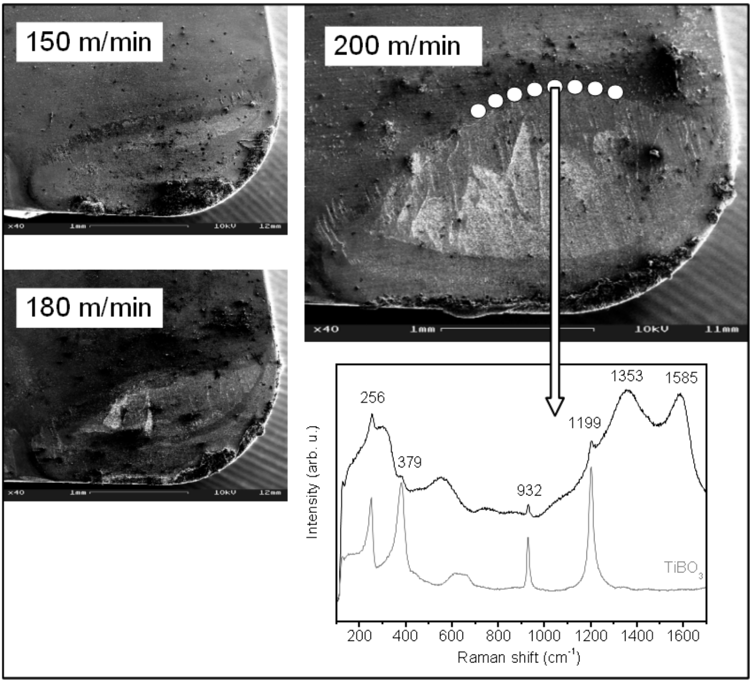

Fig. 59: SEM images (secondary-electron contrast) of D5-coated inserts from turning tests after 3 min cutting time at different turning speeds (left side and top). Resulting Raman spectrum (right bottom) of the cutting insert at v_c = 200 m/min (points of measurement are marked with white dots) compared to $TiBO_3$ (grey line).

On the other hand, at a cutting speed of v_c = 200 m/min, several measurement spots showed full oxidation of the coating to rutile, and also the borate spectrum shown in Fig. 59 was found (points of measurement are marked in the SEM image). At first sight, the spectrum looks similar to the iron borate spectrum found on the post-annealed (3h, 700°C) STS-tested coating D5 (Fig. 58, right side, top). A closer look at the peak positions, however, reveals differences. In particular, the first two peaks are shifted about 15 cm^{-1} toward lower wavenumbers. By comparison with literature data (157) and reference measurements, it was found that the peak positions (256, 379, 932, 1199 cm^{-1}) may rather be attributed to $TiBO_3$ than $FeBO_3$. The formation of $TiBO_3$ has been reported at 785 °C from TiO_2 and amorphous boron (158) as well as at 900°C from TiB_2 and O_2 (159). The annealing experiments in this work, on the other hand, demonstrated that $FeBO_3$ is only formed after prolonged heating to 700 °C. In conclusion, the increased cutting speed of $v_c = 200$ m/min generated highest contact temperatures on the rake face of the coating D5 at the inner edge of the crater (marked in Fig. 59). Furthermore, it can be assumed that the temperature in this region reaches values of at least $T \geq 785$ °C, which would be in good accordance with literature data (160; 161; 162).

4.5.6 Summary

Tribological wear tracks formed on MTCVD Ti-B-N coating D5 and TiN during ball-on-disk testing against Al_2O_3 as well as 100Cr6 were successfully characterized by means of Raman spectroscopy.

Different oxide and borate phases resulting from tribochemical reactions and tribooxidation could clearly be identified. It was shown, that the temperature dependence of tribological reactions at the interface can be successfully studied by combining exceptional short sliding distances and post-annealing of the samples at different temperatures and durations. A good correlation between the detected compounds and the observed friction coefficient was achieved.

Different oxide phases identified by Raman spectroscopy on the rake faces of inserts used in turning tests allowed an estimation of contact temperatures and wear behavior. It was found, that the temperature of the inserts is highly affected by the cutting speed. The temperature is assumed to reach values of $T \geq 785$ °C at increased cutting speeds of $v_c = 200$ m/min, especially supported the detection of $TiBO_3$.

A strong local diversity of composition was found on the wear tracks and rake faces, which may reflect local variations of the flash temperature during sliding and turning. A mapping of larger sample areas using Raman microspectroscopy is possible and may be used in future works as a powerful alternative technique to estimate temperatures generated during machining. In the sight of the present results, it should be possible to obtain a fingerprint of local heating which occurs on an insert during cutting.

5. Conclusion

$TiC_{1-x}N_x$, $TiB_xC_yN_z$ and Ti-B-N coatings prepared by HT- and MT-LPCVD were characterized using Raman spectroscopy, WDS, XRD, SEM and XPS. The results of the different analysis methods were compared and correlated. It was shown that first-order, defect-induced Raman spectra of good quality can be obtained from all the coatings, even if buried within a multilayer stack (like the $TiB_xC_yN_z$ coatings).

For $TiC_{1-x}N_x$ and $TiB_xC_yN_z$ coatings, it was found that even small changes in the C:N ratio result in systematical shifts of the Raman peaks. With increasing nitrogen concentration, the acoustical phonons shift to lower frequencies highly correlating to a decreasing lattice constant as derived from XRD measurements. The sensitivity of the TA-mode shifts to changes in the lattice constant and composition of the investigated samples was found to be largest for N-rich coatings. Looking at all investigated $TiC_{1-x}N_x$ and $TiB_xC_yN_z$ coatings, the dependence of the Raman shifts is slightly nonlinear. Nevertheless, Raman spectroscopy may be used to estimate locally compositions and lattice constants for such coatings due to the high spatial resolution. In addition to the band shifting, the intensity and FWHM of the Raman modes was found to change during the transforamtion from carbon- to nitrogen rich coatings. Furthermore, in the optical range a well-defined change in the spectral shape of the Raman modes is obtained when the nitrogen or carbon concentration in the coatings exceeds at least 30 at.%. This suggests that the appearance of this region may serve as a fingerprint to discriminate between C- and N-rich coatings.

For Ti-B-N coatings with different boron concentrations a good correlation between WDS, XRD, XPS and Raman spectroscopy was found. Despite the different information depths and information contents, the same transition trends were observed in the progression from TiN to TiB_2 by the addition of boron. At boron concentrations ≥ 18 at.%, the coatings were found by XRD and XPS to consist of two phases, namely TiN and TiB_2. On the other hand, the high sensitivity of Raman spectroscopy to small composition changes in the investigated material system enabled the clear identification of TiB in the Ti-B-N coatings with low boron concentrations ($B \leq 18$ at %). In these boron-poor coatings XRD could not detect any boron-containing phase, whereas XPS only indicated one by an undefined, weak signal in the spectra. For the examined Ti-B-N samples with varying boron concentrations, it was therefore found that only the combination of WDS, XRD, XPS and Raman spectroscopy allows a precise characterization of the different existing phases in coatings.

The oxidation behavior of TiC, TiN, $TiC_{1-x}N_x$, $TiB_xC_yN_z$ and Ti-B-N coatings was studied in this work. Therefore the coatings were annealed for 1h at 500 and 700°C under ambient conditions. The oxidation products were inspected by Raman spectroscopy, GIXRD and WDS. Oxidation products like anatase, rutile and different boron oxides could easily be distinguished by Raman spectroscopy. The oxidation depth and the oxide layer composition correlates well with the results obtained by WDS and GIXRD.

The degree of oxidation is largely dependent on the coating composition (C:N ratio as well as boron concentration). In $TiC_{1-x}N_x$ and $TiB_xC_yN_z$ coatings the extent of static oxidation at 500°C can be explained by decreasing oxidation resistance with increasing carbon concentration. Kinetic effects retard the further oxidation at 700°C, therefore a higher relative anatase concentration is observed in carbon-rich coatings. Direct comparison of $TiC_{1-x}N_x$ with $TiB_xC_yN_z$ coatings shows a higher degree of oxidation with increasing boron concentration as well as an evolution of boron oxides.

The oxidation behavior of Ti-B-N coatings is significantly affected by the boron concentration. The thermal stability against oxidation is improved at low boron-concentrations ($B \leq 18$ at %) compared to TiN at annealing temperatures up to 700°C. This behavior most likely correlates to the TiB phase in these coatings. This compound obviously enhances the oxidation resistance and decreases the thickness of the oxidation layer. After being annealed at 500°C, coatings with a high boron concentration show a higher degree of oxidation compared to TiN. However, at $T_a > 600$°C, these coatings form boron oxides on their surface. B_2O_3 exhibits protective qualities and leads to the formation of metastable anatase rather than the thermodynamic stable rutile.

Furthermore, tribological wear tracks formed on Ti-B-N and TiN coatings during ball-on-disk testing against Al_2O_3 as well as 100Cr6 were characterized by means of Raman spectroscopy. Different oxide and borate phases resulting from tribochemical reactions and tribooxidation could clearly be identified. It could be shown, that the temperature dependence of tribological reactions at the interface can be successfully studied by combining exceptional short sliding distances and post-annealing of the samples at different temperatures and durations. A good correlation between the detected compounds and the observed friction coefficient was achieved.

Different oxide phases identified by Raman spectroscopy on the rake faces of inserts used in turning tests, allowed an estimation of contact temperatures and wear behavior. The local heating of the inserts seems highly affected by the cutting speed. Therefore, the contact temperature is assumed to reach values of $T \geq 785$ °C at increased cutting speeds of $v_c = 200$ m/min, especially supported by the detection of $TiBO_3$.

In conclusion, the results of this work may clearly contribute to establish Raman spectroscopy as complementary technique compared to XRD, SEM, WDX or XPS for the characterization of titanium-based CVD coatings. Analysis of the composition, oxidation and tribological behavior can be studied less time consuming (in most cases measurement under ambient conditions is possible, minimal effort on sample preparation) and with a very high spatial resolution. Raman spectroscopy is thus a method with great potential for the investigation and development of ceramics and in particular CVD coatings.

Appendix

Table 15: Properties of TiC, TiN and TiB_2. Values are taken from [(62)] and references therein.

Coating	Crystal structure	Lattice parameter [nm]	ρ [g/cm^3]	m.p. [°C]	Linear thermal Expansion [10^{-6} K^{-1}]	Thermal conductivity [W m^{-1} K^{-1}]	Electrical resistivity [10^{-6} Ωcm]	Enthalpy [kJ mol^{-1}]	Young Modulus [10^5 N mm^{-2}]	Micro-hardness [10Nmm^{-2}]	Ox. resistance [100°C]
TiC	fcc	0.429-0.433	4.91-4.94	3060-3180	7.4-8.74	17.17-33	45-68.2	183.8-239.7	2.59-5	2094-3200 HV	11-14
TiN	fcc	0.42-0.425	4.73-5.43	2949-3220	8.3-9.4	19.26-38	17-30	303.1-338.1	2.5-6	1800-2450 HV	11-14
TiB_2	hex	0.3-0.303034/0.32-0.322953	4.38-4.5	2900-3230	6.39-8	25.96-27	7-9	150.7-324.1	3.7-5.7	2500-2480 HV	11-13

Table 16: Deposition parameters, coating thicknesses and hardness values of the examined coatings.

Sample **HT-TiC$_{1-x}$N$_x$**	N$_2$:CH$_4$	T [°C]	p [mbar]	Hardness [HV]	Thickness (TiN-TiCN) [µm]
A5	0.25	1015	300	2694	0.3 – 9.6
A4	1	1015	300	2579	0.7 – 9.2
A3	3.5	1015	300	2116	0.5 – 8
A2	9	1015	300	2174	0.5 – 6.3
A1	18	1015	300	2022	0.5 – 4.8

Sample **HT-TiB$_y$C$_y$N$_z$**	N$_2$:CH$_4$	BCl$_3$ [sccm]	T [°C]	p [mbar]	Hardness [HV]	Thickness (TiN-TiBCN-TiBN) [µm]
B5	0.25	60	1015	300	3124	0.5 – 9.4 – 1.1
B4	1	60	1015	300	2722	0.6 – 3.4 – 1.2
B3	3.5	60	1015	300	2581	0.4 – 3.5 – 1.6
B2	9	60	1015	300	2538	0.7 – 5.3 – 1.3
B1	18	60	1015	300	2334	0.5 – 5.4 – 1.5

Sample **HT-TiB$_y$C$_y$N$_z$**	N$_2$:CH$_4$	BCl$_3$ [sccm]	T [°C]	p [mbar]	Hardness [HV]	Thickness (TiN-TiBCN-TiBN) [µm]
A1	18	0	1015	300	2022	0.5 – 4.8 - 0
C2	18	30	1015	300	-	nm – 8.1 – 1.2
C3	18	60	1015	300	2334	0.5 – 5.4 – 1.5
C4	18	120	1015	300	2415	nm – 3.8 – 1.2
C5	18	240	1015	300	2514	0.4 – 5.3 – 1.5

Note: Samples C1 and C3 are the same samples as A1 and B1, respectively.

Continuation of Table 16:

Sample **MT-$TiB_yC_yN_z$**	$TiCl_4$:CH_3CN	BCl_3 [sccm]	T [°C]	p [mbar]	Hardness [HV]	Thickness (TiN-TiBCN-TiBN) [µm]
c1	8.5	20	900	90	3371	0.3 – 5.5
c2	8.5	30	900	90	3500	0.3 – 6.9 – 0.6
c3	8.5	60	900	90	3400	0.3 – 5.9 – 0.5
c4	8.5	120	900	90	3310	nm – 5.4
c5	8.5	240	900	90	3500	0.7 – 6.1

Sample **Ti-B-N**	$TiCl_4$ [ml/min]	N_2 [l/min]	BCl_3 [sccm]	T [°C]	p [mbar]	Hardness [HV]	Thickness (TiN-TiBN) [µm]
D1	2	6	30	850	900	3490	0.7 – 3.7
D2	2	6	60	850	900	3815	0.8 – 4.5
D3	2	6	120	850	900	-	0.3 – 4.8
D4	2	6	240	850	900	3960	0.8 – 5.2
D5	2	6	480	850	900	4360	0.9 – 6.5

Sample	Flow rates	T [°C]	p [mbar]	Hardness [HV]	Thickness [µm]
TiC	$TiCl_4$:CH_4 = 1.4	1010	100	2935	TiN: 1.2 - TiC: 5.6
TiN	N_2 = 11 l/min, $TiCl_4$ = 2 ml/min	970	500	1889	TiN: 6.3
TiB_2	$TiCl_4$ = 2.6 ml/min, BCl_3 = 480ml/min	850	900	nm	TiN: 0.5 – TiB_2: 3.4

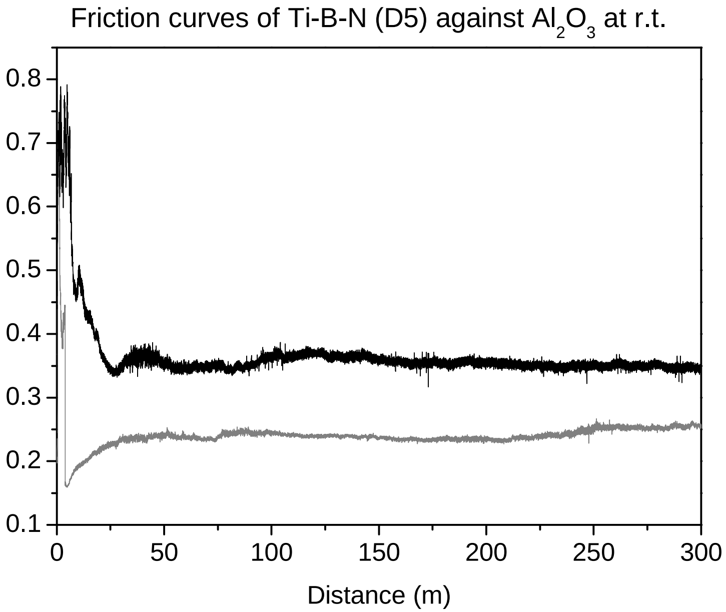

Fig. 60: Exemplary friction curves of Ti-B-N coatings D5 against Al_2O_3 at r. t. (L = 300 m, F_N = 7 N, v = 7.5 cm/s, r = 3 mm).

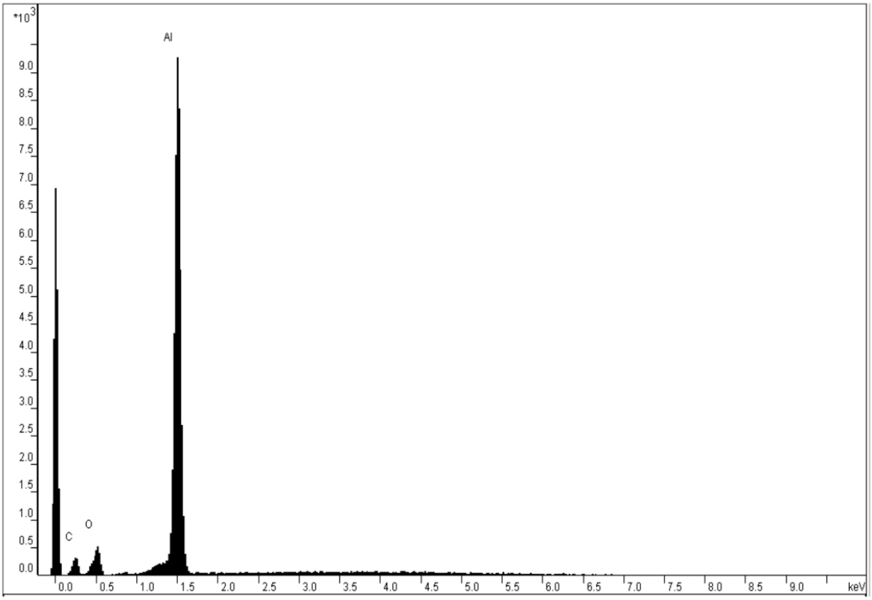

Fig. 61: EDX spectrum of Al_2O_3 balls.

Table 17: Composition of 100Cr6 steel as specified from the supplier (Test Certificate of material AISI-E-52100).

Element	C	Mn	Si	Cr	S	P
Weight %	0.99	0.35	0.27	1.54	0.019	0.013

List of References

1. Lux, B., et al. 1986, Thin Solid Films, Vol. 138, p. 49.

2. Wagner, J., et al. *Structure and Properties of CVD* TiC_xN_{1-x} *Coatings.*[eds.] G. Kneringer, P. Rödhammer and H. Wildner. Plansee Holding AG, 2001. 15th International Plansee Seminar. Vol. 2, p. 917.

3. Kathrein, M., et al. 2003, Surf. Coat. Technol., Vols. 163-164, p. 181.

4. Schintlmeister, W., et al. 1984, Wear, Vol. 100, p. 153.

5. Holzschuh, H. *Chemical-Vapor Deposition of Wera Resistant Hard Coatings in the Ti-B-C-N System: Properties and Metal-Cutting Tests.*[eds.] G. Kneringer, P. Rödhammer and H. Wildner. Plansee Holding AG, 2001. 15th Plansee Seminar. Vol. 2, p. 441.

6. Holzschuh, H. 2002, Int. J. Refract. Met. Hard Mater., Vol. 20, p. 143.

7. Lee, D.B. and Kim, S.K. 2007, Met. Mater. Int., Vol. 13, p. 469.

8. Stüber, M., Schier, V. and Holleck, H. 1995, Surf. Coat. Technol., Vols. 74-75, p. 833.

9. Zhong, D., et al. 2001, Thin Solid Films, Vol. 320, p. 398.

10. Santhanam, A.T., Quinto, D.T. and Grab, G.P. 1996, Int. J. Refract. Met. Hard Mater., Vol. 14, p. 31.

11. Wolfe, G.J., Petrosky, C.J. and Quinto, D.T. 1986, J. Vac. Sci. Technol. A, Vol. 4, p. 2747.

12. Larsson, A. and Ruppi, S. 2002, Thin Solid Films, Vol. 402, p. 203.

13. Bonetti, R.S., Wiprächtiger, H. and Mohn, E. 1990, Met. Powder Rep., Vol. 45, p. 837.

14. Kudapa, S., et al. 1999, Surf. Coat. Technol., Vol. 120, p. 259.

15. Holzschuh, H. 2004, Thin Solid Films, Vols. 469-470, p. 92.

16. Holzschuh, H. *Moderate Temperature CVD Coatings in the Ti-B-N System.*[eds.] G. Kneringer, Rödhammer P. and H. Wildner. Plansee Holding AG, 2005. 16th International Plansee Seminar. Vol. 2, p. 801.

17. Mayrhofer, P.H. and Stoiber, M. 2007, Surf. Coat. Technol., Vol. 201, p. 6148.

18. Stoiber, M., et al. 2003, J. Vac. Sci. Technol. B, Vol. 21, p. 1084.

19. Gissler, W. 1994, Surf. Coat. Technol., Vol. 68, p. 556.

20. Wagner, J., et al. 2006, Surf. Coat. Technol., Vol. 201, p. 4247.

21. Novotny, H., et al. 1961, Mh. Chem., Vol. 92, p. 403.

22. Mitterer, C., Rauter, M. and Rödhammer, P. 1990, Surf. Coat. Technol., Vol. 41, p. 351.

23. Rother, B. and Kappl, H. 1997, Surf. Coat. Technol., Vol. 96, p. 163.

24. Jung, D.H., et al. 2003, Surf. Coat. Technol., Vols. 174-175, p. 638.

25. Müller, K.B. 2002, J. Mater. Proc. Technol., Vols. 130-131, p. 432.

26. Neidhardt, J., et al. 2006, Acta Mater., Vol. 54, p. 4193.

27. Hsieh, J.H., Tan, A.L.K. and Zeng, X.T. 2006, Surf. Coat. Technol., Vol. 201, p. 4049.

28. Zhang, W.H. and Hsieh, J.H. 2000, Surf. Coat. Technol., Vol. 130, p. 240.

29. Mitsuo, A., et al. 1998, Surf. Coat. Technol., Vols. 103-104, p. 98.

30. Dreiling, I., et al. 2009, Surf. Coat. Technol., Vol. 204, p. 1008.

31. Zhong, D., et al. 2003, Surf. Coat. Technol., Vols. 163-164, p. 50.

32. Mitterer, C., et al. 2000, Surf. Coat. Technol., Vol. 125, p. 233.

33. Mayrhofer, P.H., et al. 2006, J. Appl. Phys., Vol. 100, p. 044301.

34. Lu, Y. H., et al. 2005, J. Vac. Sci. Technol. B, Vol. 23, p. 449.

35. Constable, C.P., Yarwood, J. and Münz, W.D. 1999, Surf. Coat. Technol., Vol. 116, p. 155.

36. Exharos, G.J. and Donley, M.S. 1987, Microbeam Anal., Vol. 22, p. 125.

37. Rebelo de Figueiredo, M., et al. 2010, Tribol. Lett., Vol. 40, p. 365.

38. Muratore, C., et al. 2011, Wear, Vol. 270, p. 140.

39. Klauser, F., et al. 2010, Chem. Vap. Deposition, Vol. 16, p. 127.

40. Izak, T., et al. 2010, Chem. Pap., Vol. 64, p. 46.

41. Adelhelm, C., et al. 2009, J. Appl. Phys., Vol. 105, p. 033522.

42. Klein, M.V., Holy, J.A. and Williams, W.S. 1978, Phys. Rev. B, Vol. 17, p. 1546.

43. Spengler, W., Kaiser, R. and Bilz, H. 1975, Solid State Comm., Vol. 17, p. 19.

44. Spengler, W. and Kaiser, R. 1976, Solid State Comm., Vol. 18, p. 881.

45. Spengler, W., et al. 1978, Phys. Rev. B, Vol. 17, p. 1095.

46. Ding, Z.H., et al. 2009, J. Alloys Compd., Vol. 421, p. 247.

47. Lohse, B.H., Calka, A. and Wexler, D. 2005, J. Appl. Phys., Vol. 97, p. 114912.

48. Amer, M., et al. 1998, J. Appl. Phys., Vol. 84, p. 5817.

49. Lengauer, W. *Handbook of Ceramic Hard Materials, Chapter 7: Transition Metal Carbides, Nitrides, and Carbonitrides.* [ed.] R. Riedel. Wiley VCH, 2000. Part 1: Structures and Properties.

50. Pierson, H.O. *Handbook of Chemical Vapor Deposition: Principles, Technology, and Applications.* William Andrew Inc., 1999.

51. nGimat$^{(TM)}$. [Online] http://www.ngimat.com/technology/ccvd.html.

52. Holmberg, A. and Matthews, K. *Coatings Tribology - Contact Mechanisms, Deposition Techniques and Applications.* Elsevier Science, 2009.

53. Jensen, K.F. and Kern, W. *Thin Film Processess II.* [eds.] W. Kern and J. L. Vossen. Academic Press, 1991.

54. Mattox, D.M. *Handbook of Physical Vapor Deposition (PVD) Processing.* William Andrew, 2010.

55. Jeitschko, W., Pöttgen, R. and Hoffmann, R.-D. *Handbook of Ceramic Hard Materials, Chapter1: Structural Chemistry of Hard Materials.* [ed.] R. Riedel. Wiley VCH, 2000. Part 1: Structures and Properties.

56. Parthé, E. and Yvon, K. 1970, Acta Crystallogr. B, Vol. 26, p. 153.

57. Yvon, K. and Parthé, E. 1970, Acta Crystallogr. B, Vol. 26, p. 149.

58. Haag, S. *Ionenstrahlgestützte Abscheidung dünner Funktionsschichtsysteme im System Ti-B-C-N und deren Charakterisierung.* Universität Heidelberg, 2003. PhD Thesis.

59. Tomashik, V. *B-N-Ti (Boron - Nitrogen - Titanium).* [eds.] G. Effenberg and S. Ilyenko. Springer Materials - The Landolt-Börnstein Database.

60. Spieß, L., et al. *Moderne Röntgenbeugung.* Vieweg + Teubner, 2009.

61. Volodymyr, I. *C-N-Ti (Carbon - Nitrogen - Titanium).* [eds.] G. Effenberg and S. Ilyenko. Springer Materials - The Landolt-Börnstein Database.

62. Berg, G., et al. *Handbook of Ceramic Hard Materials, Chapter 9: Data Collection of Properties of Hard Material.* [ed.] R. Riedel. Wiley VCH, 2000. pp. 965–995. Part 3.

63. Massalski, T.B., et al. *Binary Alloy Phase Diagrams.* [ed.] T. B Massalski. ASM International, 1990. p. 1655. Vol. 2.

64. Massalski, T.B., et al. *Binary Alloy Phase Diagrams.* [ed.] T. B. Massalski. ASM International, 1990. p. 392; 595. Vol. 1.

65. Ferraro, J.R. and Nakamoto, K. *Introductory Raman Spectroscopy.* Academic Press, Inc., 1994.

66. Graves, P.R. and Gardiner, D. J. *Practical Raman Spectroscopy.* Springer, 1989.

67. Presser, V. *Oxidation and wet wear of silicon carbide.* Universität Tübingen, 2009. PhD thesis.

68. Schuster, B. *Wachstum und Orientierung organischer Halbleiterschichten.* Universität Tübingen, 2009. PhD thesis.

69. Sherwood, P.M.A. *Vibrational spectroscopy of solids.* Cambridge University Press, 1972.

70. Turrell, G. *Infrared and Raman Spectra of Crystals.* Academic Press, Inc., 1972.

71. Werninghaus, T. *Micro-Raman Spectroscopy Investigation of Hard Coatings.* Technische Universität Chemnitz-Zwickau, 1997. PhD thesis.

72. Merlin, R., Pinczuk, A. and Weber, W.H. *Raman Scattering in Material Science: Chapter 1 - Overview of Phonon Raman Scattering in Solids.* [eds.] W. H. Weber and R. Merlin. Springer, 2000.

73. Montgomery, G.P., et al. 1972, Phys. Rev. B, Vol. 6, p. 4047.

74. Benedek, G. and Nardelli, G.F. 1967, Phys. Rev. , Vol. 154, p. 154.

75. Balkanski, M., Wallis, R.F. and Haro, E. 1993, Phys. Rev. B, Vol. 28, p. 1928.

76. Georgi, C., Hecker, M. and Zschech, E. 2007, J. App. Phys., Vol. 101, p. 123104.

77. Schneider, A. *In situ- und online-Raman-Spektroskopie zur Analyse von Halbleiterheterostrukturen aus* ZnS_xSe_{1-x} *und Gruppe-III-Nitriden.* Technische Universität Chemnitz, 2000. PhD thesis.

78. Presser, V., et al. 2009, Appl. Spectrosc., Vol. 63, p. 1288.

79. Shebanova, O.N. and Lazor, P. 2003, J. Raman Spectrosc., Vol. 34, p. 845.

80. Taylor, A. and Sinclair, H. 1945, Proc. Phys. Soc., Vol. 57, p. 126.

81. Vegard, L. 1921, Z. Phys., Vol. 5, p. 17.

82. Pakokthom, C., Rujijanagul, G. and Tunkasiri, T. 1999, J. Mater. Sci. Lett., Vol. 18, p. 747.

83. Scherrer, P. 1918, Göttinger Nachr. Gesell., Vol. 2, p. 98.

84. Patterson, A.L. 1939, Phys. Rev., Vol. 56, p. 978.

85. X-Ray Attenuation Length. [Online] http://henke.lbl.gov/optical_constants/atten2.html.

86. Goldstein, J. *Scanning electron microscopy and x-ray microanalysis.* Kluwer Adacemic / Plenum Pulbishers, 2003.

87. Henry, D. and Goodge, J. Geochemical Instrumentation and Analysis. *Wavelength-Dispersive X-Ray Spectroscopy (WDS).* [Online] http://serc.carleton.edu/research_education/geochemsheets/wds.html.

88. Reimer, L. *Scanning electron microscopy : physics of image formation and microanalysis.* Springer, 1998.

89. Hsu, S.M., Zhang, J. and Yin, Z. 2002, Tribol. Lett., Vol. 13, p. 131.

90. Hornbogen, E. *Werkstoffe.* Springer, 1994.

91. Fischer, T.E. and Mullins, W. M. 1992, J. Phys. Chem., Vol. 96, p. 5690.

92. Stachowiak, G.W., Batchelor, A. W. and Stachowiak, G. *Experimental Methods in Tribology.* Elsevier, 2004.

93. Sethuramiah, A. *Lubricated Wear: Science and Technology.* Elsevier, 2003.

94. Badisch, E., et al. 2004, Thin Solid Films, Vol. 460, p. 125.

95. Erdemir, A, Erck, R.A. and Robles, J. 1991, Surf. Coat. Technol., Vol. 49, p. 435.

96. Erdemir, A. 2000, Tribol. Lett., Vol. 8, p. 97.

97. Erdemir, A., Bindal, C. and Fenske, G.R. 1996, Appl. Phys. Lett., Vol. 68, p. 1637.

98. Erdemir, A., et al. 1996, Surf. Coat. Technol., Vols. 86-87, p. 507.

99. Erdemir, A., Fenske, G.R. and Erck, R.A. 1990, Surf. Coat. Technol., Vols. 43-44, p. 588.

100. Langlade, C,, et al. 2002, Appl. Surf. Sci., Vol. 186, p. 145.

101. Gardos, M. 2000, Tribol. Lett., Vol. 8, p. 65.

102. Woydt, M. 2000, Tribol. Lett., Vol. 8, p. 117.

103. Donnet, C. and Erdemir, A. 2004, Tribol. Lett., Vol. 17, p. 389.

104. Hüfner, S. *Photoelectron Spectroscopy, Principles and Application.* Springer, 2003.

105. Biswas, I. *Untersuchung der Orientierung und der Grenzflächen-Eigenschaften verschiedener Phthalocyanine mit Photoemissions- und Röntgenabsorptions-Spektroskopie und der Kelvinschwinger-Methode.* Universität Tübingen, 2010. PhD thesis.

106. Haug, A. *Oberflächenanalytische Untersuchungen von dünnen Cytosin, Thymin-, Uracil- und Hydrogen-Silsesquioxan-Filmen.* Universität Tübingen, 2009. PhD Thesis.

107. VDI 3824. 2001. Part 4. Document no. ICS 03.120.10; 87.020.

108. Möhr, S., et al. 1996, ZAAC, Vol. 622, p. 1035.

109. Decker, B.F. and Kasper, J.S. 1954, Acta Crystallogr., Vol. 7, p. 77.

110. Diehl, R. 1975, Solid State Commun., Vol. 17, p. 743.

111. Huber, M. and Deiseroth, H.J. 1995, Z. Kristallogr., Vol. 210, p. 685.

112. Refractive index database. [Online] http://refractiveindex.info/.

113. Smith, W.E. and Dent, G. *Modern Raman Spectroscopy*. London : John Wiley & Sons, 2005.

114. Munisso, M.C., Zhu, W. and Pezzotti, G. 2009, Phys. Status Solidi B, Vol. 246, p. 1893.

115. Wenzel, T., et al. 2003, Phys. Status Solidi A, Vol. 198, p. 257.

116. Grille, H., Schnittler, C. and Bechstedt, F. 2000, Phys. Rev. B, Vol. 61, p. 6091.

117. Darakchieva, V., et al. 2008, Appl. Phys. Lett., Vol. 93, p. 261908.

118. Zhou, D. and Usher, B.F. 2001, J. Phys. D: Appl. Phys. , Vol. 34, p. 1461.

119. Mitterer, C., et al. 1989, J. Vac. Technol. A, Vol. 7, p. 2646.

120. Mayrhofer, P.H., Mitterer, C. and Clemens, H. 2005, Adv. Eng. Mater., Vol. 7, p. 1071.

121. Wagner, C.W., et al. NIST X-ray Photoelectron Spectroscopy Database. [Online] http://srdata.nist.gov/xps/.

122. Sanchez, C.M.T., et al. 2009, Thin Solid Films, Vol. 517, p. 5683.

123. Lu, Y.H., et al. 2004, Surf. Coat. Technol., Vol. 187, p. 98.

124. Ben el Mekki, M., et al. 1999, Surf. Coat. Technol., Vols. 116-119, p. 93.

125. Begun, G.M. and Bamberger, C.E. 1989, Appl. Spectrosc., Vol. 43, p. 134.

126. Vajeeston, P., et al. 2001, Phys. Rev. B, Vol. 63, p. 045115.

127. Postorino, P., et al. 2001, Phys. Rev. B, Vol. 65, p. 020507.

128. Nadal, M., Grenet, T. and Teyssandier, F. 1993, J. Phys. IV France, Vol. 3, p. 511.

129. Presser, V., et al. 2009, J. Raman Spectrosc., Vol. 40, p. 2015.

130. Barrio, R.A., Castillo-Alvarado, F.L. and Galeener, F.L. 1991, Phys. Rev. B, Vol. 44, p. 7313.

131. Bindal, C. and Erdemir, A. 1996, Appl. Phys. Lett., Vol. 68, p. 923.

132. Raju, G.B., Biswas, K. and Basu, B. 2009, Scripta Mater., Vol. 61, p. 104.

133. Arenal, R., et al. 2006, Nano Lett., Vol. 6, p. 1812.

134. Habig, K.-H. 1990, Surf. Coat. Technol., Vol. 42, p. 133.

135. Gardos, M. N. *Symp. Proc. Of New Materials Approaches to Tribology: Theory and Applications.* [eds.] L. Fehrenbacher, and W. O. Winer E. Pope. Materials Research Society, 1989, p. 325.

136. Zhilyaev, V.A. and Lyubimov, V.D. 1974, Inorg. Mater., Vol. 10, p. 47.

137. Voitovich, R.F. and Pugach, E.A. 1975, Poroshk. Metall., Vol. 2, p. 57.

138. Koh, Y.H., Lee, S.Y. and Kim, H.E. 2001, J. Am. Ceram. Soc., Vol. 84, p. 239.

139. Zhang, E., Zeng, G. and Zeng, S. 2002, J. Mater. Sci., Vol. 37, p. 4063.

140. Qin, Y., et al. 2005, J. Mater. Sci., Vol. 40, p. 6553.

141. De Faria, D.L.A., Silva, S.V. and Oliveira, M.T. 1997, J. Raman Spectrosc., Vol. 28, p. 873.

142. Witke, K., et al. 1999, Appl. Surf. Sci., Vol. 151, p. 33.

143. Witke, K., et al. 1998, J. Raman Spectrosc., Vol. 29, p. 411.

144. Kouteva-Arguirova, S., et al. 2003, J. Appl. Phys., Vol. 94, p. 4946.

145. Tsu, R. and Hernandez, J.G. 1982, Appl. Phys. Lett., Vol. 41, p. 1016.

146. Compaan, A. and Trodahl, H.J. 1984, Phys. Rev. B, Vol. 29, p. 793.

147. Constable, C.P., et al. 2000, J. Vac. Sci. Technol. A, Vol. 18, p. 1681.

148. Mayrhofer, P.H., Stoiber, M. and Mitterer, C. 2005, Scr. Mater., Vol. 53, p. 241.

149. Habig, K.-H. 1986, J. Vac. Sci. Technol. A, Vol. 4, p. 2832.

150. Singer, I.L., Fayeulle, S. and Ehni, P.D. 1991, Wear, Vol. 149, p. 375.

151. Kutschej, K., et al. 2005, Surf. Coat. Technol., Vol. 200, p. 2358.

152. Mc Intyre, D., et al. 1990, J. Appl. Phys., Vol. 67, p. 1542.

153. Desmaison, J., Lefort, P. and Billy, M. 1979, Oxid. Met., Vol. 13, p. 203.

154. Vleugels, J., et al. 2002, Metall. Mater. Trans. A, Vol. 33, p. 3847.

155. Muller, O., O'Horo, M. P. and O'Neill, J. F. 1978, J. Solid State Chem., Vol. 23, p. 115.

156. Shepherd, I.W. 1972, Phys. Rev. B, Vol. 5, p. 4524.

157. Baca, L. and Stelzer, N. 2008, J. Eur. Ceram. Soc., Vol. 28, p. 907.

158. Millet, P. and Hwang, T. 1996, J. Mater. Sci., Vol. 31, p. 351.

159. Kulpa, A. and Troczynski, T. 1996, J. Am. Ceram. Soc., Vol. 79, p. 518.

160. Vieregge, G. *Zerspanung der Eisenwerkstoffe.* Verl. Stahleisen, 1959.

161. Paucksch, E., et al. *Zerspantechnik.* Vieweg + Teubner, 2008.

162. Tönshoff, H.K. and Denkena, B. *Spanen: Grundlagen.* Springer, 2004.

List of Figures

List of Tables